THESE

Présentée à l'Université de Lille
Ecole Doctorale Sciences Pour L'Ingénieur
pour obtenir le grade de :

DOCTEUR DE L'UNIVERSITE

Spécialité : **Micro et Nano technologies, Acoustique et Télécommunications**

Par

Sara HEDAYAT

Conception et fabrication de neurones artificiels pour le traitement bioinspiré de l'information

Soutenance prévue le 18 septembre 2018 devant la Commission d'Examen :

Rapporteurs :

M.Damien QUERLIOZ	Chercheur CNRS – HDR (C2N)
M.Sylvain SAÏGHI	Maître de Conférence – HDR (IMS)

Directeurs thèse:

M.Alain CAPPY	Professeur (IEMN)
Mme.Virginie HOEL	Professeur (IEMN)

Examinateurs:

Mme.Cécile DELACOUR	Chercheur CNRS (NÉEL)
M.Ian O'CONNOR	Professeur (École centrale de Lyon)
Mme.Nathalie ROLLAND	Professeur (IRCICA)
M.Alexandre VALENTIAN	Ingénieur (CEA)

© 2018 Tous droits réservés.

© 2018 Tous droits réservés.

THESE

Présentée à l'Université de Lille
Ecole Doctorale Sciences Pour L'Ingénieur
pour obtenir le grade de :

DOCTEUR DE L'UNIVERSITE

Spécialité : **Micro et Nano technologies, Acoustique et Télécommunications**

Par

Sara HEDAYAT

Conception et fabrication de neurones artificiels pour le traitement bioinspiré de l'information

Soutenance prévue le 18 septembre 2018 devant la Commission d'Examen :

Rapporteurs :	
M.Damien QUERLIOZ	Chercheur CNRS – HDR (C2N)
M.Sylvain SAÏGHI	Maître de Conférence – HDR (IMS)
Directeurs thèse:	
M.Alain CAPPY	Professeur (IEMN)
Mme.Virginie HOEL	Professeur (IEMN)
Examinateurs:	
Mme.Cécile DELACOUR	Chercheur CNRS (NÉEL)
M.Ian O'CONNOR	Professeur (École centrale de Lyon)
Mme.Nathalie ROLLAND	Professeur (IRCICA)
M.Alexandre VALENTIAN	Ingénieur (CEA)

© 2018 Tous droits réservés.

lilliad.univ-lille.fr

Thèse de Sara Hedayat, Université de Lille, 2018

© 2018 Tous droits réservés.

lilliad.univ-lille.fr

Remerciements

Ce travail a été effectué au sein des deux laboratoires CNRS, l'Institut d'Électronique de Microélectronique et de Nanotechnologie (IEMN) et l'Institut de de Recherche sur les Composants logiciels et matériels pour l'Information et la Communication Avancée (IRCICA).

Je souhaite tout d'abord remercier et exprimer ma profonde reconnaissance à mon directeur de thèse. **Pr. Alain Cappy,** Professeur émérite à l'Université de Lille, pour son expertise reconnue mondialement, sa disponibilité sans faille, sa rigueur scientifique, sa passion communicative, sa thématique de recherche et son excellente pédagogie qui m'ont permis d'évoluer scientifiquement et humainement. Je tiens à le remercier de nouveau pour ces quatre années passées à ses côtés.

Je souhaite remercier **Pr. Virginie Hoel**, Professeur à l'Université de Lille, ma co-directrice de thèse qui m'a permis de rejoindre en 2014 la thématique dirigée par Pr.Cappy, intitulée bio-inspirée et qui en 2018 est devenue le groupe « Spine ». Ayant confiance en mes capacités scientifiques lors de mon stage de Master 1, elle m'a demandé de suivre plusieurs projets qui ont abouti à cette magnifique thèse. Je la remercie pour ses conseils et son aptitude de communication.

Je remercie **Pr. Nathalie Rolland**, Professeur à l'Université de Lille, pour avoir accepté de présider cette commission d'examen.

J'adresse mes sincères remerciements à **Dr. Damien Querlioz**, Chargé de recherche au laboratoire C2N, et à **Dr. Sylvain Saïghi**, Enseignant-chercheur au laboratoire IMS, qui m'ont fait l'honneur de rapporter ce travail.

Merci à **Dr. Cécile Delacour**, Chargée de recherche à L'institut de Néel, **Dr. Ian O'Connor,** Professeur à l'Ecole Centrale de Lyon, et **Monsieur Alexandre Valentian**, Ingénieur au CEA, d'avoir accepté de faire partie de ce jury.

Je tiens à remercier la Métropole Européenne de Lille (MEL) et l'Université de Lille qui ont financé ma thèse. Egalement, je tiens à remercier l'ensemble des partenaires l'Université de Salamanque, le GDR Biocomp et le CEA pour m'avoir accompagnée tout au long de ma thèse.

Je tiens à remercier les Intervenants du projet Spine: **Christophe Loyez, François Danneville, Kévin Carpentier, Ilias Sourikopoulos, Laurent Clavier** et **Dimitri Henniquau**. L'excellence d'un travail réside dans chaque individu qui a participé de loin ou de près à ce travail !
Christophe, merci pour tous les moments passés en "carac" et de m'avoir apporté ton soutien et tes conseils que je n'oublierai point. **François**, merci d'avoir initié notre

participation à la conférence de bruit. **Ilias**, merci pour Cadence. **Kevin**, merci pour ton travail rigoureux et tes coups de main. **Laurent**, merci pour tes conseils en Matlab. **Dimitri**, merci de poursuivre ce travail en connectant un neurone biologique à un neurone artificiel.

Je tiens à remercier l'ensemble des personnes de la centrale de caractérisation de IEMN et de IRCICA avec qui j'ai eu le plaisir de travailler et profiter de leurs expériences dans une ambiance chaleureuse : **Vanessa Avramovic, Sylvie Lepilliet, Sophie Eliet, Etienne Okada, Bernard Verbeke et Rédha Kassi**.
Vanessa, merci de m'avoir appris à poser les pointes mais surtout pour ton calme et ta gentillesse. **Sylvie,** merci de m'avoir formé à IC-CAP, pour m'avoir ouvert la porte à 20h, pour toutes nos conversations, et ton soutien indéfectible à nous tous, les doctorants. **Sophie,** merci de m’avoir fait participer à la vidéo de IEMN et pour ta gentillesse. **Etienne,** merci pour tes conseils sur les bancs, ta rigueur et ton professionnalisme. **Bernard,** merci pour ta disponibilité et ta rapidité à effectuer les soudures et les collages des puces. **Rédha,** merci de m'avoir laissé présenter le caddie intelligent à XPERIUM, pour tous nos conversations, tes conseils et coups de main avec les logiciels de "carac".

J’adresse mes sincères remerciements à tous les professeurs, intervenants, et toutes les personnes qui par leurs paroles, leurs écrits, leurs conseils et leurs critiques ont guidé mes réflexions et répondu à mes questions durant mes recherches.
Que l’ensemble des stagiaires, doctorants, Post-docs, Ingénieurs du laboratoire soient aussi remerciés et encouragés à travers ces quelques lignes. Qu’ils n’oublient pas que c’est grâce à leur dynamisme et leur persévérance que les travaux de recherche peuvent progresser.

Je voudrai remercier, l'ensemble de mes collègues et amis: **Guillaume, Ezgi, Sara, Astrid, Riad, Kevin, Louis, Fuanki, Laura, Anne-Sophie, Aymeric, Ahmed, Paul** et l’ensemble des personnes qui m’ont soutenue durant ces trois années de thèse. Je garde d'excellents souvenirs avec chacun de vous. **Guillaume**, merci de m'avoir encouragée à faire de l'enseignement et pour ton précieux soutien. **Ezgi**, merci pour tes recommandations et tes conseils. **Sara**, merci pour tes encouragements extrêmement motivants et ton écoute. **Riad**, merci d'avoir toujours apporté ton aide même quelques minutes avant ma présentation. **Astrid**, merci pour tous les repas que tu as été cherchée et tes visites dans mon bureau avec ton grand sourire réconfortant. **Fuanki** merci pour ton écoute et tes conseils avisés qui m'ont permis de finir ma thèse plus sereinement. **Anne-Sophie**, merci pour toutes les réservations de salle et tous les bons moments passés en ta compagnie. **Kevin**, merci de m'avoir toujours redonné le sourire. **Louis**, merci pour nos conversations à 18h qui nous motivaient à repartir travailler. **Laura**, merci pour toutes nos conversations et ta sérénité que j'ai tant admirée et pour m'avoir emmené en Normandie dans ta famille. **Aymeric**, merci pour nos pauses cafés et tes messages de soutien. **Ahmed**, merci pour ta bonne humeur et de m'avoir fait visiter toutes les parties de L'IRCICA. **Paul**, merci d'avoir partagé ton expérience de thèse

© 2018 Tous droits réservés.

avec moi qui m’a fait avancer plus sereinement.

Je tiens à remercier très spécialement **Romain** qui a toujours été là pour moi durant cette dernière année de thèse. Pour son aide précieuse et son soutien exceptionnel dont je suis extrêmement reconnaissante. Chaque instant de cette dernière année (surtout les plus critiques), tu as été à mes côtés et je serai à tes côtés tout naturellement.

Je remercie mon frère **Shahin** pour ses encouragements et sa capacité d'analyse remarquable. Pendant ces années, ta présence m’a aidé à avancer au mieux.

Je remercie mes parents, **Nader** et **Suzanne**, qui ont toujours été là pour moi durant toutes ces années. Vous avez tout fait pour vos enfants. Vous m’avez donné un magnifique modèle de travail et de persévérance. Dans les moments les plus difficiles vous avez fait preuve de courage et vous m'avez toujours épaulée dans toutes les situations. Je suis redevable d’une éducation dont je suis fière. Papa, ce travail n'aurai pas eu lieu sans ton soutien inconditionnel et tes précieux encouragements.

© 2018 Tous droits réservés.

© 2018 Tous droits réservés.

Abstract

The microelectronics industry faces many challenges. The major one is to increase the performance of computers while reducing their energy consumption. Current computing technology has now reached its limits and it becomes thus urgent to propose new paradigms for information processing capable of reducing the energy consumption while improving the computing performances. Moreover, the human brain, is a fascinating and powerful organ with remarkable performances in areas as varied as learning, creativity, fault tolerance. Furthermore, with its total 300 billion cells, is able to perform complex cognitive tasks by consuming only around 20W. In this context, we investigated a new paradigm called neuromorphic or bio-inspired information processing.

More precisely, the purpose of this thesis was to design and fabricate an ultra-low power artificial neuron using recent advances in neuroscience and nanotechnology. First, we investigated the functionalities of living neurons, their neuronal membrane and explored different membrane models known as Hodgkin Huxley, Wei and Morris Lecar models. Second, based on the Morris Lecar model, we designed analog spiking artificial neurons with different time constants and these neurons were fabricated using 65nm CMOS technology. Then we characterized these artificial neurons and obtained state of the art performances in terms of area, dissipated power and energy efficiency. Finally we investigated the noise within these artificial neurons, compared it with the biological sources of noise in a living neuron and experimentally demonstrated the stochastic resonance phenomenon. These artificial neurons can be extremely useful for a large variety of applications, ranging from data analysis (image and video processing) to medical aspect (neuronal implants).

Résumé

L’industrie de la microélectronique fait face à de nombreux défis dont le principal est celui d’augmenter les performances des ordinateurs tout en réduisant leur consommation d’énergie. Actuellement, les technologies du traitement d'information ont atteint leurs limites et il devient donc urgent de proposer de nouveaux paradigmes capables de réduire la consommation d'énergie tout en augmentant la capacité de calcul des ordinateurs. Le cerveau humain est un fascinant et puissant organe avec des performances remarquables dans les domaines aussi variés que l'apprentissage, la créativité et la tolérance aux fautes. De plus avec ses 300 milliard de cellule, il est capable d’effectuer des taches cognitives en consommant 20W. Dans ce contexte nous avons investiguer un nouveau paradigme appelé "neuromorphic computing" ou le traitement bio-inspiré de l'information.

Plus précisément, l'objective de cette thèse est de concevoir et de fabriquer un neurone artificiel a très faible consommation utilisant les récentes avancées scientifiques dans les neurosciences et les nanotechnologies. Premièrement, on a investigué le fonctionnement d'un neurone vivant, sa membrane neuronale et nous avons exploré trois différents modèles de membranes connues sous le nom de Hodgkin Huxley, Wei et Morris Lecar. Deuxièmement, en se basant sur le modèle de Morris Lecar, nous avons réalisé des neurones artificiels analogiques à spike avec différentes constantes de temps. Puis ils ont été fabriqués avec la technologie 65nm CMOS. Par la suite, nous les avons caractérisés et obtenu des performances dépassant l’état de l’art en terme de surface occupée, puissance dissipée et efficacité énergétique. Finalement, on a analysé et comparé le bruit dans ces neurones artificiels avec le bruit dans des neurones biologiques et on a démontré expérimentalement le phénomène connu sous le nom de résonance stochastique.

Ces neurones artificiels peuvent être extrêmement utiles pour une large variété d’application allant du traitement de données à l’application médicale.

© 2018 Tous droits réservés.

© 2018 Tous droits réservés.

Table of content

© 2018 Tous droits réservés.

© 2018 Tous droits réservés.

© 2018 Tous droits réservés.

© 2018 Tous droits réservés.

Thèse de Sara Hedayat, Université de Lille, 2018

Chapter 1.

Introduction

© 2018 Tous droits réservés.

lilliad.univ-lille.fr

© 2018 Tous droits réservés.

The context and challenges of this thesis are described in the chapter 1. A brief introduction of the information processing and its origin are presented. After highlighting the challenges to overcome and the various ways to perform the data processing, we present our investigated solution, which relies on hardware brain inspired approach. An overview of the neuromorphic computing and the major projects in this thematic are also presented in the introduction. Finally, the objective and challenges of this thesis are highlighted.

1.1 Information processing

1.1.1 Introduction to information processing

There are various ways to process the information. One is realized using manmade devices such as computers and the other one is accomplished by living systems for instance the brain. The neuronal architecture and the coding used in the brain to process the information differ from the conventional computers. The brain is fascinating and a powerful living system showing remarkable performance in areas as varied as the complexity of the processed information, the fault tolerance, learning, energy consumption and regeneration of the signal. Representing 2% of the weight of a human body and consuming 20% of the overall average power, the brain is revealed the most complex and efficient information processor known today.

There is a major interest to study the difference between brain and conventional computing in order to bridge neuroscience and electronic engineering to develop artificial neural networks. This is the purpose of the following sections.

1.1.2 History of information processing in hardware

Alan Mathison Turing contributed to several areas such as cognitive science, artificial intelligence and mainly to computer science (Beavers, 2013). His theoretical work in 1936, on the digital computing machine, is now referred as to universal Turing machine (Turing, 1936), on which the conventional computer is based. Fundamental idea of a universal stored-program computing machine came from Turing and was promoted in the United States by John von Neumann and in England by Max Newman. By the end of 1945, several groups, including Turing, were devising plans for an electronic stored program universal digital computer (a Turing machine in hardware). His talent in the information processing and computers was demonstrated when he broke Naval Enigma and was the principal designer of the "bombe" : a high-speed code-breaking machine. In 1945, he designed the Automatic Computing Engine (ACE). Turing and his group pioneered the science of computer programming, writing a library of sophisticated mathematical programs for ACE. Finally, the world's first working electronic stored-program digital computer was developed by Newman in 1948, nevertheless the concept of Turing machine was a fundamental influence on this achievement (Copeland, 2004).

© 2018 Tous droits réservés.

1.1 Information processing

Since, the progress in electronic and nanotechnology (e.g., transistors, integrated circuits, memories, microprocessors) leads to the development of many versions of computers. These developments provided the programmable electronic machines (computers) that are ubiquitous today.

The information processing is combined of computation and communication. Communication moves operands and results around while computation combines operands to produce results (Boahen, 2017). In general, information processing can be described by two categories of analog and digital. Analog computer (see the upper left of **Figure 1.1**) is the first generation of computer where the computation and the communication was carried out with an analog signal. Current computers are digital computers (see the lower right of **Figure 1.1**), which use digital signals to compute as well as to communicate. The brain (see the lower left of **Figure 1.1**), known as the most energy-efficient computer, uses analog signals to compute and digital signals to communicate. In fact, the addition of information at synaptic level is considered as analog computing in the brain. The propagation of information in form of electrical impulses also called spikes is considered as digital signals enabling the communication in the brain.

The fourth category (see the upper right of **Figure 1.1**), which consists of using digital signal to compute and using analog signal to communicate, is not yet explored.

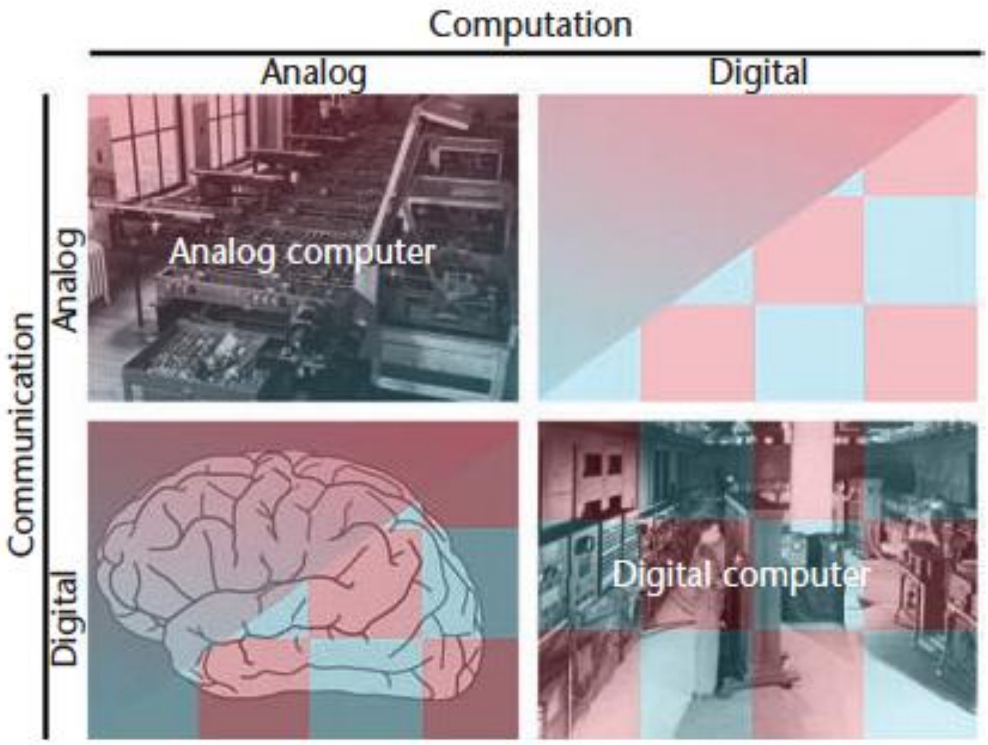

Figure 1.1 Signal choices for communication and computation (Boahen, 2017).

© 2018 Tous droits réservés.

1.2 Challenges to overcome

In the previous paragraph, we have presented briefly the conventional computer and the basis of information processing. In this section, some of the most important challenges of information processing and computers are presented. The quantity of data used, transported and created by sensors and end-user devices (from PCs to tablets and smartphones to digital TV), constitutes the digital universe. This one is growing exponentially and needs new procedures and systems to deal with data.

1.2.1 Exponential growth of Big Data

In our modern era, information processing and the Internet are omnipresent. Social media, sensors, enterprise data are all participating to the generation of enormous amount of data. According to the International Data Corporation (IDC), this amount of data created each year has grown exponentially. It reached 2.8 zettabytes in 2012 and will be around 40 zettabytes in 2020 (see **Figure 1.2**).

Figure 1.2 Exponential evolution of Big Data (Noor, 2014).

The Big data are stored in vast data centers (see **Figure 1.3**) with enormous power consumption. Data centers consume about 3% of the global electricity supply and are accounting for about 2 % of total greenhouse gas emissions. In 2015, the world's data centers used 416.2 Terawatt-hours of electricity, which was higher than the UK's total consumption of about 300 Terawatt-hours. USA data centers consumed about 70 billion Kilowatt-hours of electricity in 2014 representing 2% of the country's total energy consumption. That is equivalent to the amount consumed energy by about 6.4 million average American homes this year.

© 2018 Tous droits réservés.

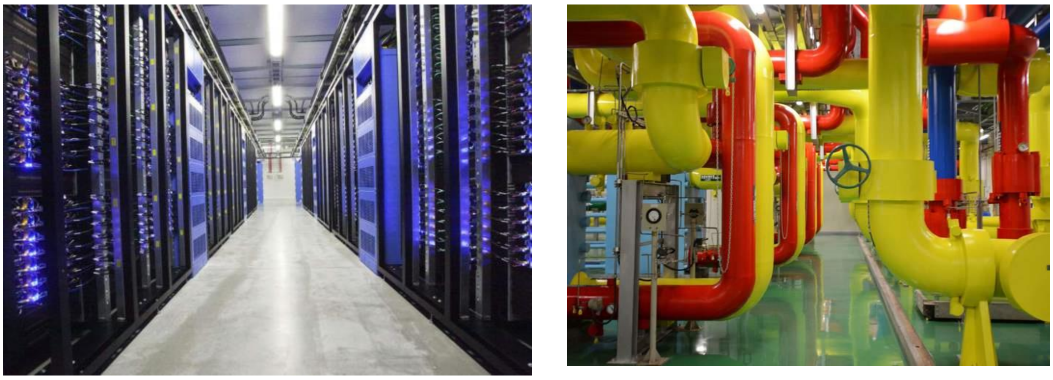

Figure 1.3 Left: The Facebook server hall in the city of Lulea, Sweden. Right: The facilities of the Google data center in Taiwan.

Finally, researchers reported that in 2025, all the world data centers would consume 1/5 of earth's power.

The increasing gap between the quantity of generated information and the computing possibilities are one of the challenges of the 21st century. Moreover, this implies an increase of the power consumption to transfer and process the data, which represents another major challenge of the 21st century.

1.2.2 Limitation of current information processing devices

The current computing is based on Von Neumann architecture, binary logic and the CMOS technology. The Von Neumann (V.N.) architecture drawback known as the "Von Neumann bottleneck" is due to the separation between processor and memory. These different parts of the microprocessor are connected by communication pathways called buses. Therefore, there are multiple paths and constant data traveling across these buses resulting in the bottleneck. The memory units also benefit of the technological improvement like microprocessors but the address decoding/reading/writing data steps are difficult to accelerate. The memory is not able to deliver information as fast as the processor is able of handling this information. This phenomenon is strongly accentuated when the architecture contains parallel multi-cores. Furthermore, in the paper entitled "*The chips are down for Moore's law*" published in February 2016, Mitchell Waldrop declares, "*the semiconductor industry will soon abandon its pursuit of Moore's law. Now things could get a lot more interesting*" (Waldrop, 2016). This sentence shows clearly that the current microprocessor computing technology has now reached some limits.

Another point is the power dissipation of microprocessors, even if the integration density continues its exponential growth (which seems difficult due to the end of the Moore law), the circuit speed has been kept constant in order to limit the power dissipation at 100 W/cm^2 (see **Figure 1.4**).

© 2018 Tous droits réservés.

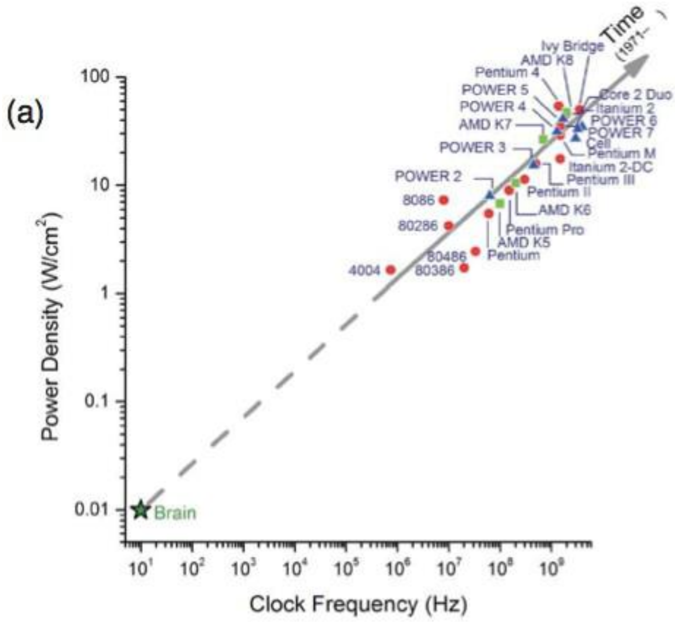

Figure 1.4 (a) The parallel, distributed architecture of the brain is different from the sequential, centralized Von Neumann architecture of today's computers. The trend of increasing power density and clock frequencies of processors is headed away from the brain's operating point (Merolla et al., 2014).

Hence, both architecture (V.N.) and devices used in the current information processors are reaching physical limits.

Carver Mead declared about the binary coding that: "*We lose a factor of about 100 because, the way we build digital hardware, the capacitance of the gate is only a very small fraction of the capacitance of the node. The node is mostly wire, so we spend most of our energy charging up the wires and not the gate. We use far more than one transistor to do an operation; in a typical implementation, we switch about 10 000 transistors to do one operation*." (Mead, 1990).

In addition, computers, champion for calculation of complex equation, have some difficulties to classify/organize/recognize data/patterns in the gray scale. Hence, it is time to propose new paradigms of information processing able to reduce the energy consumption in a drastic way while improving the performances. Artificial neural networks (ANN), computing in the same way as the human brain, could be the answer. The need of intelligent computers has pushed researchers to develop the neuromorphic computing domain. This part will be presented in following paragraphs with a brief introduction of the need of artificial intelligence.

1.2.3 Need of artificial intelligence

Artificial Intelligence (AI) could be defined as the desire to emulate the human cognitive behavior in order to develop intelligent machines. Many topics are concerned by AI such as self-driving cars, drones and robots. Associated with the appropriate learning rules, artificial neuron networks could be used in the frame of these

© 2018 Tous droits réservés.

applications to realize associative memory, video classifiers or cognitive autonomous robots.

In this context, the technology used to build brain like processors most be energy efficient, real time computing and able to analyze, communicate and learn at the human brain speed and level. Current AI technologies offer real time computing chips, but with high-energy consumption and without human intelligence, which cannot be used for intelligent embedded systems.

1.2.4 Conclusion on possible solutions

The end of Moore Law for CMOS technology, one of the three pillars of current processors impact all the semiconductor industry of 400 billion dollars (WSTS, 2017) sales and had changed the direction of research. The 'International Technology Roadmap for Semiconductors' (ITRS) is becoming 'International Roadmap for Devices and Systems' (IRDC) implying investigation in both new devices and new systems. In fact, to overcome the challenges mentioned before, three approaches can be investigated, first is to keep current information processing architecture and to replace the CMOS by another revolutionary device. This way has not yet produced any satisfying result. The second approach consists to change both the architecture and the device of the current information processing. Research on quantum computers is an example of this second option where quantum cubes play the role of switches and quantum computers replace the conventional computer. This approach can take a long time, as the researcher must overcome many challenges since the quantum cube can operate at low temperature, which is not yet adapted to our environment. The third option is to keep the CMOS technology and change the computation architecture.

© 2018 Tous droits réservés.

1.3 Investigated solution

In conclusion, based on the needs and the challenges to overcome, the alternative solution is to propose new paradigms for information processing. In this task, we have chosen to take as a model, the most efficient and powerful information processor, the brain.

1.3.1 Human Brain

The human brain has a massively parallel and reconfigurable architecture, composed of, 10^{11} neurons and 10^{15} synapses (Vuillaume et al., 2013). The brain has 300 million synaptic connections in each cm^3, which represents the number of stars in the Milky Way. The brain, with its total 300 billion cells, is able to perform a cognitive task by consuming only around 20W that is 10^4 times less than the power consumption of multicore based supercomputers.

The brain is a fascinating information processor. As you are reading these words, your brain is performing multiple complex cognitive tasks consuming only 20W during a millisecond. Moreover, it is capable of imagination, innovation that is beyond any supercomputer capabilities. This enigmatic organ has been studied over hundreds of years and still need to be investigated.

1.3.2 Brain information processing and coding

Based on neuroscience research until now, it is known that the brain uses electrical impulses called spikes to transfer information. A parallel is made between the 0 and 1 in computer science and the spikes in the brain. In fact, the absence of spike is considered like 0 and the generation of a spike in the brain as 1. It seems that the brain uses both the timing of a spike (time coding) and the frequency of a spike train (rate coding) to analyze information. The brain remains a mysterious living system, which has proved his efficiency in information processing. It is the key element of the neuromorphic computing and artificial intelligence.

© 2018 Tous droits réservés.

1.4 Neuromorphic computing

1.4.1 Neuromorphic computing origins

In 1990, Carver Mead invented the "neuromorphic computing" term (Mead, 1990). He referred to very large-scale integration with analog components that mimicked biological neuronal systems as "neuromorphic" systems. The use of neuromorphic systems for information processing is the goal of neuromorphic computing. More recently, the term of neuromorphic computing includes implementations that are based on brain-inspired architecture (Schuman et al., 2017).

The history of brain-inspired computing starts in 1943 with the Warren McCulloch and Walter Pitts neuron. Their work was the first step toward the artificial neural networks (ANNs) since a neural network could be simply defined as connected neurons. The McCulloch-Pitts neuron model is a simplified mathematical model used to represent neural properties (McCulloch and Pitts, 1943). It is based on the existence of a threshold voltage for the activation of an action potential. Using their model, it is possible to figure out most Boolean logic function. Their neurons operated under the following assumptions. They are binary devices as the input and output is either zero or one. They have fixed threshold. They receive inputs from excitatory synapses with identical weight. Inhibitory inputs have an absolute veto on excitatory input, if there is even one inhibitory input, the neuron will not fire (absolute inhibition). At each time step, the neurons are simultaneously updated by their inputs (inhibitory and excitatory synapses).

In 1949, Donald Hebb, considered as the father of neural networks, introduced the Hebbian learning rule, which provides the foundation of modern neural network (Wang & Raj, 2017). In 1958, Frank Rosenblatt introduced the first perceptron (Wang & Raj, 2017). The difference between the perceptron of Rosenblatt and the neuron of McCulloch-Pitts was: the synaptic weights (can take positive or negative value) and the neurons thresholds were variable. There is no absolute inhibitory synapse. The most important difference is that the perceptron had a learning rule. In 1970, Marvin L. Minsky and Seymour A. Papert published a book entitled "Perceptrons: an introduction to computational geometry" which acknowledge the perceptron's strengths while also showing major limitations (Olazaran, 1996). Critics of this book state that since a single artificial neuron (one perceptron) is not able of implementing a XOR function, hence larger networks have the same issue and this technic must be dropped. It is known that this book was the source of many controversies in the field of neural networks and artificial intelligence. Since many researchers have continued the research on the neural network, a summary of this evolution is presented in **Table 1.1**.

© 2018 Tous droits réservés.

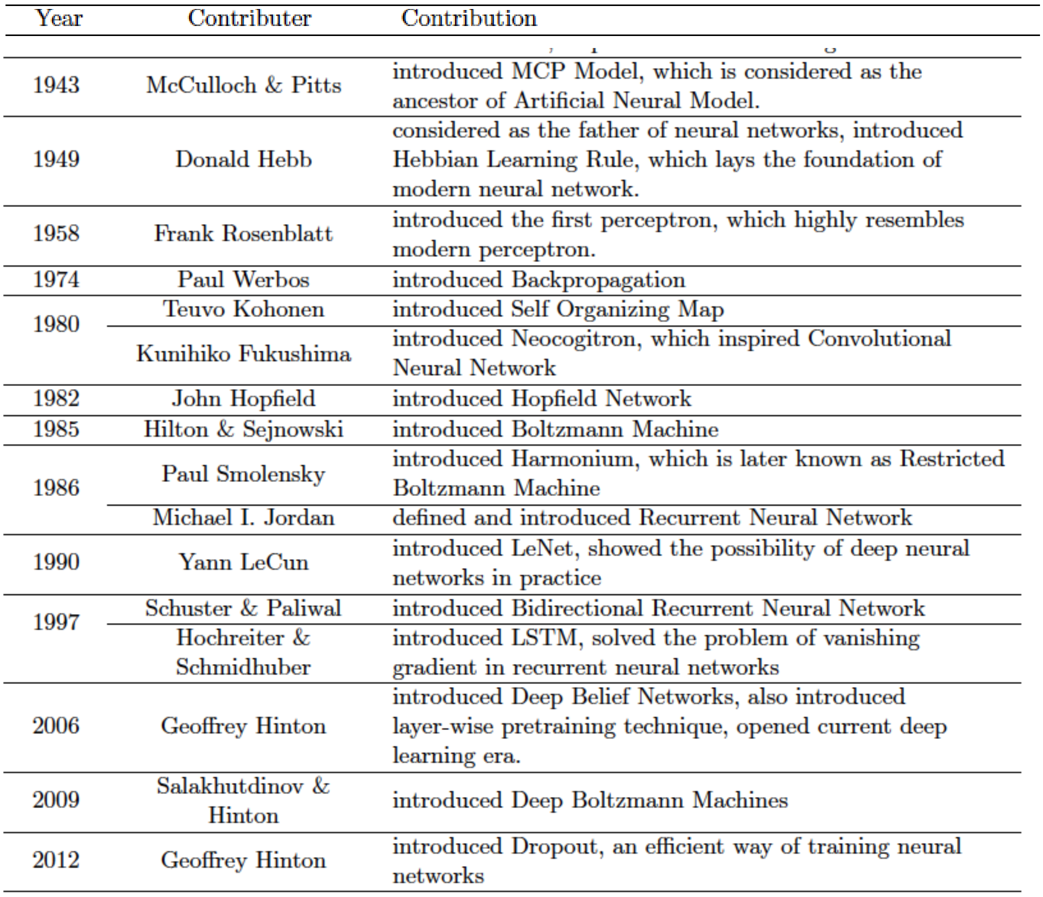

Year	Contributer	Contribution
1943	McCulloch & Pitts	introduced MCP Model, which is considered as the ancestor of Artificial Neural Model.
1949	Donald Hebb	considered as the father of neural networks, introduced Hebbian Learning Rule, which lays the foundation of modern neural network.
1958	Frank Rosenblatt	introduced the first perceptron, which highly resembles modern perceptron.
1974	Paul Werbos	introduced Backpropagation
1980	Teuvo Kohonen	introduced Self Organizing Map
	Kunihiko Fukushima	introduced Neocogitron, which inspired Convolutional Neural Network
1982	John Hopfield	introduced Hopfield Network
1985	Hilton & Sejnowski	introduced Boltzmann Machine
1986	Paul Smolensky	introduced Harmonium, which is later known as Restricted Boltzmann Machine
	Michael I. Jordan	defined and introduced Recurrent Neural Network
1990	Yann LeCun	introduced LeNet, showed the possibility of deep neural networks in practice
1997	Schuster & Paliwal	introduced Bidirectional Recurrent Neural Network
	Hochreiter & Schmidhuber	introduced LSTM, solved the problem of vanishing gradient in recurrent neural networks
2006	Geoffrey Hinton	introduced Deep Belief Networks, also introduced layer-wise pretraining technique, opened current deep learning era.
2009	Salakhutdinov & Hinton	introduced Deep Boltzmann Machines
2012	Geoffrey Hinton	introduced Dropout, an efficient way of training neural networks

Table 1.1 Major contribution to ANNs development (Wang & Raj 2017).

Researchers from a variety of fields, such as materials science, neuroscience, electrical engineering, computer engineering, and computer science are considered as the neuromorphic computing community. In our domain, the neuromorphic systems can be considered in two categories: software and hardware systems. Artificial neural networks (ANNs) used by Google to classify images or playing games with AlphaGo is some of the applications of the software field of neuromorphic computing. To perform this task, the ANNs use new algorithms allowing these networks to be trained and/or learn on their own. The hardware neuromorphic systems are made of neuro-inspired devices and architecture. As an example, Truenorth chip is a neuromorphic CMOS integrated circuit produced by IBM in 2014 (Merolla et al., 2014). With over a million of programmable neurons and over 268 million programmable synapses, it overcomes the Von Neumann bottleneck, by handling the memory, computation and communication in each of the 4096 cores of this Truenorth chip. However, the energy consumption remains still high.

It is worth mentioning that several international research programs such as SyNAPSE, the Brain initiative, the Human Brain Project, etc. are investing billions of dollars in

© 2018 Tous droits réservés.

neuromorphic computing and systems. In the following paragraphs, we will present three of these projects.

1.4.2 Neuromorphic computing major projects

A. The SyNAPSE project

SyNAPSE (Systems of Neuromorphic Adaptive Plastic Scalable Electronics) is a 21 million dollars project funded by DARPA (DARPA, 2013). The goal of this project launched in 2008, was to design a new computer architecture that mimics the brain. It had plans to combine the fields of nanoscience, neuroscience and supercomputers with the goal of developing devices with cognitive aspects. IBM's Truenorth chip has been developed in the frame of this project.

B. The Brain initiative project

The brain initiative project was launched in 2013 by the president Obama who declared, "*It will spark innovation, create jobs, stimulate the economy, treat autism, Alzheimer's, epilepsy and schizophrenia, not to mention stroke, traumatic brain injury and post-traumatic stress disorder*"(Obama, 2013).

The total investment was about 3.8 billion dollars with the contribution of three federal agencies, the National Institutes of Health NIH ($40 million), the National Science Foundation NSF ($20 million) and the Defense Advanced Research Projects Agency DARPA ($50 million). Many research institutes have also contributed to this project with 60 million dollars from the Allen Institute, 30 million dollars for Brain Science, 30 million dollars from the Howard Hughes Medical Institute, 28 million dollars from the Salk Institute for Biological Studies and 4 million dollars from the Kavli Foundation. The timeline of the project is ten years.

C. The Human Brain Project

On the other side of the Atlantic, on 28 January 2013, the European Commission announced its decision to finance the Human Brain Project, a 10-year project that is estimated to cost 1.19 billion euros (HBP, 2013). This project aims to bring together all the human brain current knowledge in order to rebuild it, piece by piece, on the strength of computer models and simulations. These two European and American projects are not competitors, but rather complementary. As Richard Walker, a spokesperson for the Human Brain Project, points out, "*all the data produced by the American project will be in the public domain, and that is a lot of results that can be incorporated into the Human Brain Project models*" (Figaro, 2013).

Understanding the human brain is one of the greatest scientific challenges facing the 21st century. If we can rise to this challenge, we can gain profound insights into what makes us human, develop new treatments for brain diseases and build revolutionary

© 2018 Tous droits réservés.

computing technologies. In the frame of our work, two main applications linked to neuromorphic systems are developed. This will be discussed in the next section.

© 2018 Tous droits réservés.

1.5 Neuromorphic computing and systems, interests and applications

Neuromorphic computers will gather several advantages such as perform complex calculations faster, more power efficiently, and on a smaller footprint than traditional Von Neumann architectures. These characteristics provide compelling reasons for developing hardware which employs neuromorphic architectures (Schuman et al., 2017).

This neuro-inspired field will impact two domains, information processors or computers and the human health care. Neuromorphic systems will be used in both cases to overcome their current limitation and increase their performances.

In the case of computers, you may imagine a smart machine helping you during the day-to-day activities. This intelligent computer communicates, learns, make decisions, and even advice you based on its resources. Watson is an example of this kind of artificial intelligence (Ferrucci et al., 2010).

In the case of human health care, millions of people die due to neurological diseases all over the world (Feigin et al., 2017). The idea is to fabricate a neuromorphic system to stimulate or even replace the defective brain area. For example, DARPA has launched the project RAM (Restore Active Memory- (DARPA, 2014)) to restore the lost memory of the injured soldiers. The first results obtained in the frame of this project are reported in (Hampson et al., 2018). They have demonstrated the first successful implementation in humans of a proof-of-concept system for restoring memory function by facilitating memory encoding using the patient's own neural codes. This idea can also be extended to an improvement of a healthy brain in terms of memory and learning, improving our intelligence.
For neurological diseases such as the epilepsy disease, we can imagine an intelligent neuromorphic system, playing the role of a "brain pacemaker" which detects the brain crises and stimulates in vivo the specific brain area to neutralize the epileptic crises. BBC has reported in January 2018 a brain pacemaker used for Alzheimer affected patients (Scharre et al., 2018).

In 2015, a primate with spinal cord injury regained control of its paralyzed leg with the help of a neuro-prosthetic system called the "brain-spine interface" that bypassed the lesion, restoring communication between the brain and the region of the spinal cord. They interface legs motor cortex activity with epidural electrical stimulation protocols to establish a brain-spine interface that alleviated gait deficits after a spinal cord injury in non-human primates (Capogrosso et al., 2016).

© 2018 Tous droits réservés.

As described in this section, neuromorphic systems address two major applications one in information processing and second in health care. These applications demonstrate the interest of the research community and validate the investment in this field.

© 2018 Tous droits réservés.

lilliad.univ-lille.fr

1.6 Objective and challenges of thesis

In order to achieve an efficient neuromorphic system, we have chosen the bottom-up approach. This approach corresponds to fabricate an artificial neuron and synapse before fabricating an artificial brain inspired system.

In this context, the main goal of this thesis was to design and fabricate an ultra-low power artificial neuron. This is a multidisciplinary work requiring both knowledge in neuroscience and electronic field. The challenges to overcome are:

1) Investigate and understand the complex functionality of a living neuron, enabling an efficient artificial neuron's design.

2) Design a simple novel architecture with optimized area, enabling the fabrication of neuromorphic VLSI systems.

3) Design and fabrication of analog spiking artificial neuron, using conventional CMOS technology, enabling a fast dissemination to the industry to fulfill current applications.

4) Obtaining ultra-low power consumption for the artificial neuron, responding to the problematic concerning the energy consumption of current information processing systems.

5) Investigate the noise within the artificial neuron, allowing a comparison to the biological sources of noise in a living neuron.

© 2018 Tous droits réservés.

1.7 References

(Beavers, 2013) Beavers, A. F. (2013). Alan Turing : Mathematical Mechanist. Alan Turing: His Work and Impact, 481–485. https://doi.org/10.1073/pnas.0703993104

(Boahen, 2017) Boahen, K. (2017). A Neuromorph's Prospectus. Comput. Sci. Eng. 19, 14–28. doi: 10.1109/MCSE.2017.33

(Capogrosso et al., 2016) Capogrosso, M., Milekovic, T., Borton, D., Wagner, F., Moraud, E. M., Mignardot, J.-B., … Courtine, G. (2016). A brain–spine interface alleviating gait deficits after spinal cord injury in primates. *Nature*, *539*(7628), 284–288. https://doi.org/10.1038/nature20118

(Copeland, 2004) Copeland (2004). The Essential Turing. *Oxford: Oxford* University Press. ISBN 0-19-825079-7

(DARPA, 2013) http://www.artificialbrains.com/darpa-synapse-program

(DARPA, 2014) https://www.darpa.mil/program/restoring-active-memory

(Feigin et al., 2017) Feigin, V. L., Abajobir, A. A., Abate, K. H., Abd-Allah, F., Abdulle, A. M., Abera, S. F., Vos, T. (2017). Global, regional, and national burden of neurological disorders during 1990–2015: a systematic analysis for the Global Burden of Disease Study 2015. The Lancet Neurology, 16(11), 877–897. https://doi.org/10.1016/S1474-4422(17)30299-5

(Ferrucci et al., 2010) Ferrucci, D., Brown, E., Chu-Carroll, J., Fan, J., Gondek, D., Kalyanpur, A. A., … Welty, C. (2010). Building Watson: An Overview of the DeepQA Project. AI Magazine, 31(3), 59. https://doi.org/10.1609/aimag.v31i3.2303

(Figaro, 2013) Des milliards de dollars pour comprendre le cerveau, Le Figaro.fr, http://sante.lefigaro.fr/actualite/2013/04/04/20174-milliards-dollars-pour-comprendre-cerveau

(Hampson et al., 2018) Hampson, R. E., Song, D., Robinson, B. S., Fetterhoff, D., Dakos, A. S., Roeder, B. M., … Deadwyler, S. A. (2018). Developing a hippocampal neural prosthetic to facilitate human memory encoding and recall. *Journal of Neural Engineering*, *15*(3), 036014. https://doi.org/10.1088/1741-2552/aaaed7

(HBP, 2013) The Human Brain Project, http://www.humanbrainproject.eu/index.html.

(Mead, 1990) Mead, C. (1990). Neuromorphic electronic systems. Proc. IEEE 78, 1629–1636.doi: 10.1109/5.58356

© 2018 Tous droits réservés.

1.7 References

(Merolla et al., 2014) Merolla, P. A., Arthur, J. V, Alvarez-icaza, R., Cassidy, A. S., Sawada, J., Akopyan, F., ... Modha, D. S. (2014). A million spiking-neuron integrated circuit with a scalable communication network and interface. Sciencemag.Org, 345(7812), 668–673. https://doi.org/10.1126/science.1254642

(Monroe, 2014) D. Monroe, "Neuromorphic computing gets ready for the (really) big time," Communications of the ACM, vol. 57, no. 6, pp. 13–15, 2014.

(McCulloch and Pitts, 1943) W.S. McCulloch and W. Pitts. A logical calculus of ideas immanent in nervous activity. Bulletin of Mathematical Biophysics, 5, 1943.

(Noor, 2014) K.Noor "Potential of Cognitive Computing and Cognitive Systems", Vison article. October 2014; DOI: 10.1515.

(Obama, 2013) Fact Sheet: BRAIN Initiative, White House, http://www.whitehouse.gov/the-press office/2013/04/02/fact-sheet-brain-initiative

(Olazaran, 1996) Olazaran M. (1996), "A Sociological Study of the Official History of the Perceptrons".

(Scharre et al., 2018) Scharre, D. W., Weichart, E., Nielson, D., Zhang, J., Agrawal, P., Sederberg, P. B., … Initiative, for the A. D. N. (2018). Deep Brain Stimulation of Frontal Lobe Networks to Treat Alzheimer's Disease. *Journal of Alzheimer's Disease*, *62*(2), 621–633. https://doi.org/10.3233/JAD-170082

(Schuman et al., 2017) Schuman, C. D., Potok, T. E., Patton, R. M., Birdwell, J. D., Dean, M. E., Rose, G. S., & Plank, J. S. (2017). A Survey of Neuromorphic Computing and Neural Networks in Hardware, 1–88. https://doi.org/10.1016/j.neucom.2010.03.021

(Turing, 1936) Turing, A. 1936. On computable numbers, with an application to the Entscheidungsprob- lem. *Proceedings of the London Mathematical Society* 2.1, 230-265.

(Vuillaume et al., 2013) Dominique Vuillaume et al,"Synaptic electronics,"IOP science.2013:380201

(Wang & Raj 2017) Wang, H., & Raj, B. (2017). On the Origin of Deep Learning, 1–72. https://doi.org/10.1139/f56-020

(Waldrop, 2016) Waldrop, M. M. (2016). The chips are down for Moore's law. Nat. News 530:144.doi: 10.1038/530144a

(WSTS, 2017) https://www.wsts.org

© 2018 Tous droits réservés.

Chapter 2.

Neurons modeling

© 2018 Tous droits réservés.

Thèse de Sara Hedayat, Université de Lille, 2018

© 2018 Tous droits réservés.

lilliad.univ-lille.fr

In this chapter, the different part of a neuron cell will be identified and the functionality of each of these specialized regions will be briefly explained. Next, an overview of mathematical models, which attempt to describe the behavior of the neuron cell, will be presented. Finally, three biophysical models and their simulation results will be described. These models will be used for the design of an ultra-low power artificial neuron, which is the basic element of future artificial neural networks.

2.1 Neuron and neuronal membrane

2.1.1 Glial and neuron cell

All organs of the human body are composed of cells. The specific functions of cells and their interactions determine the functions of organs. This is also true for the most sophisticated organ, the human brain. We can define two main types of cells in the human brain, glial cells and neurons. This chapter will emphasize on the structure of different nervous types of cells, mostly neurons in our case. Glial cells fill the space between the neurons maintaining the homeostasis process, make myelin and play a role in supporting and protecting nervous tissue providing nutrients and oxygen. They eliminate dead cells and fight pathogens. The exact role of glial cells remain still obscure, and it is generally admitted that neurons play a more important role, in particular regarding their contribution to produce and transmit the electrical impulses. This is the ‘neuron doctrine’ a discovery due to decisive neuro-anatomical work of Cajal (Andres-Barquin, 2001).

There is an impressive number of neurons in the human brain, about 100 billion. Neurons are excitable cells and specialized in the reception, integration and transmission of information. Information flows in the form of action potential also called spike. All the activity of our nervous system is based on the transmission of these nerve impulses between neurons. There are various types of neurons, which differ in morphology and functionality **(Figure 2.1)** (Lodish et al, 2000).

© 2018 Tous droits réservés.

lilliad.univ-lille.fr

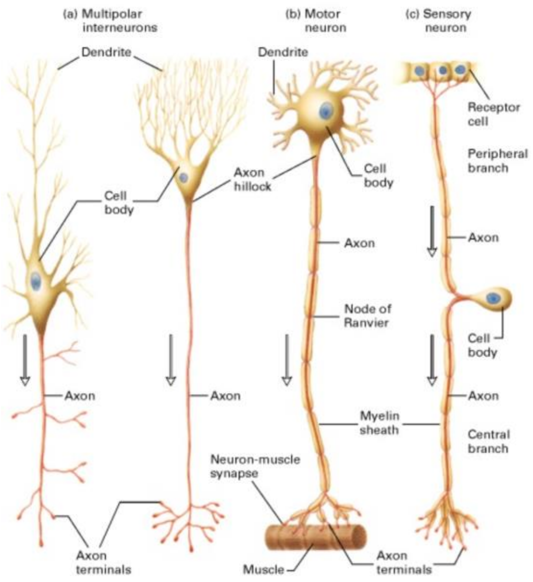

Figure 2.1 Different types of neurons.
(a) Multipolar interneurons. (b) Motor neuron.
(c) Sensory neuron (Lodish et al, 2000).

A typical neuron is composed of a cell body and different extensions differing in functionality and size. Indeed, four main parts can be identified for one neuron: cell body also called soma, axon, dendrites and axonal terminals known as synapses **(Figure 2.2)**. All these specialized regions constitute a very dense network that allows permanent and coordinated exchanges between neurons.

© 2018 Tous droits réservés.

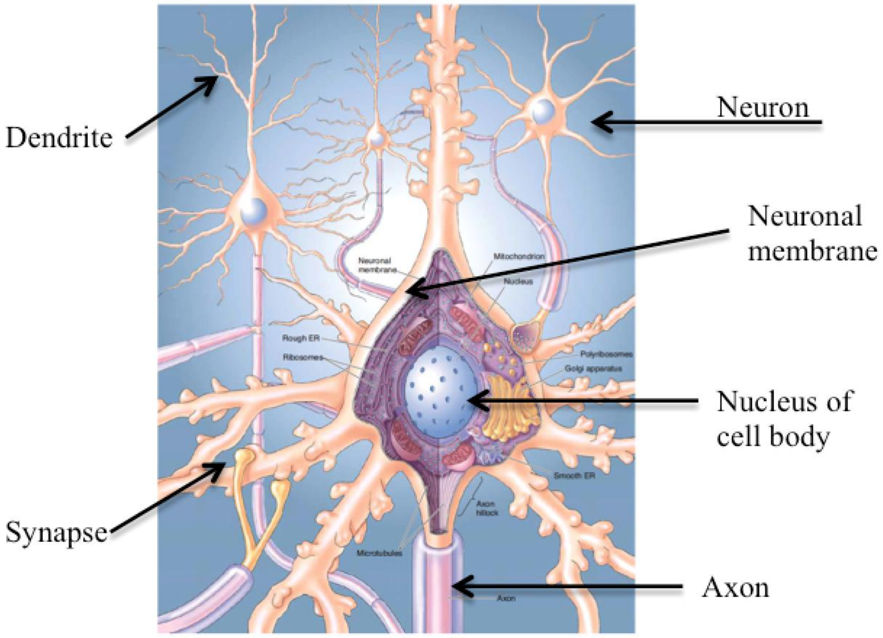

Figure 2.2 Neuron internal and external parts. Neuron, neuronal membrane, nucleus of cell body, axon, synapse and dendrite. (Bear et al, 2007).

2.1.2 Neuron cell body and axon

As we look into the cell body, we can find the cell nucleus **(Figure 2.2)**, which contains the DNA. The cell body is the place of synthesis of almost all neuronal proteins and membranes molecules (Lodish et al, 2000).

Almost every neuron has a single axon **(Figure 2.2)**. The diameters of the axon can vary from micrometers in certain nerves of the human brain to millimeters in the nerves of squid (Lodish et al, 2000). The main function of axon can be assimilated to a one-way road, which allows the conduction of spikes from the cell body to the axon terminals.

2.1.3 Neuron dendrites and synapses

The cell body is surrounded by multiple branches, which play the role of a messenger receiver. Generally known as dendrites **(Figure 2.2)**, they receive chemical signals from other neurons, convert it to electrical impulses, and finally transmit them into the cell body.

The information transfer between two neurons takes place in a specialized region called synapse **(Figure 2.2)**. Synapses are located between an axon terminal of a neuron and a dendrite of an adjacent neuron. Generally, there are two types of synapses: chemical and electrical. The chemical synapses send impulses via neurotransmitters. The electrical synapses are like tunnels; ions are transferred via hydrophilic channels also called gap junction channels **(Figure 2.3)**.

© 2018 Tous droits réservés.

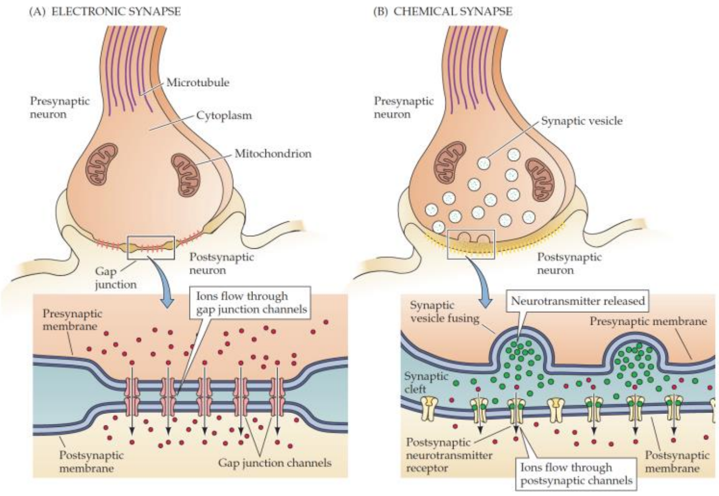

Figure 2.3 Different types of synapses. (A) Electronic synapse. (B) Chemical synapse. (Purves et al, 2004)

2.1.4 Neuronal membrane and ion channels

The intercellular connections, synapses, consist of a very thin cleft located between two fragile membranes. In fact, each membrane surrounds the neuron and forms the outer boundary of the neuron cell. Thanks to the fluidity of the membrane, the neurotransmitters diffuse across the synaptic cleft allowing the transmission of nerve impulses. When the neurotransmitter binds to the receptor, changes in the ion permeability of the postsynaptic plasma membrane is involved, leading to the membrane electric potential changes at this location. Depending on the type of postsynaptic cell, this electric fluctuation can induce an action potential for a neuron, a contraction in a muscle or even hormone secretion in case of a gland cell.

The creation and propagation of action potential is based on the ions flow across their plasma membranes highlighting that the neuronal membrane plays a fundamental role in the nervous system **(Figure 2.2)**. As mentioned before by delimiting the neuron cell, it contains the cytoplasm inside the neuron and maintains certain substances outside the neuron. This neuronal membrane is about 5 nm thick. It is composed of two layers of lipid molecules with many protein structures embedded in the membrane. Some of these proteins called ion transporters or pump channels maintain a gradient (Bear et al, 2007), i.e. a difference in ionic concentrations between the intracellular space and the extracellular space of the neuron cell. Other specific proteins form ion channels, which select certain substances that can penetrate through the neuronal membrane **(Figure 2.4).** Both ion transporters and ion channels are necessary to describe the generation and propagation of action potential.

© 2018 Tous droits réservés.

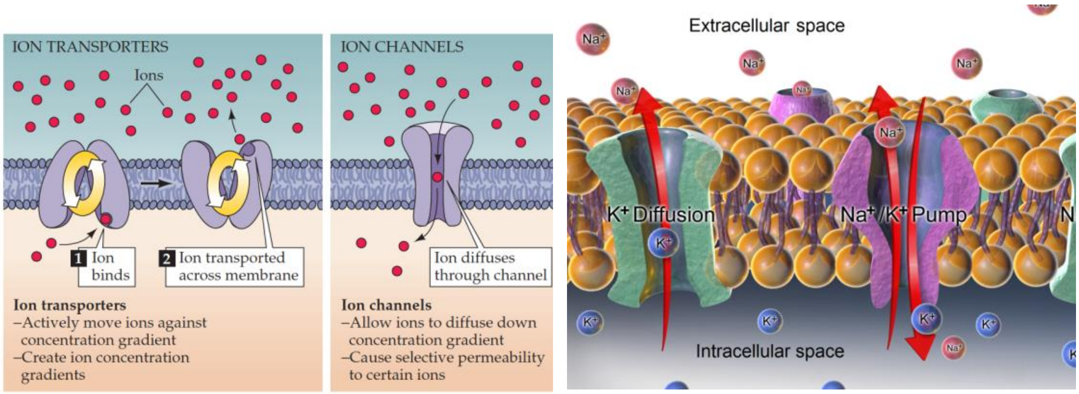

Figure 2.4 Neuronal membrane. Left: comparison of ion transporters with ion channels. Right: simplified schematic of the neuronal membrane with principal channels and principal ionic concentrations (Na^+ and K^+) (Bear et al, 2007).

2.1.5 Neuronal membrane and the action potential

In this part, we will describe the variation of the action potential according to the exchange of ionic charges through the neuronal membrane. It is worth mentioning that the difference in electric potential between the interior and exterior of a neuron cell is called the membrane potential. This term will be used in the next paragraphs.

At rest, there is a negative potential difference around -65mV between the intracellular surface of the neuron membrane and its extracellular surface called the resting potential (Bear et al, 2007). This resting potential results from a concentration gradient of sodium ions Na^+ and potassium ions K^+ between the inside and the outside of the neuron. In fact, in resting state Na+ ions have a higher concentration in the extracellular space than the intracellular space. On the contrary, K^+ ions have a higher concentration in the intracellular space than the extracellular space. For each ion, the reversal potential (also known as Nernst potential) is the membrane potential for which there is no net flow of that particular ion from one side to another side of the neuronal membrane. At equilibrium the Nernst potential for potassium and sodium ions are respectively E_K=-77mVand E_{Na}=+50mV.

The action potential is characterized by a fast and localized modification of the permeability of the neuron's membrane: Na^+ enters into the cell using ion channels selectively permeable to sodium. The membrane potential takes then a positive value, about +40 mV, close to the Nernst potential of sodium (E_{Na}). It is illustrated as the depolarization phenomena in **Figure 2.5**.

© 2018 Tous droits réservés.

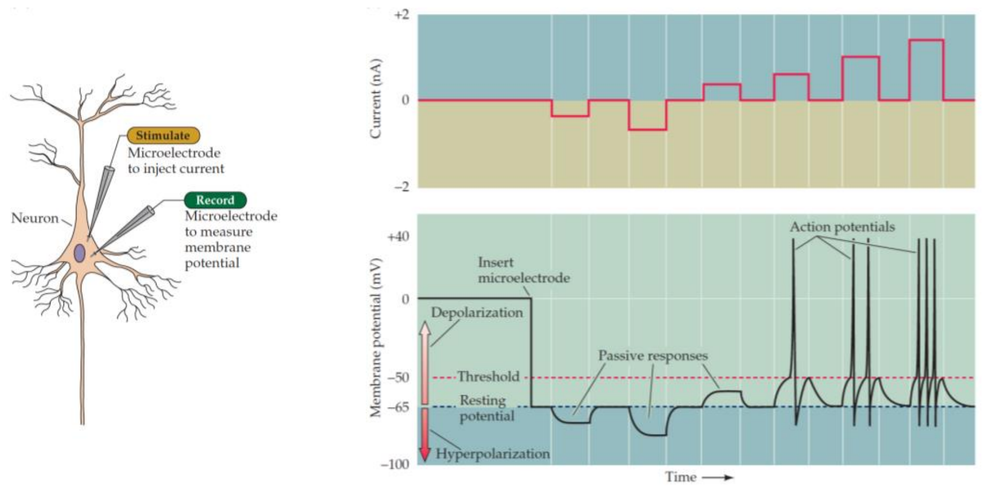

(A) (B)

Figure 2.5 The evolution of membrane potential. (A) Neuron and electrodes to stimulate and record the neuronal membrane. (B) Injected current and (C) the membrane potential evolution in time (Purves et al, 2004).

Then, potassium ions (K^+) leave very quickly the cell, passing through dedicated ion channels. The membrane potential decreases to a lower value than the resting potential, which defined the repolarization and then hyperpolarization sequences. Finally, the membrane potential reaches its initial resting state. All these variations of the action potential last only a few milliseconds in living cells.

This localized and transient nerve impulse, which is mostly generated in a region of the cell body called axon hillock, propagates along the neuron axon. In fact, action potentials can originate not only at the axon hillock, but also in the axon initial segment, 30 to 40µm from the soma and close to the first myelinated segment. In some neurons, the action potential even originates at the first node of Ranvier (**Figure 2.6)**, where sodium channels are highly concentrated. For both myelinated and unmyelinated axons, once the action potential begins in the axon, it is not only propagating toward the nerve terminals but also back into the soma and dendrites (Caldwell, 2010).

The myelination of the axon impacts the propagation speed of an action potential. In fact the unmyelinated axon conduction velocities range from about 0.5 to 10m/s, while the myelinated axons can conduct at velocities of up to 150m/s (Purves et al, 2004).

© 2018 Tous droits réservés.

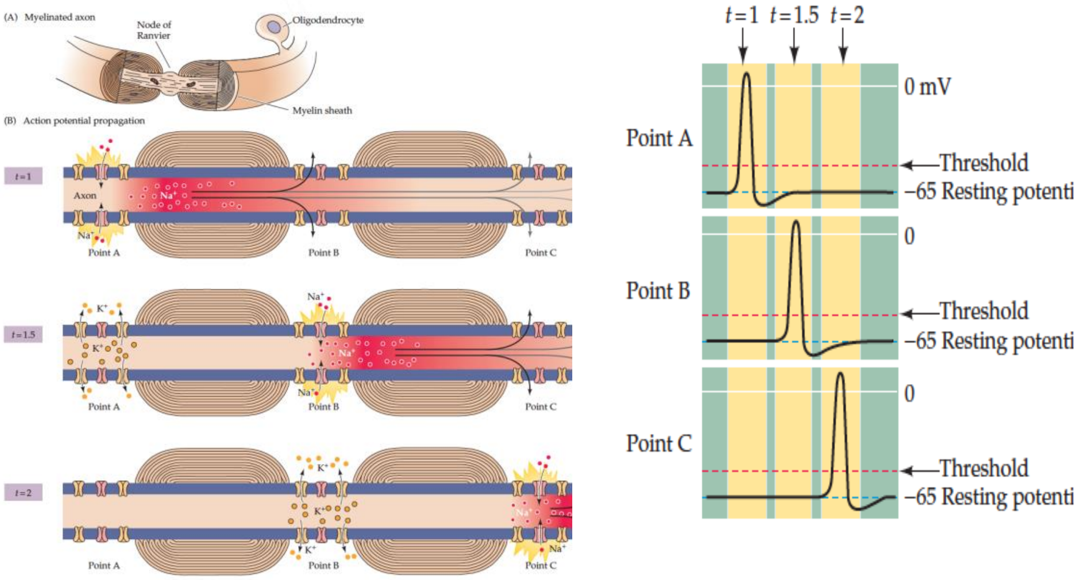

Figure 2.6 Propagation of action potential in the neuronal membrane. Left:(A) Myelinated axon. (B) Action potential propagation. Right: (A) Action potential at t = 1ms. (B) Action potential at t = 1.5ms. (A) Action potential at t = 2ms (Purves et al, 2004).

Previously, the different regions of a neuron cell were presented. The generation and propagation of spike due to the mechanism of ionic channels in the neuronal membrane have been defined. In the next section, mathematical models of the neuronal membrane will be described.

© 2018 Tous droits réservés.

2.2 State of the art: spiking neuron models

In many fields, science tries to explain the existing phenomena using physical equations. This is the case for the neuronal membrane where many scientists try to explain the generation of spike using more or less complex mathematical models. Several neuronal membrane models have been proposed over the time. These models, also called spiking neuron models, are a mathematical description of the generation of spikes in cells as a function of the properties of their membrane. They are designed to accurately describe biological processes.

Investigated in 1907 by Lapicque, the Integrate-and-fire (I&F) is one of the most widely used models in computational neuron science. Also known as the simplest neuron model, it describes relation between the current and the membrane potential. When an excitatory current is applied, the membrane voltage increases until it reaches a threshold. Since I&F, more complex models had been developed: leaky integrate and fire, I&F with adaptation, I&F or burst, quadratic I&F. However, they are not complete enough to describe with a good accuracy the complexity of spiking behavior of individual neurons in response to excitatory current pulses.

Models such as FitzHugh Nagumo in 1961, Morris-Lecar in 1981, Hindmarsh Rose in 1984, Wilson and Izhikevich in 2003, are more efficient to reproduce the neuro-computational properties of biological spiking neurons. In 2004, a comparison of these neuronal models has been investigated by Izikevich (Izhikevich, 2004) **(Figure 2.7)**.

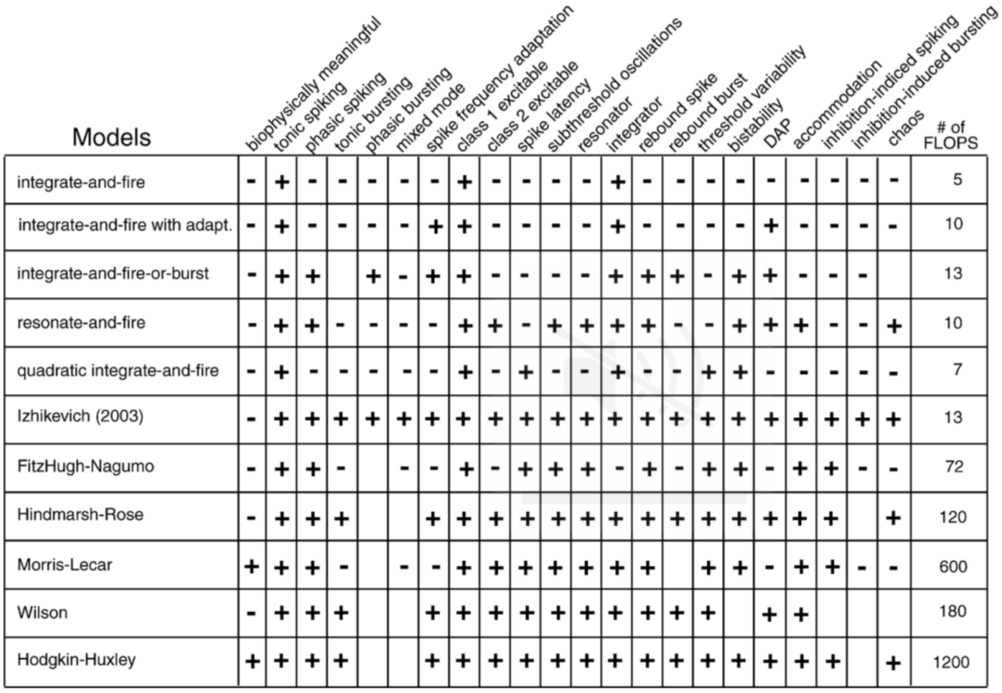

Models	biophysically meaningful	tonic spiking	phasic spiking	tonic bursting	phasic bursting	mixed mode	spike frequency adaptation	class 1 excitable	class 2 excitable	spike latency	subthreshold oscillations	resonator	integrator	rebound spike	rebound burst	threshold variability	bistability	DAP	accommodation	inhibition-indiced spiking	inhibition-induced bursting	chaos	# of FLOPS
integrate-and-fire	-	+	-	-	-	-	-	+	-	-	-	-	+	-	-	-	-	-	-	-	-	-	5
integrate-and-fire with adapt.	-	+	-	-	-	-	+	+	-	-	-	-	+	-	-	-	-	+	-	-	-	-	10
integrate-and-fire-or-burst	-	+	+		+	-	+	+	-	-	-	-	+	+	+	-	+	+	-	-	-		13
resonate-and-fire	-	+	+	-	-	-	-	+	+	-	+	+	+	+	-	-	+	+	+	-	-	+	10
quadratic integrate-and-fire	-	+	-	-	-	-	-	+	-	+	-	-	+	-	-	+	+	-	-	-	-	-	7
Izhikevich (2003)	-	+	+	+	+	+	+	+	+	+	+	+	+	+	+	+	+	+	+	+	+	+	13
FitzHugh-Nagumo	-	+	+	-		-	-	+	-	+	+	+	-	+	-	+	+	-	+	+	-	-	72
Hindmarsh-Rose	-	+	+	+			+	+	+	+	+	+	+	+	+	+	+	+	+	+		+	120
Morris-Lecar	+	+	+	-		-	-	+	+	+	+	+	+	+		+	+	-	+	+	-	-	600
Wilson	-	+	+	+			+	+	+	+	+	+	+	+	+	+		+	+				180
Hodgkin-Huxley	+	+	+	+			+	+	+	+	+	+	+	+	+	+	+	+	+	+		+	1200

Figure 2.7 Comparison of spiking neuronal models (Izhikevich, 2004).

As shown in **Figure 2.7** the most attractive and meaningful model is the Hodgkin and

© 2018 Tous droits réservés.

Huxley model (HH) proposed in 1952 (Hodgkin and Huxley, 1952). It is the first model to describe the generation of one spike based on the experimental studies of the neuronal membrane. HH model will be presented in the next section.

Several mathematical models have been proposed after the Hodgkin-Huxley model in order to describe the spiking activity in living membranes. These refined models are also based on channel-based equations. Most of these models were designed by introducing extra-ionic channels and by adding corresponding terms to the original HH equation.

In this work, three neuronal membrane models were investigated. First, the widely known and pioneer Hodgkin and Huxley model, which studies the properties of the giant squid axon. Second, the Wei model which proposes a precise model for the human neuron cell to describe the unification of neuronal spikes. Finally, the Morris-Lecar model attracted our attention as it gathers both criteria of biophysically meaningful and simplicity. A description of these models and the simulation results are presented in the next section.

2.3 Investigation of biophysical neuron models

2.3.1 Hodgkin and Huxley model

In this section, the Hodgkin Huxley model, called HH model, will be investigated. Hodgkin, Huxley and Eccles received the 1963 Nobel Prize in Physiology or Medicine for their discoveries concerning the ionic mechanisms involved in the initiation and propagation of the spike in the peripheral and central portions of the nerve cell membrane **(Figure 2.8)** (Schwiening, 2012).

Figure 2.8 The cover of the 1963 Nobel Prize Program. Huxley, left, looks on as Hodgkin adjusts a brand-new Tektronix 502A oscilloscope (Schwiening, 2012).

© 2018 Tous droits réservés.

As shown in **Figure 2.9,** they were also the first ones who observed one potential action by introducing an electrode into the giant squid axon. The 500µm diameter of this axon allows the rapid conduction (the speed increases as the square root of the diameter) of action potentials driving a fast response.

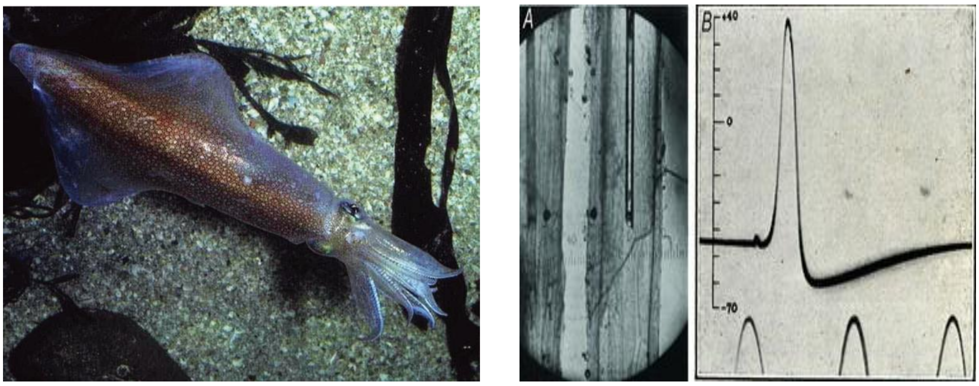

Figure 2.9 Intracellular recording of the squid giant axon action potential. Left: Loligo forbesi, the 60cm long squid. Right: (A) Photomicrograph of an electrode inside a squid giant axon. (B) The first intracellular recording of an action potential. The sine wave under the spike has a frequency of 500 Hz (Schwiening, 2012).

Based on these in vivo measurements and the results described in Hodgkin and Huxley's 1952 publication, it is suggested that the electrical behavior of the neuronal membrane can be represented by the electrical circuit shown in **Figure 2.10**.

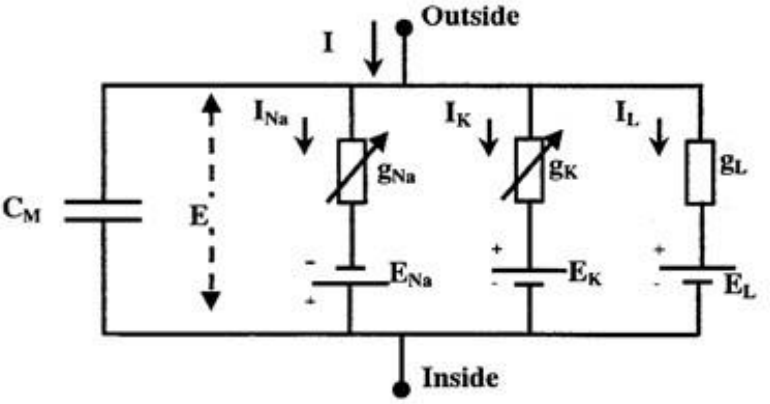

Figure 2.10 The electrical circuit proposed by Hodgkin and Huxley representing the neuronal membrane. Currents, potassium conductance (g_K) and sodium conductance (g_{Na}) varies with the membrane potential. The other components have constant values (Hodgkin and Huxley, 1952).

The non-linear differential equations of Hodgkin and Huxley constitute the reference model for any other scientist seeking to understand the operation of a neuron. This model is important not only because the parameters have a biophysical meaning and

© 2018 Tous droits réservés.

are measurable, but also because they allow us to study issues related to synaptic integration, dendritic cable filtering, the effects of dendritic morphology, the interaction between ionic currents, and other issues related to the dynamics of a neuron and its neuronal membrane.

The Hodgkin and Huxley model is defined by four differential equations coupled to each other. The target of this paragraph is to explain the link between HH equations and their biological meaning.
Based on the HH electrical circuit shown in **Figure 2.10,** the total current (I) is the result of two main contributions that are the charge of the membrane capacitance (C_M) and the ion currents (I_{ion}) crossing the membrane through the ion channels (Eq.2.1). The ion currents result from the addition of sodium and potassium currents ($I_{Na} and\ I_K$), and a leakage current (I_l) (Eq.2.1).

$$I = C_M \frac{dV_m}{dt} + I_{ion}$$
$$I_{ion} = I_{Na} + I_K + I_l$$
Eq.2.1

Each of these currents (I_{Na}, I_K and I_l) is determined by a driving force that can be conveniently modeled as an electrical potential difference and a coefficient permeability that has the dimension of a conductance. As shown in Eq.2.2, the potassium current (I_K) is equal to the potassium conductance (g_K) multiplied by the difference between the membrane potential (V_m) and the equilibrium potential of the potassium ion also known as Nernst potential (E_K) (Hodgkin and Huxley, 1952). Sodium current (I_{Na}) also depends on the sodium conductance (g_{Na}), the membrane potential (E or V_m) and the sodium Nernst potential (E_{Na}). This definition is also true for I_l (expression of I_{Na}, I_K and I_l in annex).

$$I_K = g_K(V_m - E_K)$$
Eq.2.2

Hodgkin and Huxley experiment suggests that g_K and g_{Na}, varies with the membrane potential and time; but E_{Na}, E_K, E_l, C_M and g_l can be considered as constant (values in annex).
The potassium conductance g_K is defined by the Eq.2.3, where $\bar{g}_K$ is the maximal potassium conductance, n is a gating variable ranging between 0 and 1. The gating variable n is defined by a first order differential equation depending on two rate constants α_n and β_n, which varies only with Vm (annex).

$$g_K = \bar{g}_K n^4$$
$$\frac{dn}{dt} = \alpha_n(1-n) - \beta_n n$$
Eq.2.3

© 2018 Tous droits réservés.

Sodium conductance g_{Na} (expression in annex) is defined in the same way except that it depends on other gating variables m and h (Eq.2.4). Where m is associated with sodium channel activation and h corresponds to the sodium channel inactivation. The expression of their respective α and β are presented in annex.

Finally, by replacing the expression of each conductance (g_K, g_{Na} and g_l) in their respective ionic current (I_K, I_{Na} and I_l) and gathering the three gating variables (n, m and h) we can obtain the four main equations of HH model (Eq.2.4) (Hodgkin and Huxley, 1952).

$$
\begin{gathered}
I = C_M \frac{dV_m}{dt} + \bar{g}_K n^4 (V_m - E_K) + \bar{g}_{Na} m^3 h (V_m - E_{Na}) + g_l (V_m - E_l) \\
\frac{dn}{dt} = \alpha_n (1 - n) - \beta_n n \\
\frac{dm}{dt} = \alpha_m (1 - m) - \beta_m m \\
\frac{dh}{dt} = \alpha_h (1 - h) - \beta_h h
\end{gathered}
\tag{Eq.2.4}
$$

Based on HH equations previously described the numeric resolution of this model with Matlab software, was investigated. The Matlab code of HH model was found in the literature (Siciliano, 2012). The constant parameters as well as the equations are extracted from (Hodgkin and Huxley, 1952) and the results are presented in the next paragraph.

2.3.1.1 Results of HH model: threshold excitatory current

The excitability of the neuron is defined as its ability to produce a spike in response to a stimulus. The generation of spike depends on the excitatory current and its duration, which follows the principle of excitability of the neuron. we define the threshold excitatory current as the required current to generate only one spike for a given time. **Figure 2.11.Left** shows a threshold excitatory current with 7µA/cm^2 amplitude (Iex) and 5ms pulsed duration (Ts). For this excitation, the variation of ionic currents are presented versus time in **Figure 2.11.Right**. The maximum sodium current (I_{NaMax}) is around -782µA/cm^2 and the maximum potassium current (I_{KMax}) is around 822µA/cm^2. The leakage current (I_L) is negligible compared to both I_{Na} and I_K.

© 2018 Tous droits réservés.

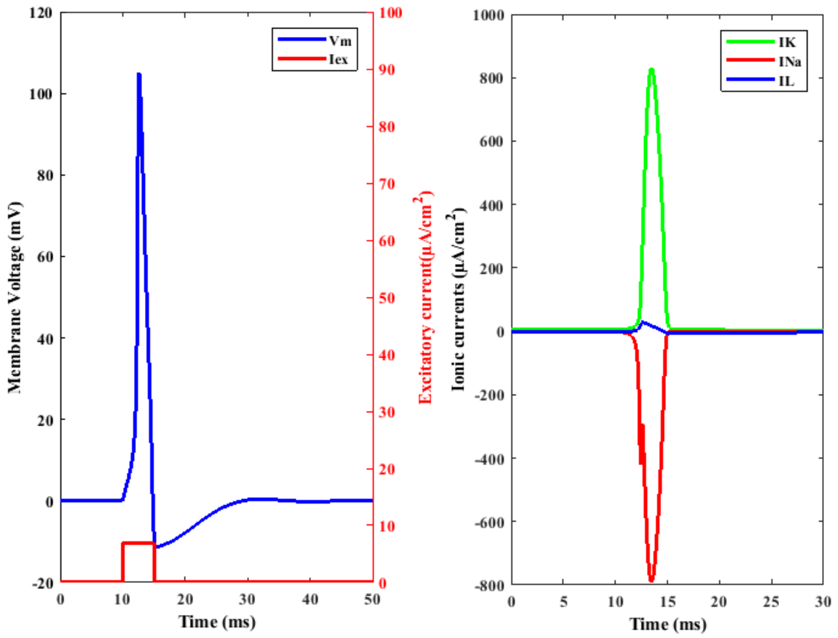

Figure 2.11 Generation of one spike with HH model. Left: Membrane voltage for a pulsed excitatory current with Iex = 7µA/cm^2 and Ts = 5ms. **Right:** Ionics currents, I_{Na} I_K and I_L.

From this basic behavior, the excitability of the squid's neuronal membrane was investigated by increasing the threshold current amplitude and its time duration (**Figure 2.12**). In fact, this study was driven to monitor the number of spikes generated in the time domain versus the injected excitatory current.

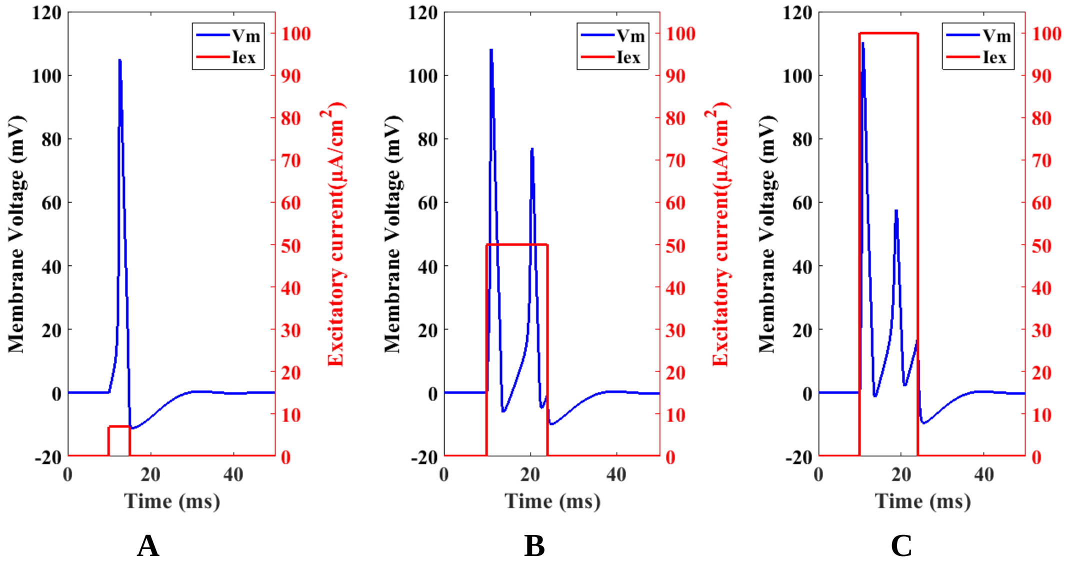

Figure 2.12 Excitability property of the neuronal membrane for HH model.

© 2018 Tous droits réservés.

The response of the HH model, determined at the threshold excitatory current I_{ex} = 7µA/cm^2 during T_s = 5ms (**Figure 2.12.A**), was kept as a reference. As we increase I_{ex} to 50µA/cm^2 and T_s to 14ms, a second spike is generated (**Figure 2.12.B**). A third partial spike is observed for I_{ex} = 100µA/cm^2 and T_s = 14ms (**Figure 2.12.C**).

This study demonstrates the influence of the amplitude and the duration of the pulsed excitatory current in the generation of spikes. To complete this work, we have investigated different pulsed currents, in terms of amplitude and pulsed duration, and conclude that the number of charges induced into the neuronal membrane is the main criteria to obtain a spike train. A detailed result will be presented in a next section (2.3.2.3 Injected charge).

2.3.1.2 Monte Carlo comparison

In the frame of a collaboration with a team of Salamanca University, a stochastic model based on the Monte Carlo (MC) technique was also used to solve HH equations (Vasallo et al, 2017). MC model is based on the probabilities for the different ions to cross the cell membrane. Sodium, potassium and leakage channels are introduced in the model according to the Hodgkin and Huxley equations. As it can be seen in **Figure 2.13**, Matlab and Monte Carlo simulations of HH equations are in good agreement.

© 2018 Tous droits réservés.

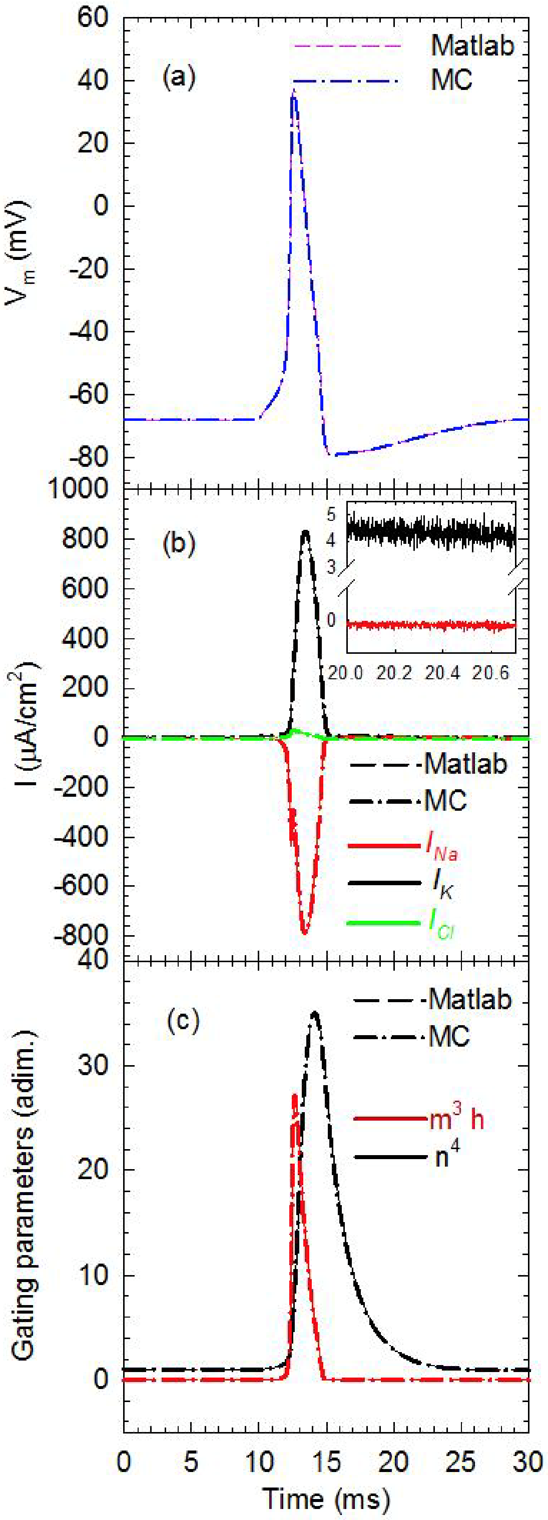

Figure 2.13 Comparison between MC and Matlab solver of HH model for. (a) Membrane voltage V_m. (b) Ionics currents I_{Na}, I_K and I_{Cl}. (c) Sodium (m^3h) and potassium (n^4) gating variables. For all cases an excitation of $I_{app} = 7\mu A/cm^2$ and $T_s = 5ms$ starting at 10ms is used (Vasallo et al, 2017).

© 2018 Tous droits réservés.

Figure 2.13 represents the time variation of membrane voltage, ionic currents, sodium (m^3h) and potassium (n^4) gating variables in response to a pulsed excitatory current (Iapp) applied at 10ms with 7µA/cm2 amplitude and 5ms of duration. During the first 10ms, where Iapp is equal to zero, the neuronal membrane is in a steady state. At the onset of Iapp, sodium channels open more rapidly than potassium channels (m3h increases, Figure 2.13.c). It induces the flow of sodium ions into the cell, resulting in a negative I_{Na} (**Figure 2.13.b**), which leads to the increase of V_m (**Figure 2.13.a**). The rise of V_m will result to the slow opening of potassium channels (shifted n^4 increases, **Figure 2.13.c**) leading to the exit of potassium ions from the intracellular space to extracellular space and a positive I_K arises (**Figure 2.13.b**). As V_m reaches its peak value, around +40mV, sodium channels start to close (m^3h decreases, **Figure 2.13.c**), the slow potassium channels are completely open and potassium ions rush out from the intracellular space to the extracellular space and the voltage quickly returns to its resting value. As the potassium channels are closing slowly, potassium ions continue to leave the cell, resulting in a negative overshoot called hyperpolarization. The resting membrane potential is slowly restored thanks to the diffusion and leakage channel (I_{Cl}). During the action potential generation and a short time after the recovery of the steady state, it is impossible to stimulate the neuronal membrane in order to fire again. In fact, the period from the initiation of the spike to immediately after the peak is referred as the absolute refractory period. During this time, the cell cannot produce any new action potential.

The generation of one spike obtained by the Matlab and MC resolution of HH model seems to be exactly the same, despite the stochasticity in the MC model. However, a closer look at the MC results corresponding to a zoom of I_{Na} and I_K (inset in **Figure 2.13.b)** reveals the presence of fluctuations in the ion currents that is the signature of a channel noise (Vasallo et al, 2017). It is interesting to note that the same results have been obtained with Matlab and MC for the resolution of HH model.

© 2018 Tous droits réservés.

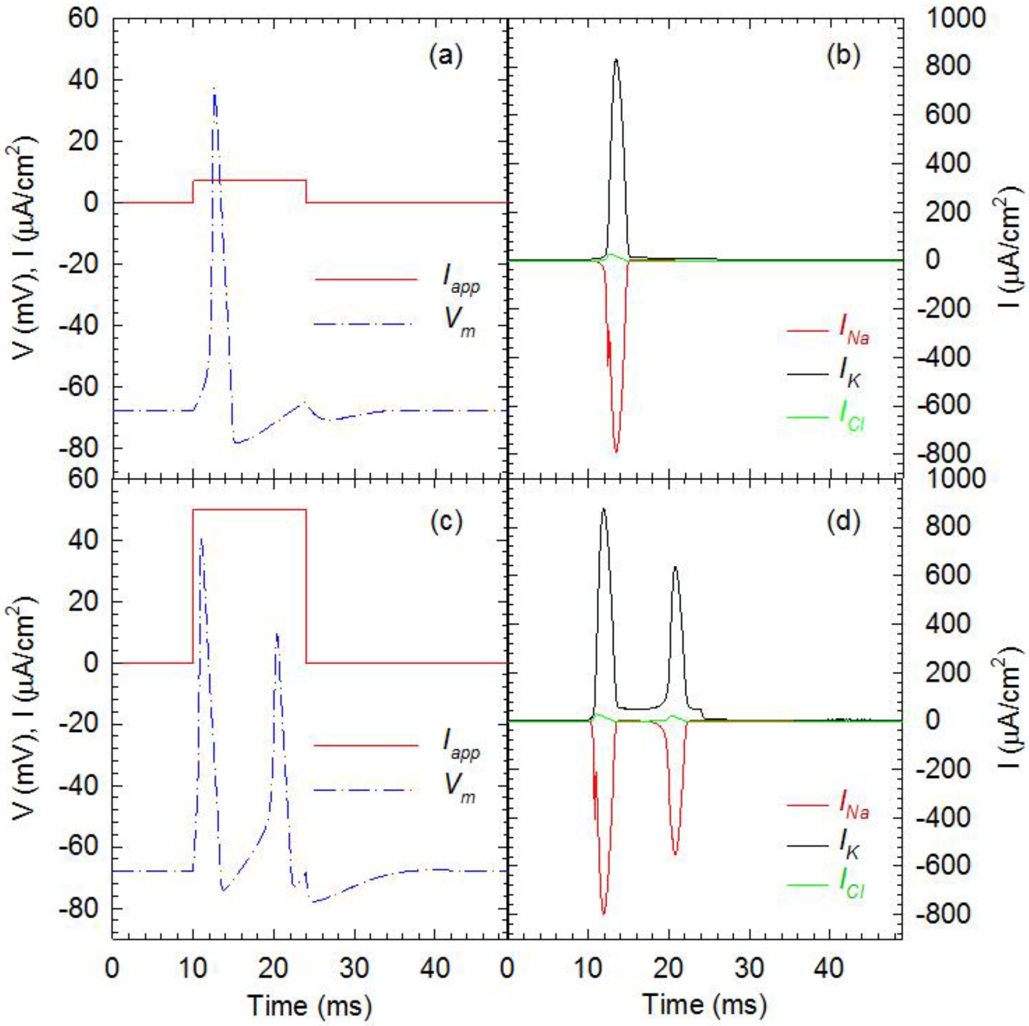

Figure 2.14 MC time evolution of various neuronal membrane parameters. (a) Membrane voltage V_m for I_{app}= 7μA/cm^2 and T_s = 14ms. **(b)** Ionic currents for I_{app} = 7μA/cm^2 and T_s = 14ms. **(c)** Membrane voltage V_m for I_{app} = 50μA/cm^2 and T_s = 14ms. **(d)** Ionic currents for I_{app} = 50μA/cm^2 and Ts = 14ms. In all cases, the excitatory current starts at 10ms (Vasallo et al, 2017).

As described in this section, Hodgkin and Huxley succeeded in describing the generation of one spike based on the mechanism of ionic channels present in the neuronal membrane. In their model, the neuronal membrane and the neuron cell is a simplified version of the reality. In the next section, we will investigate the Wei model also based on HH model but with a more detailed description of the neuronal cell.

2.3.2 Limitation of Hodgkin Huxley model and introduction to Wei model

Proposed in 2014, Wei model based on HH model describes several types of generation of spikes, such as epileptic state named "seizure", stable state called "steady stream" and cerebral attack labeled "stroke" (Wei et al, 2014). This model demonstrates that these pathological dynamics, as well as normal spiking behavior of neurons, share a

© 2018 Tous droits réservés.

unified dynamic underpinning. They extend the HH formalism to uncover a unification of neuronal membrane dynamics. The main difference between Wei model and HH model lies in their different hypothesis, which is reflected in their respective equations. **Table 2.1** compares the main equations of Wei model (Eq.2.5) with HH model equations (Eq.2.4).

Main equations of Wei model Eq.2.5	Main equations of HH model Eq.2.4
$C\frac{dV_m}{dt} = -I_{Na} - I_K - I_{Cl} - \frac{I_{pump}}{\gamma}$ $I_K = G_K n^4(V_m - E_K) + G_{KL}(V_m - E_K)$ $I_{Na} = G_{Na} m^3 h(V_m - E_{Na}) + G_{NaL}(V_m - E_{Na})$ $I_{Cl} = G_{ClL}(V_m - E_{Cl})$ $\frac{dq}{dt} = \alpha_q(1-q) - \beta_q q \quad ,q = m,h,n$	$C_M\frac{dV_m}{dt} = -I_{Na} - I_K - I_l$ $I_K = \bar{g}_K n^4(V_m - E_K)$ $I_{Na} = \bar{g}_{Na} m^3 h(V_m - E_{Na})$ $I_l = \bar{g}_l(V_m - E_l)$ $\frac{dq}{dt} = \alpha_q(1-q) - \beta_q q \quad ,q = m,h,n$

Table 2.1 Comparison of Wei model's equations with HH model's equations.

As shown in **Table 2.1,** the Wei model is essentially based on HH model. The variation of the membrane voltage (dV_m/dt) is due to similar ionic currents in both models. The gating variable in both models have also the same equations.

However, and contrary to HH model, the Wei model uses differential equations to describe the variation of the ionic concentrations. For simplicity, we present Eq.2.6, which describes only the potassium concentration outside the cell (NK_0^+) and inside the cell (NK_i^+). Similar equations describe the variation of sodium (NNa_0^+, NNa_i^+) and leakage concentration (NCl_0^+, NCl_i^+) (see annex).

$$\frac{dNK_0^+}{dt} = \frac{1}{\tau}\big(\gamma\beta I_K - 2\beta I_{pump} - I_{diff} - I_{glia} - 2I_{gliapump} + \beta I_{kcc2} + \beta I_{nkcc1}\big)\nu_0 \qquad \text{Eq.2.6}$$
$$\frac{dNK_i^+}{dt} = \frac{1}{\tau}\big(-\gamma I_K + 2I_{pump} - I_{kcc2} - I_{nkcc1}\big)\nu_i$$

These novel equations describing the variation of the ion concentrations proposed by Wei model allows us to study the individual charge conservation, which was not the case for the HH model (global charge conservation). A look into the **Table 2.1**, also shows the presence of an additional current I_{pump} in Wei model.

The Nernst potential defined as constant in HH model (see annex) is more accurate in Wei model since it varies with time. This is due to the Nernst potential definition

© 2018 Tous droits réservés.

defined as a ratio of ion concentrations. The Wei model also takes in account the variation of the neuron volume and the osmotic pressure due to the gradient of the ionic concentration. We can observe the improvements of the Wei model (human neuronal membrane) versus HH model (squid neuronal membrane) in the **Figure 2.15**.

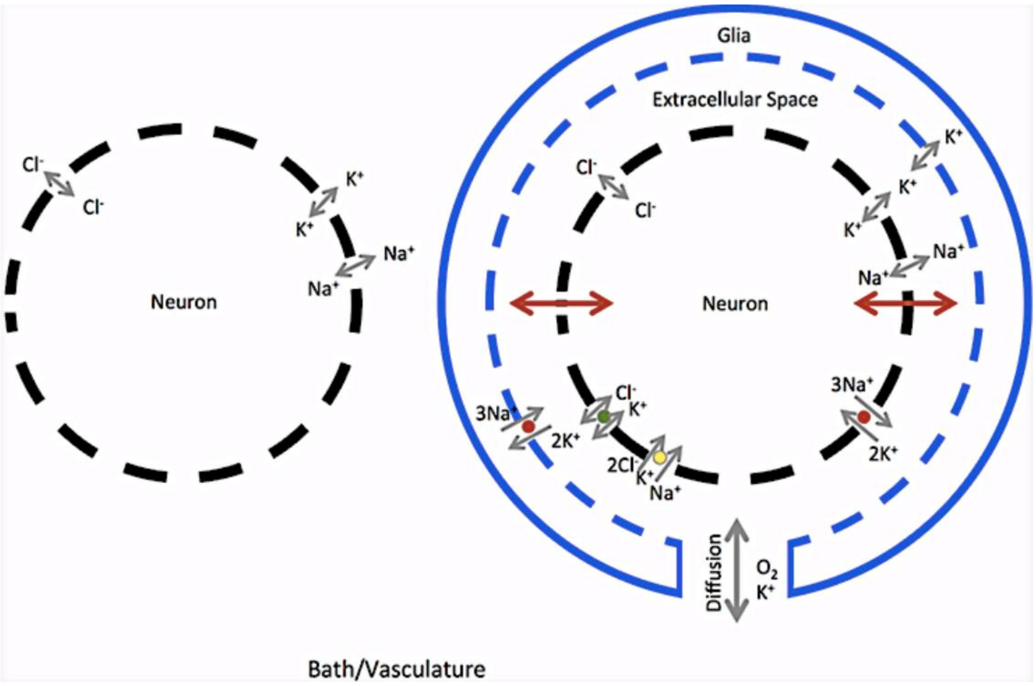

Figure 2.15 Comparison of HH model and Wei model schematic for the neuron cell (Wei et al, 2014).

Investigation of individual charge conservation with Wei model and global charge conservation with HH model enables us to obtain a profound knowledge of the neuronal membrane which is essential for the design of an artificial neuron used in neuro-inspired circuits. In fact, these models, which increase in complexity, give us an overview of what is the reality of a biological neuron and set us the important criteria to take in account to design a neuro-inspired system.

To facilitate the dissemination of their results, the MATLAB code required to reproduce the full model was available and provided by Wei and co-authors. Several modification of the Matlab code has been performed in order to obtain a simple neuro-inspired model. We removed the effects of osmotic pressure, which is not essential for our target. In fact, it is not necessary to reproduce all the neuronal phenomena and pathological dynamics to design a neuro-inspired circuit. This work targets the main and normal biological mechanisms of a neuron cell and the efficient way to reproduce it with nano-electronic devices. As mentioned before, Wei model can reproduce different spiking states, seizure and spreading depression and normal spike train.

© 2018 Tous droits réservés.

According to this, we redefined the variation of intracellular and the extracellular volume to reproduce the normal spiking state.

2.3.2.1 Results of Wei model: threshold excitatory current

Our first study showed that Wei model can generate one spike with Iex = 7µA/cm^2 during 7ms **(Figure 2.16)**.

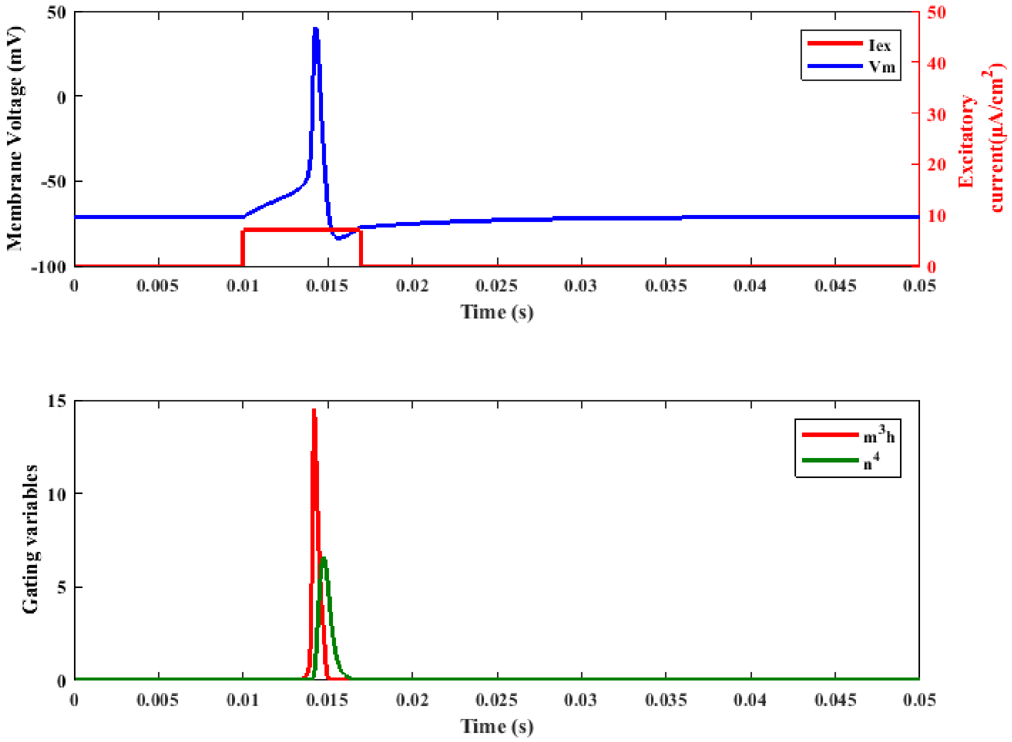

Figure 2.16 Generation of one spike and gating variables with Wei model. Up: One spike is generated for Iex = 7µA/cm^2 and Ts = 7ms. Down: Gating variable m^3h (red) and n^4 (green) for Iex = 7µA/cm^2 and Ts = 7ms.

However, due to the nonlinear differential equations used in the HH and Wei models, it is difficult to determine precisely the threshold current. As it can be seen in **(Figure 2.17),** the Wei model generates one spike for different threshold excitatory currents. **(Figure 2.17.up)** shows the generation of one spike with Iex = 5µA/cm^2 and Ts = 7ms while **(Figure 2.17.down)** illustrates one spike with Iex = 7µA/cm^2 and Ts = 5ms.

© 2018 Tous droits réservés.

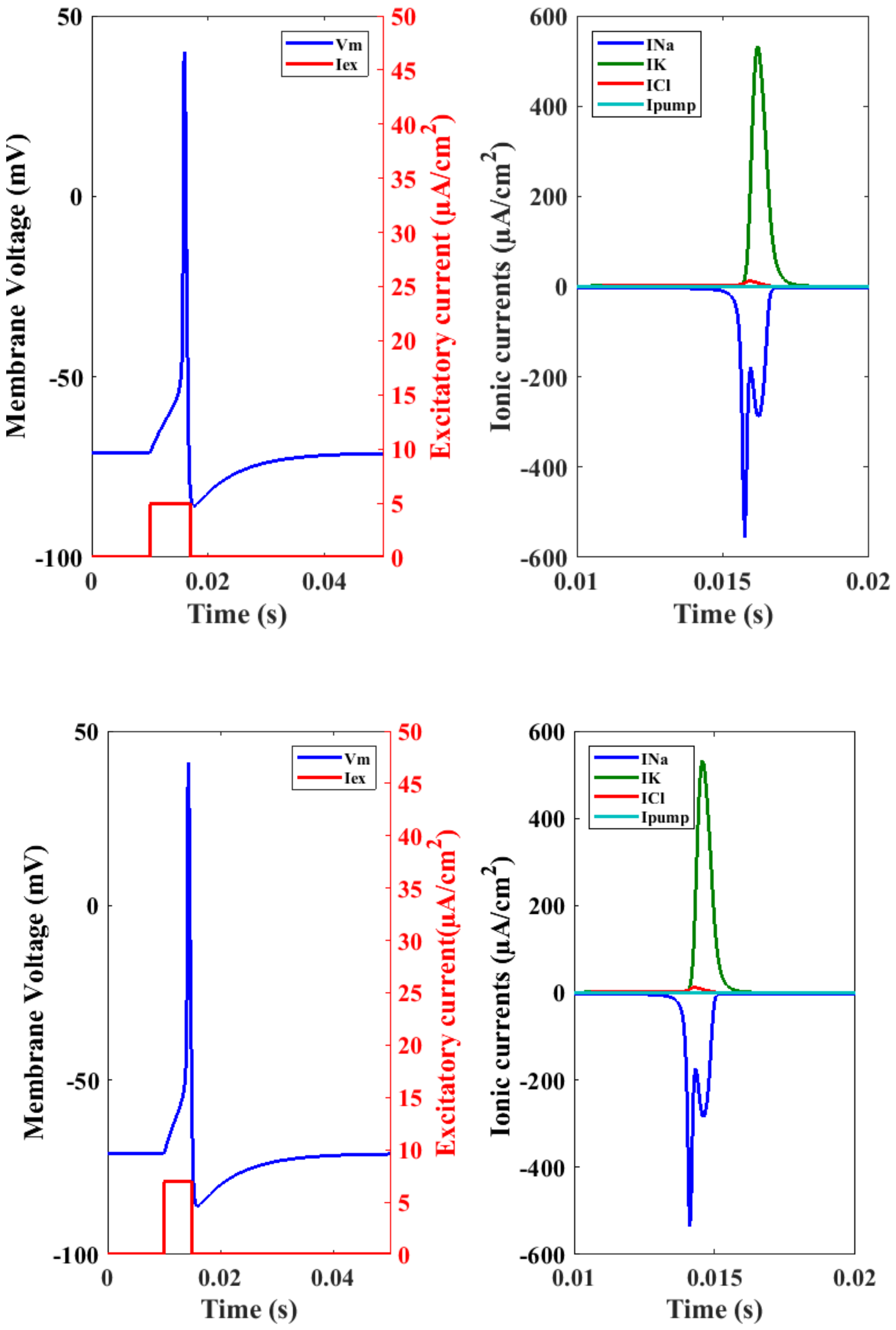

Figure 2.17 Generation of one spike with Wei model. Figure.2.17.up: Vm is generated for Iex = 5µA/cm^2 and Ts = 7ms. **Figure.2.17.down:** Vm is generated for Iex = 7µA/cm^2 and Ts = 5ms.

Based on these results, it can be concluded that the threshold edge is not well defined. This point needs to be more deeply investigated and another way is needed, to establish the boundary. In order to precisely define this value, the effect of injected charge was investigated for the Wei model. This choice is based on how the neuronal membrane of

© 2018 Tous droits réservés.

the soma changes from a resting state to a spiking state, brought by a slight depolarization of the cell body and the charges collected from dendrites.

2.3.2.2 Injected charge

As demonstrated before, since it is difficult to determine the threshold excitation of the neuron as a function of Iex or Ts, another approach is to determine the threshold excitation by the number of injected charges through the membrane (Q), which is defined as follows:

$$Q = \text{Iex}.\text{Ts} \qquad \text{Eq.2.7}$$

In this study, the excitatory current Iex and its duration Ts will vary while the injected charges through the membrane, is kept constant. A constant value Q of 49nC/cm^2 obtained with Iex = 7µA/cm^2 and Ts = 7ms was chosen as a reference. As Iex varies from 3.5µA/cm^2, to 7µA/cm^2 and 14µA/cm^2 and Ts varies from 14ms, 7ms and 3.5ms respectively, the neuron generates one spike for these three cases. It can be concluded that the variation of Iex and Ts does not influence the generation of spike, as the number of charges remains constant (49nC/cm^2). Thus it seems that the excitability of the neuron is related to the quantity of injected charges Q and therefore depends on the product of the excitation current (Iex) by the excitation time (Ts). This new conclusion leads us to investigate the excitability of the neuron when Q is variable. Hence, we define the on-state (Q1S) corresponding to the minimal quantity of charges for which the neuron spikes only once. The work was carried out for different excitatory current values. As shown in **Figure 2.18,** Iex varies from 2µA/cm^2 to 8µA/cm^2 by steps of 1µA/cm^2. The number of charges decreases as the excitatory current increases. Furthermore, as the excitatory current increases the pulsed duration needed to generate one spike decreases.

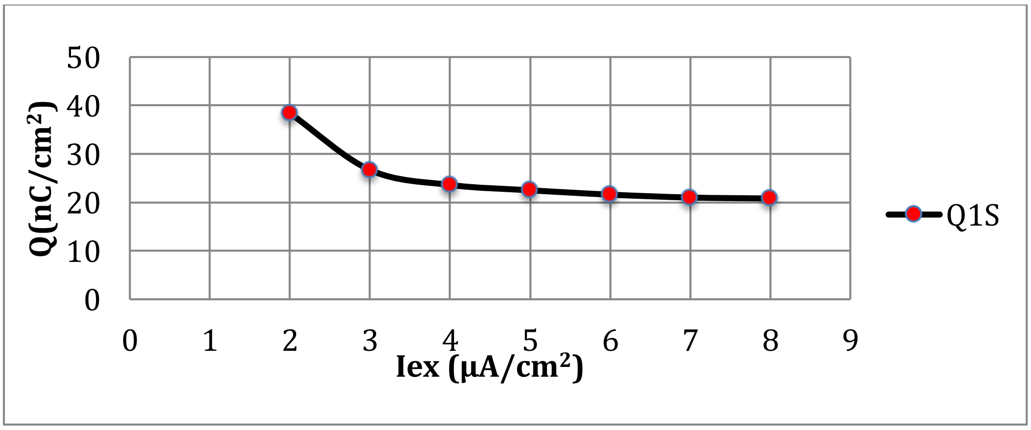

Figure 2.18 Variation of injected charges as a function of different excitatory currents.

© 2018 Tous droits réservés.

This study highlights that the minimum number of charges to obtain one spike is around 21nC/cm^2. As a major conclusion, based on this study, we can determine various excitatory currents to generate only one spike. In fact, a wide range of values can be used for Iex and Ts parameters of the pulsed excitatory current.

2.3.3 Power and energy consumption

One of the main objectives of this thesis is to propose an ultra-low power artificial neuron. Therefore, two different methods to determine the power and energy consumption of a neuron cell will be presented. The first idea consists in estimating the power and energy consumption of one neuron based on the total brain consumption, while the second consists in calculating the power and energy consumption based on ionic currents obtained by HH model and Wei model.

2.3.3.1 Power consumption per spike based on brain consumption

The former method is presented in this paragraph. It is known that the brain represents less than 2% of a person's weight and consumes 20% of the body energy (Drubach, 2000). In addition, the average power consumption of an adult is about 100W (Rigden, 1996). Hence, the total consumption of the human brain is around 20W. The brain has 10^{11} neurons and the overall brain consumption for one second is 20J, hence each neuron will consume 200pJ. In case of fast brain activities, each neuron spikes at an average frequency of 20Hz, corresponding to the average beta wave frequency (Priyanka, 2016). Based on the 20Hz frequency value, we can easily deduce that the energy per spike is around 10pJ/spike. This simple calculation corresponds to the estimation of energy per spike for a biological neuron from human cortex reported from (Poon and Zhou, 2011) and (Lennie, 2003).

The second method is based on our previous results concerning the excitability of the neuronal cell. We have investigated in detail the generation of one spike and its corresponding ionic currents (I_{Na} and I_K) in HH model and Wei model. Based on these ionic currents, we can estimate the power and the energy consumption per spike, which is presented in the following section.

2.3.3.2 Power consumption per spike based on ionic currents

According to the equations presented in the **Table 2.2**, we define sodium power (P_{Na}) and potassium power (P_K) for HH model and Wei model. The power consumption for each models are based on the ionic currents (I_{Na} and I_K), the membrane potential (V_m) and Nernst potentials (E_{Na} and E_K). Obviously, the overall dissipated power (P_d), is obtained by the addition of P_{Na} and P_K.

© 2018 Tous droits réservés.

$P_{Wei,HH}\ (nW.cm^{-2})$
$P_{Na} = I_{Na}(V_m - E_{Na})$
$P_K = I_K(V_m - E_K)$
$P_d = I_{Na}(V - E_{Na}) + I_K(V - E_K)$

Table 2.2 Power consumption for HH and Wei model.

The Nernst potentials are constant in the HH model, while the Nernst potentials in the Wei model vary as function of the dynamic of the ionic concentrations (annex). The resulting power of HH and Wei models are illustrated in **Figure 2.19**. We observe similar shapes for P_K. For both models, the P_d occurs during 2ms. However the shape of P_{Na} differs between the two models having an impact on P_d. In addition, the powers amplitudes in HH model are much higher than in Wei model.

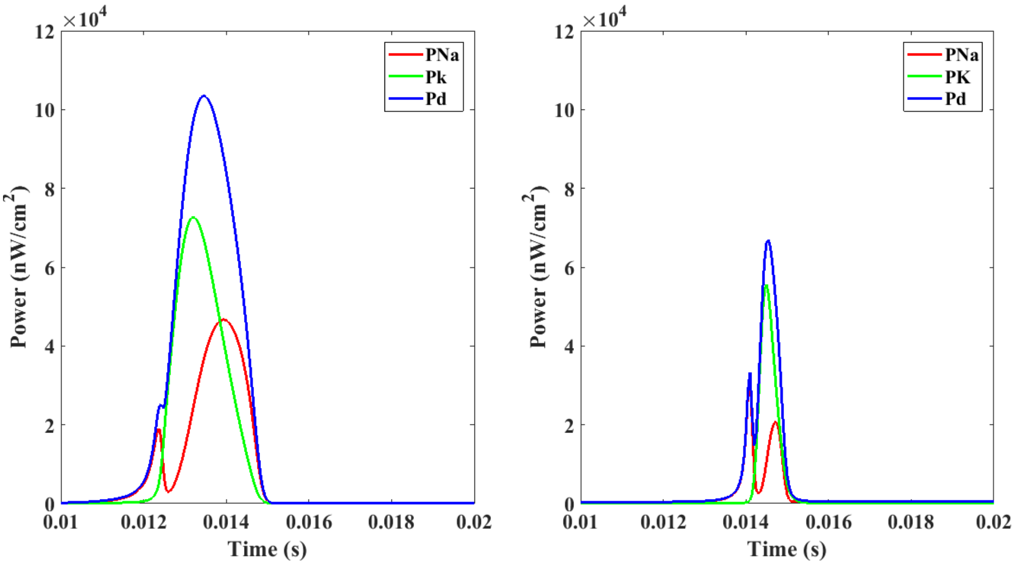

Figure 2.19 Comparison of power consumption in HH model and Wei model. In both models $\boldsymbol{P_{Na}}$(red), $\boldsymbol{P_K}$(green) and $\boldsymbol{P_d}$(blue) are in nW/cm^2. **Left:** Power consumption in HH model for Iex = 7µA/cm^2 during Ts = 14ms (same as Ts = 7ms). **Right:** Power consumption in Wei model for Iex = 7µA/cm^2 during Ts = 7ms.

We performed a trapeze type integration of P_{Na} and P_K and multiplied these results to the surface of the neuronal membrane to determine the energy consumption per spike. To define the surface of the neuronal membrane, we consider the shape of the cell body to be spherical with a 20µm diameter (Bear et al, 2007). We obtain a neuronal surface of 10^{-6} cm^2. Hence, the energy consumption per spike for HH model is 20 fJ/spike and 3 fJ/spike for Wei model. The energy per spike obtained with the Wei model is less than the value obtained with HH model due to the lower amplitude of each ionic power.

2.3.4 Conclusion on HH and Wei models

HH model and Wei model reproduce the excitability of the neuronal membrane. For both models, we have determined a specific excitatory current for the generation of

© 2018 Tous droits réservés.

only one spike. Additionally, we have investigated the influence of the number of injected charges on the generation of one spike in the Wei model. We have performed the analyses of power and energy consumption of both models, when the neuron spikes only once. As described previously both HH and Wei model are based on four nonlinear differential equations. These complex models are very useful to calibrate the electronic artificial neuron design but due to the high number of parameters, they lead to complex electrical circuits with considerable silicon surface (Yu and Cauwenberghs, 2010). Thus, a simpler and also biophysically meaningful model, the Morris-Lecar (ML) model was investigated. Next section will introduce the Morris Lecar model and some results from the simulation.

2.3.5 Morris-Lecar model

Catherine Morris and Harold Lecar have investigated the Barnacle muscle fibers. They proposed in 1981 a model with only two states variables known as the Morris-Lecar (ML) model (Morris and Lecar, 1981). This model describes the voltage oscillations in the Barnacle giant muscle fiber based on the membrane voltage V_m and the potassium gating variable n. As shown in Eq.2.8, ML model is a system of two non-linear differential equations associated with exponential functions.

$$
\begin{gathered}
C_m \frac{dV_m}{dt} = I_{ex} - G_{Ca} m_{ss}(V_m)(V_m - E_{Ca}) - G_k n(V_m - E_K) - G_L(V_m - E_L) \\
\frac{dn}{dt} = \lambda(V_m)(n_{ss}(V_m) - n) \\
m_{ss}(V_m) = \frac{1}{2}\left[1 + Tanh\left(\frac{V_m - V_1}{V_2}\right)\right] \\
n_{ss}(V_m) = \frac{1}{2}\left[1 + Tanh\left(\frac{V_m - V_3}{V_4}\right)\right] \\
\lambda(V_m) = \lambda_0 Cosh\left(\frac{V_m - V_3}{2V_4}\right)
\end{gathered}
\qquad \text{Eq.2.8}
$$

In these equations, C_m is the membrane capacitance, I_{ex} is the excitatory current, E_K, E_{Ca} and E_L are the ion equilibrium potentials, G_{Ca} G_K and G_L are the calcium (same as sodium in HH and Wei model), potassium and leak conductance. The steady-state potassium and sodium gating variables are respectively n_{ss} and m_{ss} while λ_0 is the reference frequency. Finally, V_1 to V_4 are fitting parameters that can serve for tuning the dynamic properties in order to represent different systems of interest.

We have simulated the Morris-Lecar (Waterloo, 2013) model also called "ML original" with an available Matlab code. The parameters of "ML original" model are extracted from Morris and Lecar, 1981 publication. First, the response of this model in time

© 2018 Tous droits réservés.

domain to different constant excitatory current (Iex) was investigated, as shown in **Figure 2.20**.

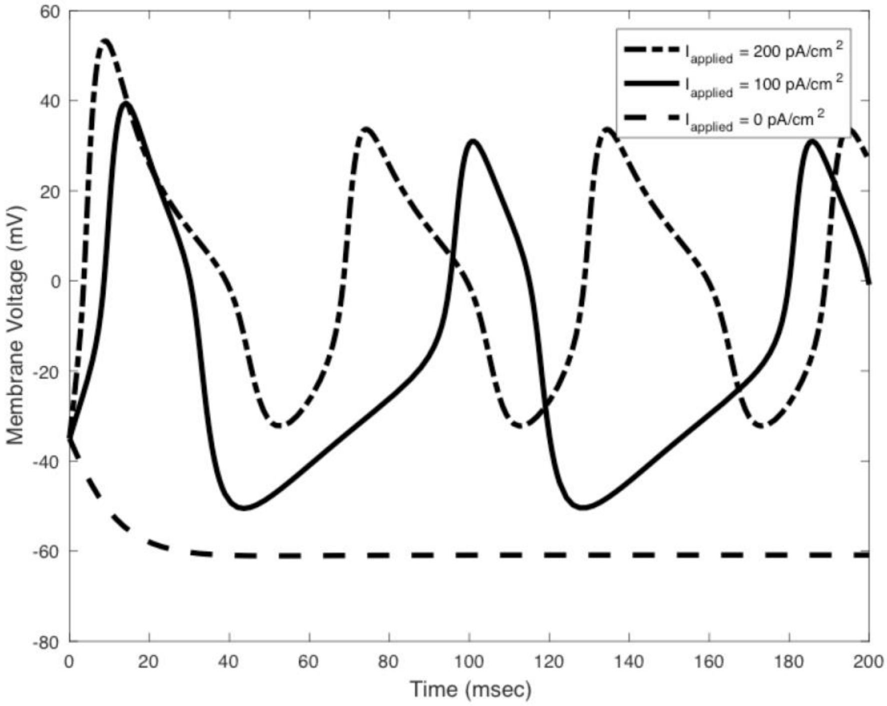

Figure 2.20 Response of ML model to different excitatory current. ML response to a continuous excitatory current: 0, 100 and 200pA/cm^2.

Additionally **Figure 2.21** shows the response of the ML model in frequency domain as a function of the excitatory current (Frequency-current or F-I curve). As illustrated by the F-I curve (**Figure 2.21**), without any excitatory current, the membrane voltage is in the resting state and an absence of spiking frequency is observed. As the excitatory current increases, the spiking frequency increases and reaches a maximum value of 16Hz. It can be noticed that the ML model spike frequency is around 8Hz for Iex = 90pA/cm^2. As we increase the excitatory current from 120pA/cm^2 to 200pA/cm^2, the spike frequency increases from 14Hz to 16Hz. It saturates around 16Hz for Iex between 150pA/cm^2 and 200pA/cm^2. The ML model does not spike for 250pA/cm^2 < Iex < 350pA/cm^2. This type of "Frequency versus current" curve correspond to class-1 neural excitability, in which action potentials can be generated with arbitrarily low frequency that increases in accordance with the excitatory current (Izhikevich, 2007).

© 2018 Tous droits réservés.

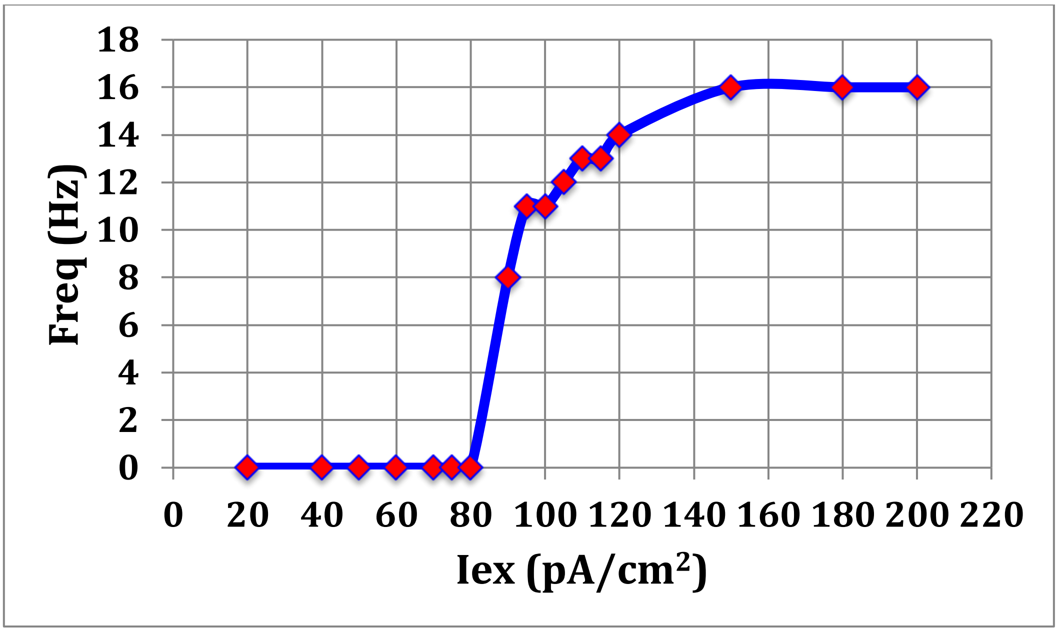

Figure 2.17 The F-I curve of ML model.

We can conclude that ML model validates the excitability behavior of the neuronal membrane and also reproduces the spiking activity of a neuronal cell. Hence, this model can be used as a guideline since it is simple enough to be reproduced by a conventional electrical circuit. ML model will be more investigated in chapter 3. The analogy between the ML equations and the circuit proposed for the artificial neuron will be explained.

© 2018 Tous droits réservés.

Thèse de Sara Hedayat, Université de Lille, 2018

2.4 Conclusion

In this part, the various specialized regions of a neuron cell were presented. The main region responsible in the generation of action potential, the neuronal membrane was described. The dynamics of ionic channels present in the neuronal membrane can indeed explain the generation of spikes. Ionic channel mechanisms can be described with mathematical equations known as neuronal model. An overview of various neuronal models was presented in this chapter. In order to understand the complex behavior of the neuronal membrane, three of these biophysical models HH, Wei and Morris-Lecar were investigated. Each of these neuronal models was studied through simulation by Matlab software (and Monte Carlo simulation for HH model). Based on results presented in this chapter, the excitability mechanisms of the neuron were specified. A precise modulation of the generation of spikes as a function of the charge density was performed. This allows us to estimate the power and energy efficiency per spike for HH and Wei model.

© 2018 Tous droits réservés.

lilliad.univ-lille.fr

2.5 Annex

Hodgkin Huxley model

Ionic current:

The ionic current is composed of sodium current (I_{Na}), potassium current (I_K) and leakage current (I_l). Their expression are presented as follow

$$I_{Na} = g_{Na}(V_m - E_{Na})$$
$$I_K = g_K(V_m - E_K)$$
$$I_l = g_l(V_m - E_l)$$

Constant parameters:

The following values are taken from the publication of Hodgkin and Huxley in 1952. They are implemented in HH code and simulated with Matlab software.

C_M (µ$F.cm^{-2}$)	*1.0*
E_{Na} (mV)	*+55*
E_K (mV)	*-72*
E_l (mV)	*-49.4*
$\bar{g}_{Na}$ ($m.mho.cm^{-2}$)	*120*
$\bar{g}_K$ ($m.mho.cm^{-2}$)	*36*
g_l ($m.mho.cm^{-2}$)	*0.3*

Sodium conductance:

The sodium conductance depends on gating variables m and h.

$$g_{Na} = \bar{g}_{Na}m^3h$$
$$\frac{dm}{dt} = \alpha_m(1-m) - \beta_m m$$
$$\frac{dh}{dt} = \alpha_h(1-h) - \beta_h h$$

Gating variables and transition rate constants:

Gating variable n is a dimensionless quantity, comprise between 0 and 1, which corresponds to potassium channel activation. The constant α_n determines the rate at which a gating channel switch from closed state to open state, while β_n is a rate at which it switches from an open state to a closed one. The transition rate constants α_n and $\beta_n$are related to V$_m$ through rather complex exponential functions.

© 2018 Tous droits réservés.

2.5 Annex

$$\frac{dn}{dt} = \alpha_n(1-n) - \beta_n n$$

$$\alpha_n(V_m) = \frac{0.01(V_m - 10)}{1 - \exp\left[\frac{-(V_m - 10)}{10}\right]}$$

$$\beta_n(V_m) = 0.125\exp(-\frac{V_m}{10})$$

Gating variable n and transition rate constants α_n and β_n

Gating variable m is a dimensionless quantity between 0 and 1, which correspond to sodium channel activation. α_m and β_m represent the transition rate constants.

$$\frac{dm}{dt} = \alpha_m(1-m) - \beta_m m$$

$$\alpha_m(V_m) = \frac{0.1(V_m - 25)}{\exp\left[\frac{-(V_m - 25)}{10}\right] - 1}$$

$$\beta_m(V_m) = 4\exp(-\frac{V_m}{18})$$

Gating variable m and transition rate constants α_m and β_m

Gating variable h is a dimensionless quantity between 0 and 1, which correspond to sodium channel inactivation. α_h and β_h represent the transition rate constants.

$$\frac{dh}{dt} = \alpha_h(1-h) - \beta_h h$$

$$\alpha_h(V_m) = 0.07\exp(-\frac{V_m}{20})$$

$$\beta_h(V_m) = \frac{1}{1 + \exp\left[\frac{-(V_m - 30)}{10}\right]}$$

Gating variable h and transition rate constants α_h and β_h

Wei model

Potassium, sodium and chloride concentrations:

The concentration of each ion type is continuously updated by integrating the relevant ion currents and fluxes. As an example, the rate of change of the number of intracellular K^+ ions, $\frac{dNK_i^+}{dt}$, is a function of IK and Ipump, as well as cotransport currents Inkcc1

© 2018 Tous droits réservés.

and Ikcc2.

$$\frac{dNK_i^+}{dt} = \frac{1}{\tau}\left(-\gamma I_K + 2I_{pump} - I_{kcc2} - I_{nkcc1}\right)\nu_i$$

$$\frac{dNK_0^+}{dt} = \frac{1}{\tau}\left(\gamma\beta I_K - 2\beta I_{pump} - I_{diff} - I_{glia} - 2I_{gliapump} + \beta I_{kcc2} + \beta I_{nkcc1}\right)\nu_0$$

Potassium concentrations in Wei model

The intracellular Na$^+$ ion number dynamics, $\frac{dNNa_i^+}{dt}$, is modeled based on the membrane Na$^+$ current (INa), Ipump, and Inkcc1.

$$\frac{dNNa_i^+}{dt} = \frac{1}{\tau}\left(-\gamma I_{Na} - 3I_{pump} - I_{nkcc1}\right)\nu_i$$

$$\frac{dNNa_0^+}{dt} = \frac{1}{\tau}\left(-\gamma\beta I_{Na} + 3\beta I_{pump} + \beta I_{nkcc1}\right)\nu_0$$

Sodium concentrations in Wei model

The dynamics of the number of intracellular Cl$^-$, $\frac{dNCl_i^-}{dt}$, is a function of ICl, Inkcc1, and Ikcc2.

$$\frac{dNCl_i^-}{dt} = \frac{1}{\tau}(\gamma I_{ClL} - I_{kcc2} - 2I_{nkcc1})\nu_i$$

$$\frac{dNCl_0^-}{dt} = \frac{1}{\tau}(-\gamma\beta I_{ClL} + \beta I_{kcc2} + 2\beta I_{nkcc1})\nu_0$$

Chloride concentrations in Wei model

In these equations τ = 1000 is used to convert second to millisecond. νi and νo are the intracellular and extracellular volumes, respectively. β = νi/νo is the ratio of intra-/extracellular volume.

Nernst potential:

The reversal potentials of Na$^+$ (E_{Na}), K$^+$ (E_K), and Cl$^-$ (E_{Cl}) are given by Nernst equations:

$$E_{Na} = 26.64\ln\left(\frac{[Na^+]_0}{[Na^+]_i}\right)$$

$$E_K = 26.64\ln\left(\frac{[K^+]_0}{[K^+]_i}\right)$$

$$E_{Cl} = 26.64\ln\left(\frac{[Cl^-]_i}{[Cl^-]_0}\right)$$

where [.]i and [.]o represent concentrations inside and outside the cell, respectively.

© 2018 Tous droits réservés.

2.5 Annex

Constant parameters:

The units and description of all parameters used in Wei model are summarized in the following table.

Parameters	Units	Description
C	$1\mu F.cm^{-2}$	Membrane capacitance
G_{Na}	$30mS.cm^{-2}$	Maximal conductance of sodium current
G_K	$25mS.cm^{-2}$	Maximal conductance of potassium current
G_{NaL}	$0.0247mS.cm^{-2}$	Conductance of leak sodium current
G_{KL}	$0.05mS.cm^{-2}$	Conductance of leak potassium current
G_{ClL}	$0.1mS.cm^{-2}$	Conductance of leak chloride current
β_0	7	Ratio of the initial intra-/extracellular volume
ρ_{max}	$0.8\ mM/s$	Maximal Na/K pump rate
$G_{glia,max}$	$5\ mM/s$	Maximal glia uptake strength of potassium
$\varepsilon_{k,max}$	$0.25s^{-1}$	Maximal potassium diffusion rate
$[K^+]_{bath}$	$3.5g.mol^{-1}$	Normal bath potassium concentration
ε_0	$0.17s^{-1}$	Oxygen diffusion rate
α	$5.3g.mol^{-1}$	Conversion factor
$[0_2]_{bath}$	$32mg.L^{-1}$	Normal bath oxygen concentration
U_{kcc2}	$0.3mM/s$	Maximal KCC2 cotransporter strength
U_{nkcc1}	$0.1mM/s$	Maximal NKCC1 cotransporter strength

© 2018 Tous droits réservés.

2.6 References

(Andres-Barquin, 2001) Andres-Barquin, P. J. (2001). Ramón y Cajal: a century after the publication of his masterpiece. *Endeavour*, *25*(1), 13–17. https://doi.org/10.1016/S0160-9327(00)01334-X

(Bear et al, 2007) Bear Mark.F et al, Neurosciences, A la découverte du cerveau, 2007, 3e edition, Edition Pradel, ISBN :978-2-913996-66-3.

(Caldwell, 2010) Caldwell, J. H. (2010). Action Potential Initiation and Conduction in Axons. In *Encyclopedia of Neuroscience* (pp. 23–29). https://doi.org/10.1016/B978-008045046-9.01642-9.

(Drubach, 2000) Drubach, Daniel. The Brain Explained. New Jersey: Prentice-Hall, 2000.

(Hodgkin and Huxley, 1952) Hodgkin AL, Huxley AF, A quantitative description of membrane current and its application to conduction and excitation in nerve,1952, J Physiol 117:500 –544.

(Izhikevich, 2004) Izhikevich, E. M, Which model to use for cortical spiking neurons?, 2004, IEEE Trans. Neural Netw. 15, 1063–1070. doi: 10.1109/TNN.2004.832719.

(Izhikevich, 2007) Izhikevich, E. M, Dynamical Systems in Neuroscience: The Geometry of Excitability and Bursting, 2007, Cambridge, MA: MIT Press.ISBN 978-0-262-09043-8.

(Lodish, 2000) Lodish H, Berk A, Zipursky SL, et al. Molecular Cell Biology, 2000, 4th edition. New York: W. H. Freeman, Section 21.1, Overview of Neuron Structure and Function. Available from: https://www.ncbi.nlm.nih.gov/books/NBK21535.

(Lennie, 2003) Lennie P, The cost of cortical computation, 2003, Curr Biol 13:493–497.

(Morris and Lecar, 1981) Morris, C., and Lecar, H. (1981). Voltage oscillations in the barnacle giant muscle fiber. Biophys. J. 35, 193–213.

(Purves, 2004) Purves Dale, George J. Augustine, David Fitzpatrick, William C. Hall, Anthony-Samuel LaMantia, James O. McNamara, S. Mark Williams, Neuroscience, 2004 third edition, Sinauer Associate , ISBN: 0-87893-725-0.

© 2018 Tous droits réservés.

2.6 References

(Poon and Zhou, 2011) Poon C-S, Zhou K. Neuromorphic Silicon Neurons and Large-Scale Neural Networks: Challenges and Opportunities. *Frontiers in Neuroscience*. 2011;5:108. doi:10.3389/fnins.2011.00108.

(Priyanka, 2016) Priyanka A.Abhang and Suresh C.Mehrotra, in introduction to EEG and Speech based emotion recognition (https://www.sciencedirect.com/topics/medicine-and-dentistry/beta-wave), 2016.

(Rigden, 1996) Rigden, John S. 1996. *Macmillan encyclopedia of physics*. New York: Simon & Schuster Macmillan.

(Schwiening, 2012) Schwiening Christof J., A brief historical perspective: Hodgkin and Huxley, 2012, J.Physiol, May 2012; DOI: 10.1113.

(Siciliano, 2012) Siciliano, R. (2012). The Hodgkin-Huxley Model Its Extensions, Analysis and Numerics. Retrieved from http://www.math.mcgill.ca/gantumur/docs/reps/RyanSicilianoHH.pdf.

(Vasallo et al, 2017) G.Vasallo, F.Galán-Prado, J.Mateos, T.González, S.Hedayat, V.Hoel and A.Cappy. "Monte Carlo model for action potentials in bioinspired devices", Journal of Computational Electronics, Volume 16, Issue 2, pp 419–430, June 2017.

(Wei et al, 2014) Wei Y, Ullah G, Ingram J, Schiff SJ, Oxygen and seizure dynamics: II. Computational modeling, 2014, J Neurophysiol 112:213–223.

(Waterloo, 2013) https://www.math.uwaterloo.ca/~bingalls/MMSB/Code/matlab/ Morris_Lecar.m.

(Yu and Cauwenberghs, 2010) Yu, T., and Cauwenberghs, G. (2010). Analog VLSI biophysical neurons and synapses with programmable membrane channel kinetics. IEEE Trans. Biomed.Circuits Syst. 4, 139–148. doi: 10.1109/TBCAS.2010.2048566.

© 2018 Tous droits réservés.

Thèse de Sara Hedayat, Université de Lille, 2018

Chapter 3.

Analog artificial neuron

© 2018 Tous droits réservés.

lilliad.univ-lille.fr

© 2018 Tous droits réservés.

In order to design an original and innovative analog artificial neuron, it was necessary to verify the existing solutions at the beginning of this work. To fulfill this task, a state-of-the-art of stand-alone artificial neurons in terms of power, energy dissipation, and occupied area was provided and presented in the first part of this chapter.

In the second part, the analogy between the artificial neuron and the Morris-Lecar model will be demonstrated. This artificial neuron can emulate with a good accuracy the behavior of living neuron, which we will be referring as "biomimetic neuron".
It can also, instead of mimicking the biology, provide higher frequency spike rates to target large scale bio-inspired networks for the information processing applications. This version of the artificial neuron is designated "fast neuron". The biomimetic neuron and fast neuron as well as their design parameters will be presented in the third and the fourth part of this chapter.

To design an artificial neural network, it is necessary to include synapses between neurons, as in biology. Following this idea, we have connected these different artificial neurons with simple synapses described in the third part of this chapter to investigate phenomena encountered in human brain such as the burst phenomena, which is presented in the fifth part.

All these bio-inspired circuits have been fabricated within two different chips designated as WetWire and GreyMatter in the TSMC 65nm CMOS technology. We performed the characterization of these chips at IEMN laboratory and we will present corresponding results in the fifth and sixth part of this chapter. We will conclude on the performances of these proposed neuro-inspired circuits and give some perspectives for the following chips.

3.1 State of the art of artificial neuron

In the scope of neuromorphic, computing, different ways are used to fulfill this task such as hardware neural networks. Hardware devices, designed to realize artificial neural network (ANN) architectures and associated learning algorithms especially taking advantage of the inherent parallelism in the neural processing are referred as hardware neural networks (HNN) (Misra & Saha, 2010).
The choice of the technology is driven by the application and the aimed performances. It can range from silicon neuron (Indiveri et al., 2011) to all memristor neuron and synapse (Pantazi, Woźniak, Tuma, & Eleftheriou, 2016) (La Barbera et al., 2015) and even spintronic oscillator neuron (Torrejon et al., 2017). These components often

© 2018 Tous droits réservés.

present several strengths as well as several constraints such as complicated circuits, immature technology and reliability issues.
These basic blocks contribute to the hardware realization of artificial neural network (HNN). Therefore, artificial neuron represents one of the main building blocks for implementing neuromorphic systems (Indiveri et al, 2011).

In our case, an artificial neuron is defined as a hardware implementation of the biological neuron. We focus on silicon artificial neuron based on complementary metal oxide semiconductor abbreviated as CMOS technology. This technology is predominant in micro- and nanoelectronics circuits as microprocessors, microcontrollers and other digital logic circuits. CMOS technology is also widely used for analog circuits such as image sensors, data convertors and so on.

Beyond these industrialized applications, CMOS technology allows a high-density integration of logic functions on a chip and became the most used technology to be implemented in very large-scale integration (VLSI) chips. The use of standard industrial technology was an important point to reduce the fabrication time of artificial neurons using foundries such as Taiwan Semiconductor Manufacturing Company (TSMC) and to scale up neural networks with the integration of more than 1000 neurons in a hardware neuronal network.

Moreover, it is possible to envisage a hybrid system where a CMOS neuron is connected to memristive synapses as illustrated in **Figure 3.1** (Yang et al., 2013).

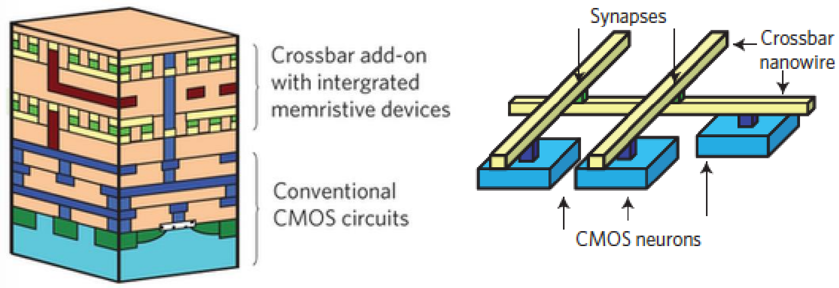

Figure 3.1 Hybrid CMOS memristor circuit. Memristive devices correspond to artificial synapses and CMOS circuits correspond to artificial neurons (Yang et al, 2013).

Analog spiking hardware approach is used to develop general purpose ultra-low power and large-scale neural systems. Different laboratories have worked on stand-alone analog neuron. The state-of-the-art analog artificial neurons based on their

© 2018 Tous droits réservés.

performances in terms of power, energy consumption and area are presented in **Table 3.1**.

References	**Neuron type**	**CMOS node**	**Core Area (μm^2)**	**Spiking frequency (Hz)**	**Power**	**Energy (pJ/Spike)**
Indiveri et al., 2006	LIF	0.35 µm	2573	200	-	900
Wijekoon and Dudek, 2008	LIF	0.35 µm	2800	10^6	8-40 µW	8.5-9
Basu and Hasler, 2010	Saddle	0.35 µm	2740	100	1.74 nW	17.4
Joubert et al., 2012	LIF	65 nm	538	$1.9\ 10^6$	78 µW	41
Cruz-Albrecht et al., 2012	LIF	90 nm	442	100	40 pW	0.4

Table 3.1 State-of-the-art performance of reported stand-alone artificial neurons.

As shown in **Table 3.1**, the common neuron type is Leaky Integrated Fire (LIF - presented in the chapter 2), which represents one of the simplest and most widely used for such implementations. Based on results reported in **Table 3.1**, we can conclude that the most energy efficient stand-alone neuron was proposed by Cruz-Albrecht in 2012. It consumes 40pW and 0.4pJ/spike with a core area of 442 μm^2.

These artificial neurons have been investigated. Based on their performances an ultra low power artificial neuron has been proposed, with several versions and will be presented in the next section.

3.2 Design of artificial neuron

There are specific applications such as streaming video compression, which demand high volume adaptive real-time processing and learning of large datasets in reasonable time and necessitate the use of energy-efficient HNN (Misra & Saha, 2010). To meet different applications, several versions of the artificial neuron have been designed in this work. The biomimetic neuron mimics the behavior of living neuron by reproducing biological action potential and time constants. The fast neuron is designed to generate

© 2018 Tous droits réservés.

higher spiking frequencies with minimal core area. These versions of the artificial neuron and their corresponding circuits will be explained in the following sections.

The artificial neuron is based on ML model, which is constituted of two non-linear differential equations associated with exponential functions. These equations can be represented by expressions based on current node summation, as per Kirchhoff's Current Law (KCL). These equations, Eq.3.1 to Eq.3.5 have been investigated in chapter 2.

$$C_m \frac{dV_m}{dt} = I_{ex} - G_{Ca} m_{ss}(V_m)(V_m - E_{Ca}) - G_k n(V_m - E_K) - G_L(V_m - E_L) \quad \text{Eq.3.1}$$

$$\frac{dn}{dt} = \lambda(V_m)(n_{ss}(V_m) - n) \quad \text{Eq.3.2}$$

$$m_{ss}(V_m) = \frac{1}{2}\left[1 + Tanh\left(\frac{V_m - V_1}{V_2}\right)\right] \quad \text{Eq.3.3}$$

$$n_{ss}(V_m) = \frac{1}{2}\left[1 + Tanh\left(\frac{V_m - V_3}{V_4}\right)\right] \quad \text{Eq.3.4}$$

$$\lambda(V_m) = \lambda_0 Cosh\left(\frac{V_m - V_3}{2V_4}\right) \quad \text{Eq.3.5}$$

The link between the HH model and electronic circuits is not a trivial matter due to the use of four non-linear differential equations. On the contrary, the ML model is much more attractive for this purpose containing only two state variables: the membrane voltage V_m and the potassium gating variable *n* (Eq.3.1 to Eq.3.5).

Based on the analyzes presented in chapter 2, we have concluded that the main channels responsible for generating the spike are the sodium and potassium channels. The dynamics of each ionic channel (Na^+ and K^+), can be reproduced by a single transistor (see **Figure 3.2**) biased in sub-threshold regime (Farquhar and Hasler, 2005) (Hynna and Boahen, 2007).

© 2018 Tous droits réservés.

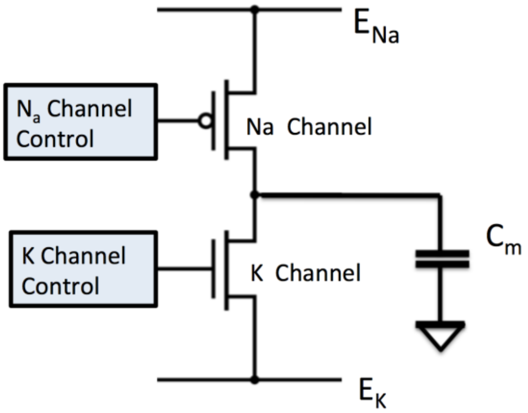

Figure 3.2 General schematic of artificial membrane circuit.

In this approach, we replace the calcium channel defined in the original Morris-Lecar model, by the sodium channel in our artificial neuron represented in **Figure 3.3**. The membrane capacitance (C_m) is charged through a PMOS transistor modeling the sodium channel (MP_{Na}) and discharged through an NMOS transistor modeling the potassium channel (MN_K) and the leakage conductance (G_L). The leak conductance is in fact an NMOS transistor, which enables us to adjust the artificial neuron stability. We will discuss this point in the next section.

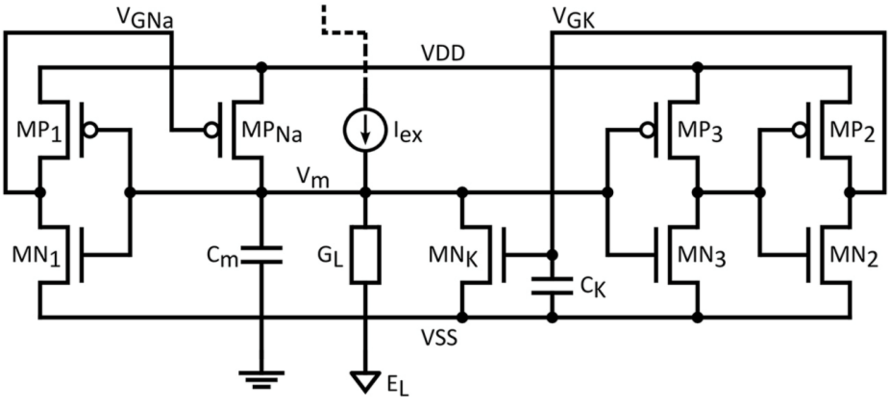

Figure 3.3 Artificial neuron circuit based on the ML model.

This circuit reproduces the generation of one action potential (V_m) through the membrane capacitance and the two feedback loops. The membrane voltage (V_m) is defined as a voltage across the membrane capacitance and it is also the node corresponding to the summing point of the excitatory current (I_{ex}), leakage current, positive and negative feedback loop.

A positive feedback loop (through MP_{Na} and MP_1/MN_1) implements a pull-up network for the creation of V_m. The negative feedback loop, which implements a pull-down network,

© 2018 Tous droits réservés.

is defined through MN_K and the two cascaded inverters MP_2/MN_2 and MP_3/MN_3. The time constant of the negative-feedback loop is set by capacitance C_K.

3.2.1 Excitatory and inhibitory synapses

The excitatory current I_{ex} is assumed to be provided by a synaptic circuit which in the most rudimentary form can be implemented by a single transistor current source. Therefor for the artificial neuron the synaptic circuit is a PMOS transistor. In fact, a PMOS transistor can model excitatory synapses through additional sodium channels, while conversely, inhibitory synapses would be represented by additional potassium channels and NMOS transistors (see **Figure 3.4**). As widely supported by many works (Arthur and Boahen, 2006) in order to introduce plasticity, the excitatory and inhibitory post synaptic currents can be controlled by interposing “weight” transistors (V_{Wexc} is the weight for excitatory synapse and V_{Winh} is the weight for inhibitory synapse).

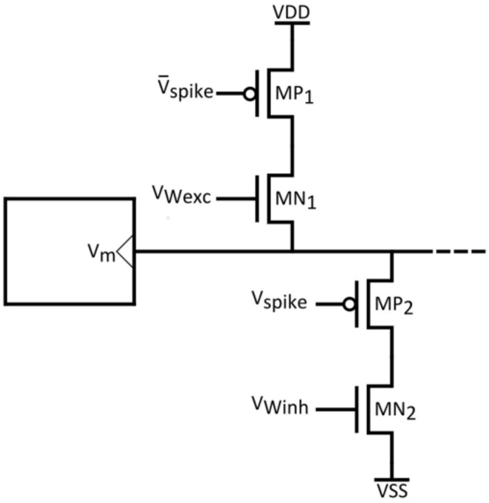

Figure 3.4 Indicative synaptic circuits.

In conclusion, the excitation of the artificial neuron is produced by the PMOS transistor, which is considered as the input of the artificial neuron. The membrane voltage of the artificial neuron (V_m) is connected to a buffer which is considered as the output of the artificial neuron. This part will be more developed in the "fabrication" section.

In the following paragraphs the artificial neuron circuit will be analyzed. This circuit analysis is divided in three parts: the drain current model, the static properties of the inverters in subthreshold operation and finally the circuit response equation.

© 2018 Tous droits réservés.

3.2.2 Drain current model in the sub-threshold regime

All the transistors used in the artificial neuron are assumed to operate in the deep sub-threshold regime, with a supply voltage lower than (or equal to) 200mV. Therefore, the drain current will have an exponential relation with gate-to-source voltage V_{gs}. Hence, the following expression is suited to model the drain current:

$$I_{ds} = G_0 \exp\left(\frac{V_{gs}}{\eta V_t}\right) V_{ds} \qquad \text{Eq.3.6}$$

where G₀ represents the device conductance with G_{n0} for NMOS and G_{p0} for PMOS; V_{ds} is the drain-to-source voltages, η is the subthreshold slope factor and V_t is the thermal voltage. The NMOS and PMOS ideality factors are assumed to have the same value.

As it will be proved, the use of such a simple model provides a comfortable medium for demonstrating the correlation between the circuit response and the ML model equations sufficiently. In addition to that, it allows a straightforward circuit analysis that is essential for the implementation effort in the CMOS technology.

3.2.3 Static properties of inverters in sub-threshold

The inverters play a central role in the artificial neuron performances. In fact, they are the elementary circuits used to reproduce the hyperbolic tangent function (*Tanh*) present in the Morris-Lecar model (see Eq.3.3 and Eq.3.4).

$$m_{ss}(V_m) = \frac{1}{2}\left[1 + Tanh\left(\frac{V_m - V_1}{V_2}\right)\right] \qquad \text{Eq.3.3}$$

$$n_{ss}(V_m) = \frac{1}{2}\left[1 + Tanh\left(\frac{V_m - V_3}{V_4}\right)\right] \qquad \text{Eq.3.4}$$

A CMOS inverter operating in the sub-threshold regime is illustrated in **Figure 3.5**.

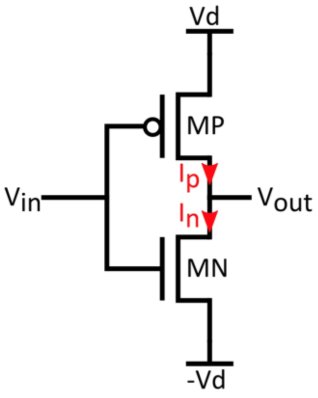

Figure 3.5 Inverter biasing conditions used in the analysis.

© 2018 Tous droits réservés.

As shown in **Figure 3.5** the input and output voltages are V_{in} and V_{out}. The supply voltages are presented by V_d and $-V_d$. By applying the Kirchhoff's Current Law for the output node of this inverter (see **Figure 3.5**) and expressing currents (I_p and I_n) as in Eq.3.6, the output voltage can be expressed as following:

$$V_{out} = -V_d . Tanh\left[\frac{V_{in}}{\eta V_t} + \frac{1}{2}\ln\left(\frac{G_{n0}}{G_{p0}}\right)\right] = -V_d . Tanh\left[\frac{V_{in} - V_{isv}}{\eta V_t}\right] = -V_d . Tanh\left[\frac{V_q}{\eta V_t}\right] \qquad \text{Eq.3.7}$$

The *Tanh* in Eq.3.7 can be simplified by using the following expressions where the ratio of conductances (G_{n0}/G_{p0}) appears:

$$V_{isv} \cong V_{in}|_{(V_{out}=0)} = -\frac{\eta V_t}{2} ln\left(\frac{G_{n0}}{G_{p0}}\right) \qquad \text{Eq.3.8}$$

As shown in Eq.3.8, V_{isv} represents the input voltage V_{in} when $V_{out} = 0$. It can be either positive or negative depending on the conductance ratio.

In order to simplify Eq.3.7, we also use the parameter V_q defined as follows:

$$V_q = V_{in} - V_{isv} \qquad \text{Eq.3.9}$$

The output voltage described in Eq.3.7, shows two important properties of the proposed artificial neuron. Primarily, the switching voltages of inverters in this circuit are controlled by the conductance ratio. For example, with a ratio of 10 between the NMOS and PMOS conductance, the switching threshold can be shifted around 50mV. Hence, we can tune the required voltage shifts V_1 and V_3 in Eq.3.3 and Eq.3.4. Secondarily, in order to match the behavior of artificial neuron, the presence of voltage gain is necessary. As it has been shown by (Mead, 1989), the high value of the sub-threshold slope of MOS transistors (larger than 60 mV/dec) yields a much lower current-voltage slope than the one in biology. Hence, to mimic the neuron dynamic and reach the correct circuit operation, it is necessary to benefit of the gain brings by the presence of inverters.

In Eq.3.7, the maximum voltage gain *Av* will be obtained for $V_{out} = 0$. This can be expressed as:

$$A_v = \left.\frac{dV_{out}}{dV_{in}}\right|_{V_{in}=V_{isv}} = -\frac{V_d}{\eta V_t} \qquad \text{Eq.3.10}$$

© 2018 Tous droits réservés.

According to Eq.3.10, the magnitude of A_v can be larger than one for $V_d > \eta V_t$. For an ηVt about 35mV to 40mV, a significant voltage gain can be provided when V_d > 70–80mV. It is worth mentioning that this supply voltage value is close to the Nernst potentials encountered in biological cells. This last observation reveals that the artificial neuron can be implemented to operate under extremely low supply bias.

3.2.4 The circuit response analysis

In this part, we will demonstrate the analogy between the Morris-Lecar equations and the artificial neuron response. The artificial neuron and the two summing nodes V_{GK} and V_m are presented in **Figure 3.6**.

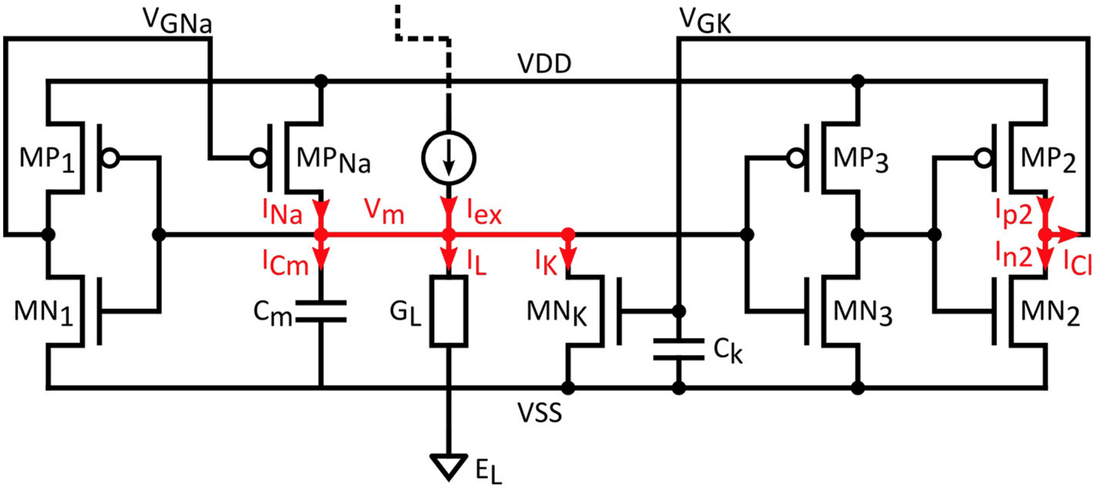

Figure 3.6 Artificial neuron circuit analyses.

For the sake of simplicity, we consider a symmetrical supply voltage and neglect the transistor capacitances. The application of KCL on V_m and V_{GK} nodes allows us to obtain the following equations:

$$I_{Cm} = I_{Na} - I_K + I_{ex} - I_L \qquad \text{Eq.3.11}$$

$$I_{Ck} = I_{p2} - I_{n2} \qquad \text{Eq.3.12}$$

Where I_{Cm} and I_{Ck} are respectively the current through the membrane and the potassium capacitances. I_{Cm} is defined by the drain current of MPNa (I_{Na}), the drain current of MNK (I_K), the excitatory current (I_{ex}) and the leakage current (I_L). In the same way, I_{Ck} results from the drain current of MP_2 (I_{p2}) and the drain current of MN_2 (I_{n2}). In the above equations, we replace all the drain currents by the Eq.3.6 and we obtain the following equations:

© 2018 Tous droits réservés.

$$\begin{aligned} C_m \frac{dV_m}{dt} &= G_{Na} \exp\left(\frac{V_d - V_{GNa}}{\eta V_t}\right)(V_d - V_m) \\ &\quad - G_K \exp\left(\frac{V_{GK} + V_d}{\eta V_t}\right)(V_m + V_d) + I_{ex} - I_L(V_m) \end{aligned} \qquad \text{Eq.3.13}$$

$$\begin{aligned} C_k \frac{dV_{GK}}{dt} &= G_{p2} exp\left(\frac{V_d - V_{out3}}{\eta V_t}\right)(V_d - V_{GK}) \\ &\quad - G_{n2} \exp\left(\frac{V_{out3} + V_d}{\eta V_t}\right)(\mathrm{V_d} + \mathrm{V_{GK}}) \end{aligned} \qquad \text{Eq.3.14}$$

where V_{GNa} and V_{GK} correspond to the gate voltages of $\mathrm{MP_{Na}}$ and $\mathrm{MN_K}$. V_{GNa} is the output of the first inverter (MP1/MN1) and V_{out3} is the output of the third inverter (MP3/MN3). An input/output relation such as Eq.3.7 relates both V_{GNa} and V_{out3} to V_m. The Eq.3.14 could also be rewritten as follows:

$$\frac{dV_{GK}}{dt} = \lambda(V_m)\left[V_d Tanh\left(\frac{V_{q2}}{\eta V_t}\right) - V_{GK}\right] \qquad \text{Eq.3.15}$$

with the reference frequency $\lambda(V_m)$:

$$\lambda(V_m) = \frac{2. Cosh\left(\frac{V_{q2}}{\eta V_t}\right). exp\left(\frac{V_d}{\eta V_t}\right). \sqrt{G_{n2} G_{p2}}}{C_k} \qquad \text{Eq.3.16}$$

and parameter V_{q2}, based on Eq.3.9:

$$V_{q2} = V_{in2} - V_{isv2} = V_{out3} + \frac{\eta V_t}{2} ln\left(\frac{G_{n2}}{G_{p2}}\right) \qquad \text{Eq.3.17}$$

the differential equation for V_{GK} (Eq.3.15) is similar to that of the Morris-Lecar model. In particular, the time dynamics of V_{GK} are defined by the reference frequency $\lambda(V_m)$, which is related to the circuit parameters through Eq.3.16. The Eq.3.13 could be rewritten as the first differential equation of the Morris-Lecar model by introducing the parameters $m_{ss}(V_m)$ and n :

$$\begin{aligned} C_m \frac{dV_m}{dt} &= G_{Na} exp\left(\frac{2V_d}{\eta V_t}\right) m_{ss}(V_m)(V_d - V_m) \\ &\quad - G_K\, exp\left(\frac{2V_d}{\eta V_t}\right) n\,(V_m + V_d) + I_{ex} - I_L(V_m) \end{aligned} \qquad \text{Eq.3.18}$$

with the potassium gating variable, n:

$$n = exp\left(\frac{V_{GK} - V_d}{\eta V_t}\right) \qquad \text{Eq.3.19}$$

and,

© 2018 Tous droits réservés.

$$m_{ss}(V_m) = \exp\left(-\frac{V_{GNa}(V_m) + V_d}{\eta V_t}\right) \qquad \text{Eq.3.20}$$

V_{GNa} and V_{GK} are between $-V_d$ and $+V_d$ therefore $m_{ss}(V_m)$ and n are between 0 and 1. We observe a good correlation between the $m_{ss}(V_m)$ function of the artificial neuron and the *Tanh* function of the Morris-Lecar model.

As shown in Eq.3.19, n is simply related to V_{GK}. Assuming a small V_{GK}, the first order approximation of n would be:

$$n = exp\left(\frac{-V_d}{\eta V_t}\right)\exp\left(\frac{V_{GK}}{\eta V_t}\right) \approx \exp\left(-\frac{V_d}{\eta V_t}\right)\left(1 + \frac{V_{GK}}{\eta V_t}\right) \qquad \text{Eq.3.21}$$

Eq.3.21 demonstrates a linear relation between *n* and V_{GK}, which allows us to replace V_{GK} by *n* and rewrite Eq.3.15, as follows:

$$\frac{dn}{dt} = \lambda(V_m)[n_{ss}(V_m) - n] \qquad \text{Eq.3.22}$$

Hence, the equation of I_{CK} of the artificial neuron (Eq.3.14) matches the second differential equation (Eq.3.2) of the Morris-Lecar model. Based on Eq.3.13 and Eq.3.14 we can conclude that the dynamic behavior of the artificial neuron is described by the currents I_{Na}, I_K, I_{p2}, I_{n2} and the two time constants, which are associated with C_m and C_k.

The static power and the energy dissipation of the artificial neuron are described in the following paragraph and results will be presented in the next section. The static power is the product of the supply voltage ($+/-V_d$) by the leakage currents flowing through the inverters, the leak conductance (if present), the MP_{Na} and MP_K. The dynamic power is defined as the additional energy dissipation during spiking activity. It is related to the charge and discharge of the capacitances C_m and C_k.

In conclusion, we have demonstrated the analogy between the artificial neuron response and the Morris-Lecar model. Our approach is based on the use of a simple sub-threshold drain current model (Eq.3.6), the assumption of equal slope factors for PMOS and NMOS and a linearization step. This analytical model was used as a guideline for circuit design and was complemented by more rigorous circuit simulations presented in the next section.

© 2018 Tous droits réservés.

3.3 Design of biomimetic neuron

In order to design the biomimetic neuron and to define its design parameters, we had to choose the appropriate bioinspired neuronal model, which enables us to obtain a simple circuit with state-of-the-art performance (energy, power consumption and area). For example, Rasche and Douglas (Rasche & Douglas, 2000) describe an analog implementation of Hodgkin–Huxley model with 30 adjustable parameters, which required 4mm^2 area for a single neuron. This does not correspond to our objectives.

In chapter 2, we have investigated neuronal models with four state variables (Hodgkin Huxley model and Wei model) and two state variables (Morris-Lecar). In order to design a simple circuit, we have chosen the Morris-Lecar model to be the principal neuronal model and we developed the artificial neuron based on this neuronal model. Nevertheless, as we wanted to reproduce also the biological aspect of a living neuron, we choose the Wei model as my reference model.

The Wei model enables us to extract the main parameters involved in the human neuron spiking behavior. In the next sections, we will describe my methodology to use both models leading to the design of the biomimetic artificial neuron.

3.3.1 Design of biomimetic neuron: comparison with the Wei model

For some applications, the neuron dynamics should be compatible with the biological neuron one. The Wei model allows describing a wide range of neuronal activities. It unifies neuronal dynamics from usual spikes to seizures, enabling our understanding of the brain and defining what is essential in the control of pathological states (Wei et al., 2014). Two main criteria have been investigated, the shape of the spike and the excitatory response of the biological neuron.

First, parameters like spike width (SW), peak width (PW), threshold voltage (V_{th}), resting potential (V_{rest}), absolute refractory period (AR_p), spiking frequency (F) and peak-to-peak amplitude (V_{pp}) were extracted from the reference model proposed by Wei et al (Wei et al., 2014). The entire design of the biomimetic neuron relies on these parameters. Clearly, the biomimetic neuron must represent the same characteristic.

The second criterion is to understand the excitatory behavior seen in the biological neuron. This point was investigated in chapter 2 by varying the amplitude (I_{ex}) and the width (T_s) of the excitatory current. It was verified that the combination of these parameters resulted in a similar spiking frequency and enabled a precise modulation of the number of spikes.

Thus, we concluded that the excitability of the neuron depends on the amount of injected charge (Q) and this parameter was chosen to compare the Wei model with the artificial neuron. Since the Wei model parameters are defined by unit area, while those

© 2018 Tous droits réservés.

of the circuit are defined for a whole neuron, a normalization coefficient is needed to compare the different models. This coefficient is defined as follows:

$$\xi = {}^{I_{ex}}/_{C_m} \qquad \text{Eq.3.23}$$

where I_{ex} and C_m are respectively the excitatory current and the membrane capacitance. Using these two different criteria, we adjust the design of the artificial neuron, in order to obtain the same behavior of a biological neuron and designed the biomimetic neuron.

Two circuits have been designed for the biomimetic neuron, one with 6 transistors and another one with 8 transistors. The shape of sodium current (INa) and potassium current (IK) as well as their spike response are illustrated in **Figure 3.7** (biomimetic with 6 transistors) and **Figure 3.8** (biomimetic with 8 transistor). Both reproduce the spike shape observed in the biological neuron. However, a difference is observed in the output response while the same excitatory current (Iex = 1pA, Ts = 10ms, Q = 10fC and ξ = 80A/F) is used. The biomimetic neuron with 8 transistors (**see Figure 3.8**) produces three spikes while the biomimetic neuron with 6 transistors produces one spike (see **Figure 3.7**).

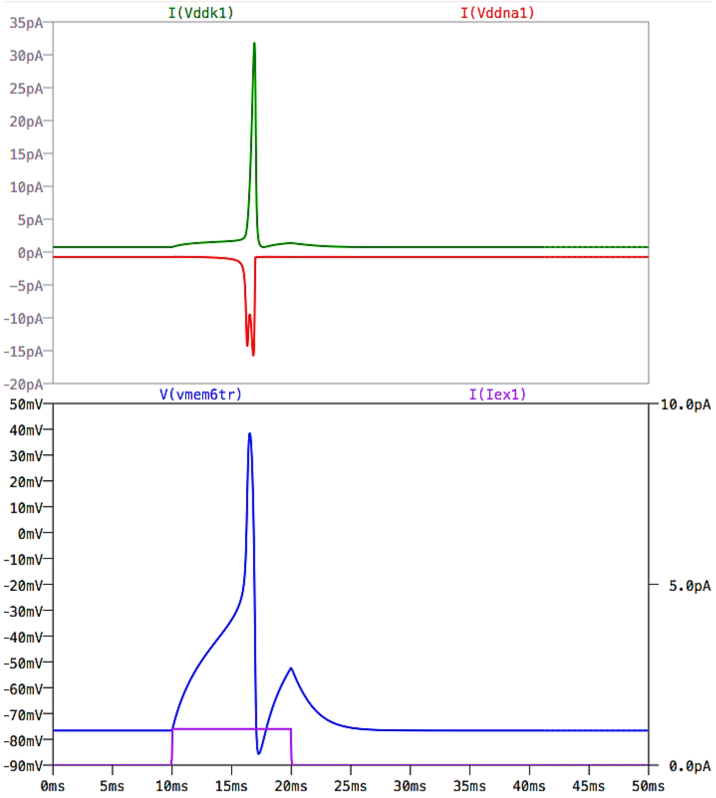

Figure 3.7 Response of the biomimetic neuron with 6 transistors to a pulsed current. With Iex = 1pA and Ts = 10ms. I(VddK1) corresponds to the potassium current (IK); I(Vddna1) corresponds to the sodium current (INa). The action potential is in blue V(vmem6Tr) and the excitatory current is I(Iex1) in pink.

© 2018 Tous droits réservés.

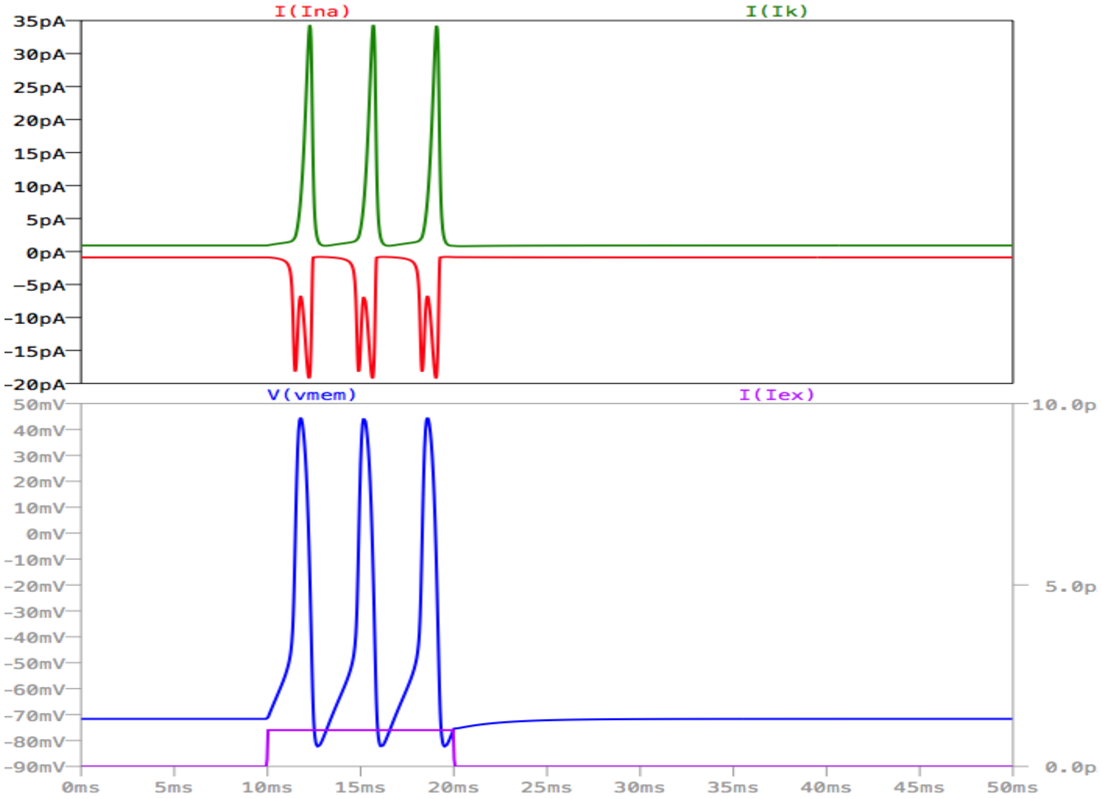

Figure 3.8 Response of the biomimetic neuron with 8 transistors to a pulsed current. With Iex = 1pA and Ts = 10ms. I(Ik) corresponds to the potassium current (IK) and I(Ina) corresponds to the sodium current (INa). The action potential is in blue V(vmem) and the excitatory current I(Iex) is in pink.

In the previous section, we have presented the analogy between the artificial neuron and ML neuronal model. We simulated the biomimetic circuit with LTspice and Cadence software. The results of these simulations have been compared with the Wei model, which enabled us to choose the set of design parameters for the biomimetic neuron. These parameters are presented in the **Table 3.2** and **Table 3.3**.

© 2018 Tous droits réservés.

MP_1	**MP_2**	**MP_3**	**MP_{Na}**
400nm	580nm	120nm	600nm
MN_1	**MN_2**	**MN_3**	**MN_K**
120nm	120nm	650nm	1.83µm
C_m		**C_K**	
50fF		100fF	

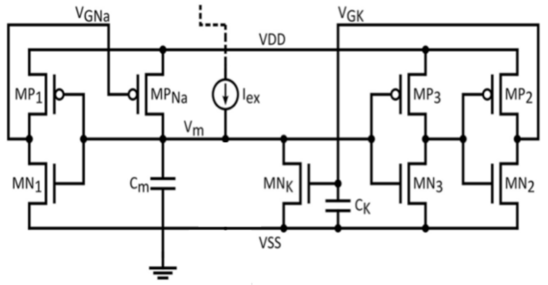

Biomimetic neuron circuit with 8 transistors

Table 3.2 Biomimetic circuit parameters with 8 transistors. All Transistor have a gate length of Lg = 65nm.

MP_1	**MP_2**	**MP_{Na}**
720nm	720nm	1.44µm
MN_1	**MN_2**	**MN_K**
120nm	120nm	1.44µm
C_m		**C_K**
50fF		100fF

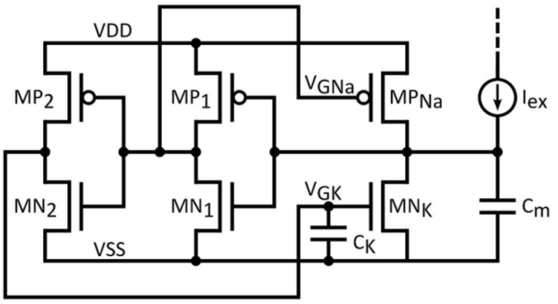

Biomimetic neuron circuit with 6 transistors

Table 3.3 Biomimetic circuit parameters with 6 transistors. All Transistor have a gate length of Lg = 65nm.

As mentioned before in these circuits the excitatory current (Iex) is produced by a PMOS transistor with a gate length of Lg = 65nm and a gate width of w = 120nm. The main difference between these two biomimetic circuit beside the number of used transistors remains in the flexibility to modulate the threshold voltage. The threshold voltage is modulated with the first inverter (MP_1/MN_1). In the circuit with 6 transistors the first inverter is also connected to the potassium transistor (MN_K). The circuit with 8 transistors enables an independent modulation of the threshold voltage due to the presence of a third inverter (MP_3/MN_3) connected to the potassium transistor. Hence it offers the possibility to adjust with accuracy the threshold voltage of the spike around -50mV, without impacting the potassium transistor. Hence, we have chosen the design of the biomimetic neuron with 8 transistors to be fabricated and from here now we will analyze the results from this biomimetic neuron.

© 2018 Tous droits réservés.

3.3.2 Comparison between biological neuron and biomimetic circuit

In this part, we will compare the response of the biomimetic neuron (8 transistors) to the Matlab resolution of the Wei model for the same normalization coefficient ξ = 20A/F. The Wei model simulation will be referred as the biological neuron. As shown in **Figure 3.9**, one spike is obtained for both neurons. In this case, the amount of injected charge for the biological neuron and the biomimetic neuron are respectively Q = 35nC/cm^2 and Q' = 2.5fC. This number of charges is obtained for two different excitatory currents: Iex = 20µA/cm^2 during Ts = 1.75ms in the case of the biological neuron and Iex' = 1pA during Ts' = 2.5ms for the biomimetic neuron. This first result indicates that similar behaviors are observed and the study was continued with higher injected charges. As illustrated in **Figure 3.10**, we observe the generation of two spikes. In this case the amount of injected charge for the biological neuron and the biomimetic neuron are respectively Q = 175nC/cm^2 and Q' = 5fC. The corresponding excitatory current for the biological neuron is Iex = 20µA/cm^2 during Ts = 8.75ms and Iex' = 1pA during Ts' = 5ms for the biomimetic neuron. A good agreement is also noticed in this case.

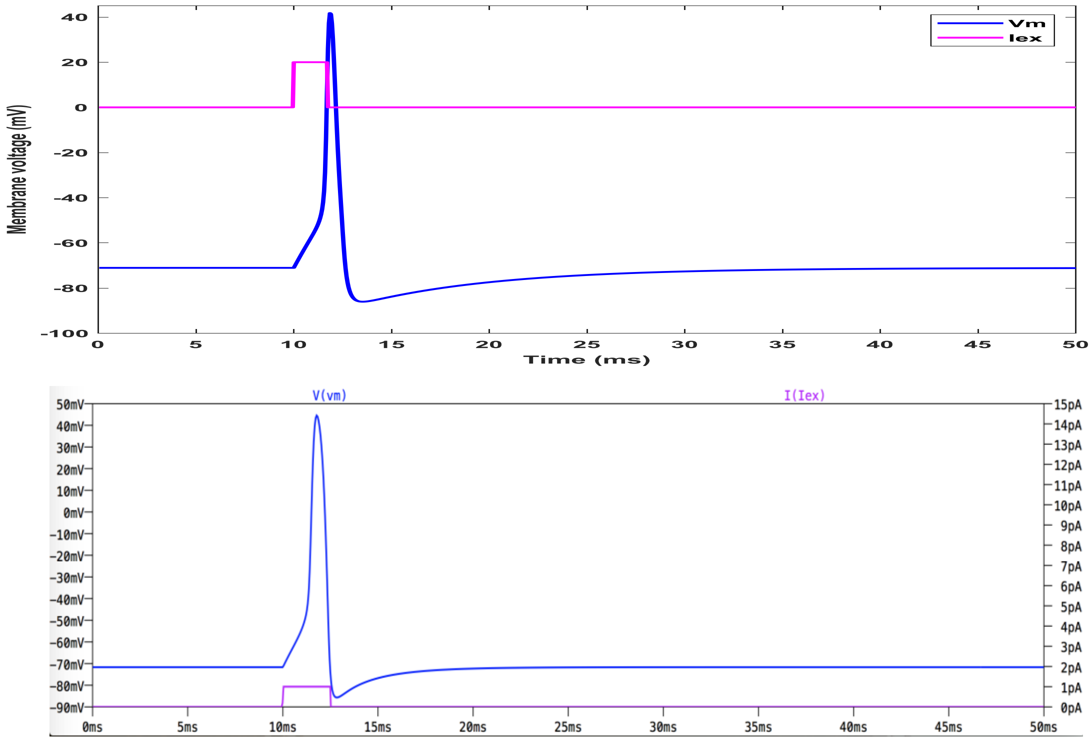

Figure 3.9 One spike in response to an excitatory pulse. Biological neuron (up) response to injected charge of Q = 35nC/cm^2 and biomimetic neuron response (down) to injected charge of Q' = 2.5fC pulse of excitatory current with ξ = 20A/F. One spikes is generated for both neurons.

© 2018 Tous droits réservés.

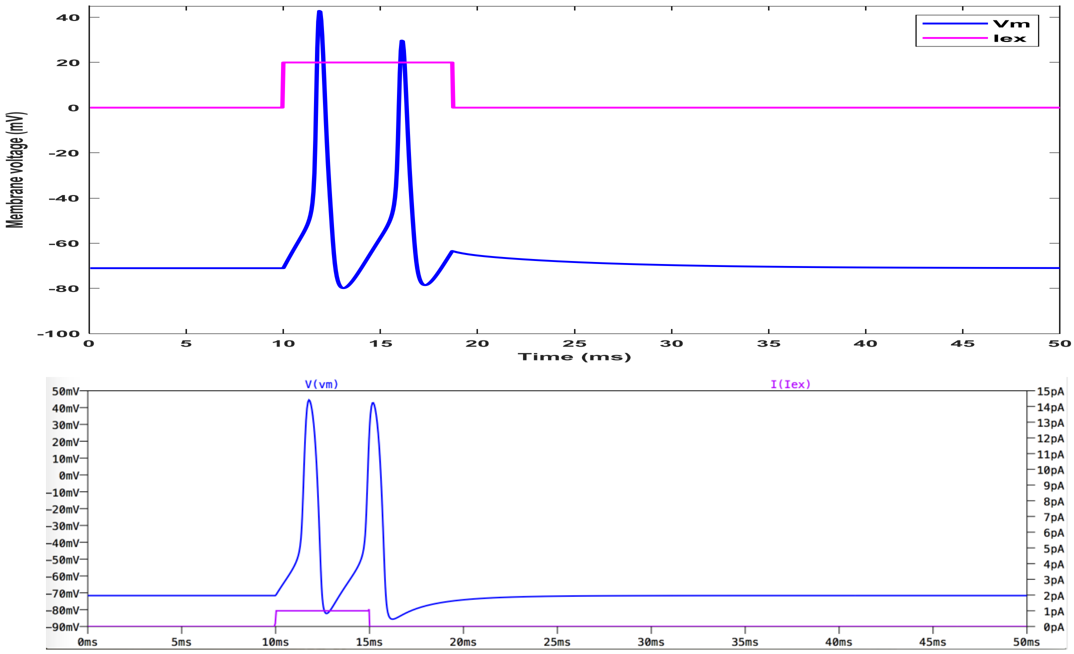

Figure 3.10 Two spikes in response to an excitatory pulse. Biological neuron response (up) to injected charge Q = 175nC/cm^2 and biomimetic neuron response (down) to injected charge of Q' = 5fC a pulse of excitatory current with ξ = 20A/F. Two spikes are generated for both neurons.

Three spikes are obtained as shown in **Figure 3.11**, for Q = 200nC/cm^2 and Q' = 10fC with Iex = 20µA/cm^2 during Ts = 10ms in the case of the biological neuron and Iex' = 1pA during Ts' = 10ms for the biomimetic neuron. As illustrated in **Figure 3.9** to **Figure 3.11**, the peak-to-peak amplitude (Vpp) is around 130 mV, in the range between 40 mV and -90 mV that respect the biasing of the biological neuron as it is a constraint between E_{Na} = 55mV and E_K = -94mV.

© 2018 Tous droits réservés.

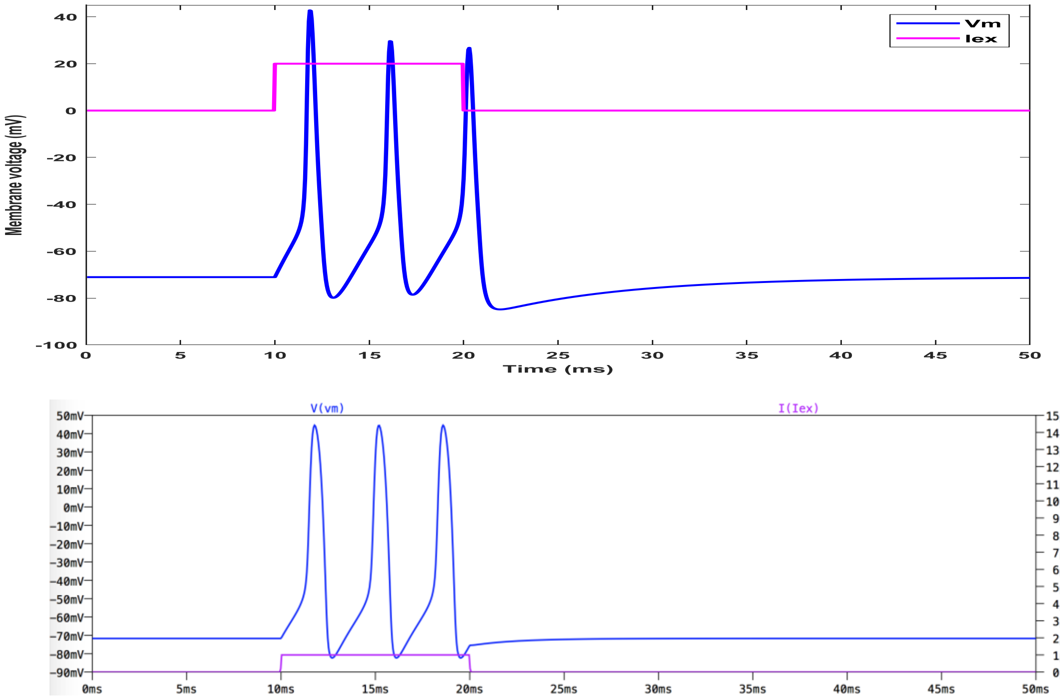

Figure 3.11 Three spikes in response to an excitatory pulse. Biological neuron response (up) to injected charge Q = 200nC/cm^2 and biomimetic neuron response (down) to injected charge of Q' = 10fC to a pulse of excitatory current with $\xi = 20$A/F. Three spikes are generated for both neurons.

As illustrated in **Figure 3.9** to **Figure 3.11** similar responses are obtained for both biomimetic neuron and biological neuron. For both neurons, the ratio of excitatory current and membrane capacitance, i.e. the normalizing coefficient, is ξ =20A/F. Therefore, we demonstrate the precise modulation of the number of spikes for both biomimetic artificial and biological neuron with the same normalizing coefficient. As shown in the above figures, as we increase the amount of injected charge (Q and Q') the number of spikes increases. This validates the second criteria mentioned before: the amount of the injected charge plays a central role in the excitatory behavior of the neuron.

In the next paragraph, we will compare the extracted parameters from the spike obtained with the biological neuron to the spike obtained with the biomimetic neuron. As reported in **Table 3.4**, the resting potential (V_{rest}) and the threshold voltage (V_{th}) for both neurons are respectively -70mV and -50 mV. We obtain the same values with the cadence simulation of the biomimetic neuron.

© 2018 Tous droits réservés.

Parameters	**V_{rest} (mV)**	**V_{th} (mV)**	**V_{pp_max}(mV)**	**AR_p (ms)**
Biological neuron	-70	-50	120	4
Biomimetic neuron	Adjustable -70	Adjustable -50	Adjustable 120	Adjustable 3.5

Table 3.4 Spiking characteristics for constant ξ. The spike generated from biological neuron (Wei neuron) is compared to the one from biomimetic neuron. Same normalization coefficient ξ = 20A/F is used for both neurons.

The design of the biomimetic neuron is flexible as we can adjust the parameters presented in the **Table 3.4**. As mentioned before, V_{rest} is modulated with the leak conductance, the V_{th} is adjust with the first inverter, V_{pp} varies with the drain bias and ARp depends on the excitatory current.

The peak width (PW) is defined at the threshold voltage (V_{th}) of the neuron while the spike width (SW) is defined at the minimum point (Min_{point}) of the spike (see **Figure 3.12**).

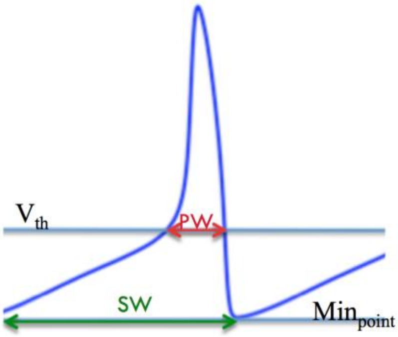

Figure 3.12 Spike, peak width (PW) and spike width (SW).

A comparison of PW and SW of the biological neuron and the biomimetic neuron is reported in **Table 3.5**.

© 2018 Tous droits réservés.

	For 1 spike in Figure 3.9		**For 2 spikes in Figure 3.10**		**For 3 spikes in Figure 3.11**	
Spike parameters	PW (ms)	SW (ms)	PW (ms)	SW (ms)	PW (ms)	SW (ms)
Biological neuron	1.15	10	1.21	4.35	1.25	4.35
Biomimetic neuron	1.28	7.7	1.26	3.56	1.25	3.44

Table 3.5 Comparison of Peak Width (PW) and SW (Spike Width) between the spike of biological and biomimetic neuron.

As shown in **Table 3.5**, the peak width and the spike width of both neurons are similar. These close comparisons between these parameters validate the similarity between the biomimetic neuron and the biological neuron in terms of spike shape and excitatory response to an external stimulation. Therefore, we validate the first criteria mentioned previously; reproduce the exact shape of the spike based on defined parameters. These results validate the design of the biomimetic neuron patterned from Wei model.

© 2018 Tous droits réservés.

3.4 Design of fast neuron

As shown in the previous section for biomimetic neuron, we choose to take in account two different criteria in order to generate action potentials similar to those in living neuron. For the design of the fast neuron, our purpose was to achieve a higher spiking frequency rate and a better energy efficiency with a compact design in order to build networks with several thousands of artificial neurons. These performances are obtained by trading off the biological accuracy for higher frequency and reduced silicon area.
These targets were reached by reducing the value of the capacitances C_m and C_K of one order of magnitude. Reducing the capacitances values affect the time constant of the spike and the frequency of the circuit. A satisfying spike shape was obtained even though we removed the leak and the third inverter of the artificial neuron. The reduction of the number of inverters will reduce the design flexibility of the artificial neuron concerning the threshold voltage as described before in the biomimetic section.
These modifications are the main characteristics of the fast neuron. The fast neuron is composed of few elementary devices: two inverters (MP_1/MN_1 and MP_2/MN_2), sodium and potassium transistors (MP_{Na} and MN_K), membrane and potassium capacitances (C_m and C_K). The schematic of the fast neuron as well as the design parameters are illustrated in **Table 3.6**.

<table>
<tr><th colspan="2">MP_1</th><th colspan="2">MP_2</th><th colspan="2">MP_{Na}</th></tr>
<tr><td colspan="2">300nm</td><td colspan="2">360nm</td><td colspan="2">400nm</td></tr>
<tr><th colspan="2">MN_1</th><th colspan="2">MN_2</th><th colspan="2">MN_K</th></tr>
<tr><td colspan="2">600nm</td><td colspan="2">120nm</td><td colspan="2">1.2µm</td></tr>
<tr><th colspan="3">C_m</th><th colspan="3">C_K</th></tr>
<tr><td colspan="3">4fF</td><td colspan="3">8fF</td></tr>
</table>

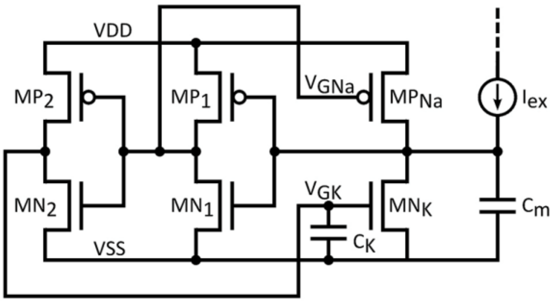

Fast neuron circuit with 6 transistors

Table 3.6: Fast circuit parameters with 6 transistors. All transistor have a gate length of Lg = 65nm.

The fast neuron with design parameters presented in **Table 3.6** was simulated and reproduces the excitability of the neuron with a reduced silicon footprint and a higher frequency performance. The shape of the generated spikes and the excitability of the neuron are still satisfying as illustrated in **Figure 3.13**. The spike amplitude is between -100mV and 60mV with following biasing for the fast neuron circuit: VDD = 100mV, VSS = -100mV and the excitatory current of I_{ex} = 40pA during T_s = 200µs.

© 2018 Tous droits réservés.

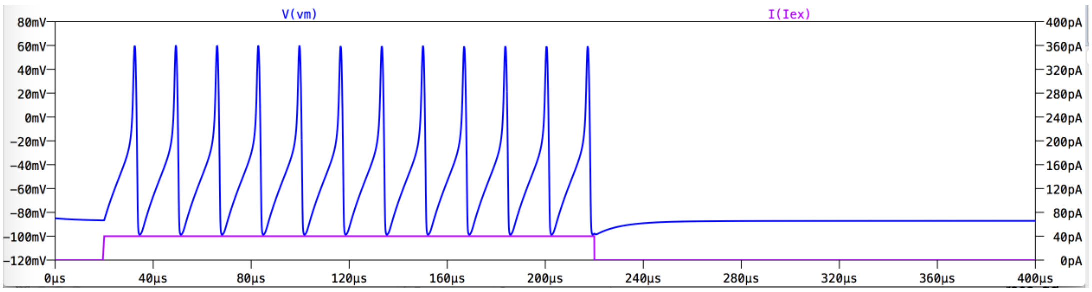

Figure 3.13 The Fast neuron circuit response to a pulsed excitation. Spike train for an excitatory current of I_{ex}=40pA during T_s=200µs.

The spike width for the fast neuron is SW = 16µs. The peak width is defined at the threshold voltage (in this case V_{th} = -20mV), which corresponds to PW = 5µs. We observe a three orders of magnitude difference between SW and PW of the fast neuron versus the biomimetic ones (In the biomimetic neuron: PW = 1.25ms and SW = 3.44ms for three spikes). The resting potential V_{rest} is -90 mV. We observe a 20mV difference as we compare the V_{rest} of the fast neuron (-90mV) to the V_{rest} of biomimetic neuron (-70mV). There is 30mV difference between the V_{th} of the fast neuron (-20mV) and the V_{th} of the biomimetic neuron (-50mV). Therefore, the shape of the spike is slightly different from the biological spike. Nevertheless, the excitatory response remains the same.

The fabricated biomimetic neuron with the design parameters presented in **Table 3.2** and the fast neuron with the design parameters presented in **Table 3.6** as well as their corresponding performances will be presented in the following sections.

© 2018 Tous droits réservés.

3.5 Fabrication of artificial neurons

The neuro-inspired circuits described in the previous sections have been designed and fabricated using TSMC 65nm CMOS process in the LP option. The test chip was called WetWire and its dimensions were 1.2mm x 2.1mm. The WetWire chip contains a variety of neuron circuits including different designs of the biomimetic (with and without leak conductance) and fast neuron, different versions of connected biomimetic to biomimetic neuron and finally connected biomimetic neuron to fast neuron called also tonic-Burst circuit. The connection of these neurons is made through excitatory and inhibitory synapses. Without accounting for the output driving buffer or protection circuitry, the area occupied by the biomimetic neuron is 200µm^2. This value decreases radically for the fast neuron with 35µm^2 due to its low C_m and C_K values. In fact, the capacitors dominate the area utilization, 65% for the fast and 70% in the biomimetic neuron. The fabricated chip is shown in **Figure 3.14**. The biomimetic neuron and fast neuron (referred as simplified neuron) are illustrated on the photographed of WetWire chip (**Figure 3.14.a**).

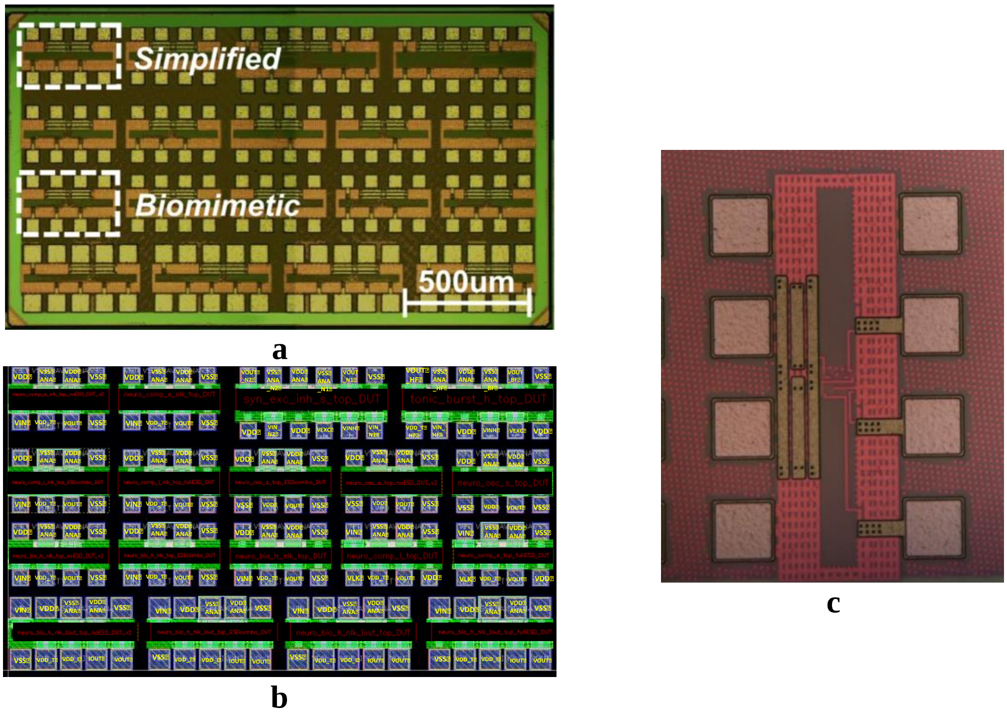

Figure 3.14 a: Die photographs of the fabricated WetWire chip. The highlighted DUTs, each one sized 450 x 250µm, refer to the two neuron circuit variants: biomimetic (core size: 200 µm^2) and fast or simplified (core size: 35 µm^2). **Figure 3.14.b:** all 18 circuits of the WetWire chip with their respective input and output pads. **Figure 3.14.c:** fabricated biomimetic neuron and its 8 pads.

All these circuits were designed with external biasing pads as shown in **Figure 3.14.b**. The excitation was implemented with on-chip trans-conductance, a PMOS transistor (w = 120nm Lg = 65nm). This trans-conductance is externally biased through VIN and

© 2018 Tous droits réservés.

VDD_T pads (see **Figure 3.14.b** and **Figure 3.16**). The VIN pad is connected to the gate of the PMOS as the VDD_T pad is connected to the source of the PMOS transistor (**see Figure 3.16**). The output signal was monitored through an on-chip unity gain output buffer designed to ensure that the frequency response of the neuron circuit would not be affected (see **Figure 3.15).**

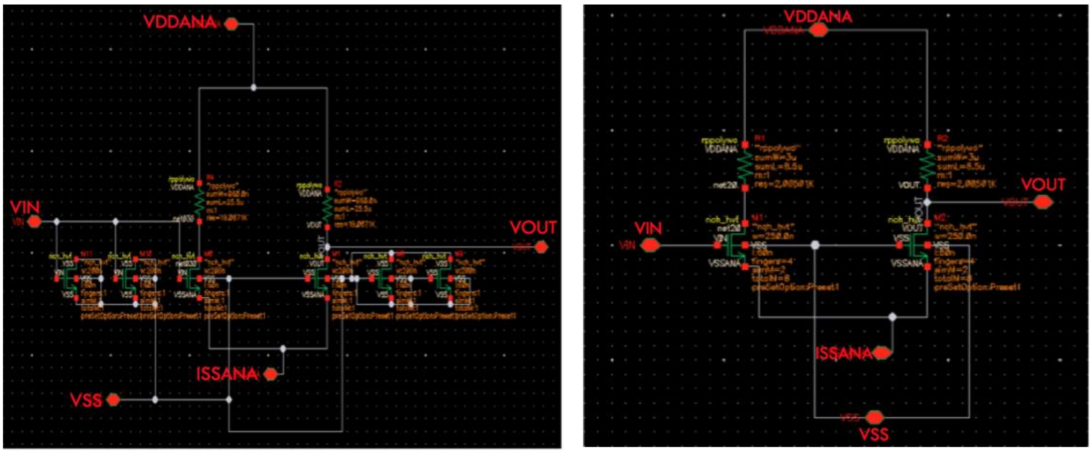

Figure 3.15 Left: Buffer for the biomimetic neuron **Right:** Buffer for the fast neuron.

The output buffer featured independent DC supply through the VDDANA and ISSANA pads (see **Figure 3.15** and **Figure 3.16**). These independent DC supplies enable accurate power consumption measurements while the neuron's bias pins were not ESD protected. We will describe the result of these characterizations in the following sections.

In summary, as shown in the **Figure 3.16,** the VIN pad corresponds to the excitatory input, connected to the gate of the PMOS trans-conductance. VDD and VSS are respectively the drain and the source bias of the artificial neuron. The VDD_T pad corresponds to the source of the PMOS trans-conductance.

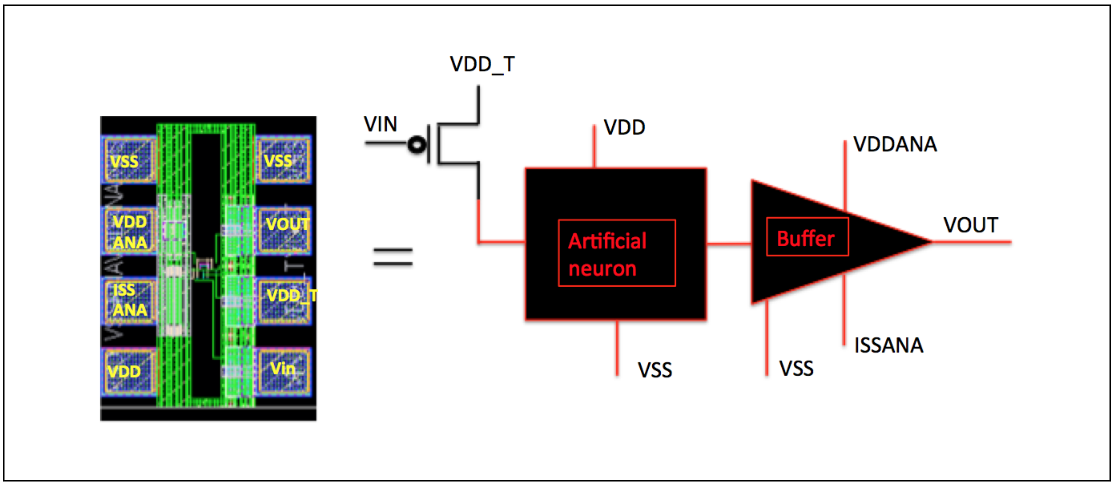

Figure 3.16 The fabricated biomimetic neuron and fast neuron (left). The schematic of biomimetic neuron and fast neuron (right) connected to the buffer. As shown, 7 pads must be biased in order to characterize these artificial neurons.

© 2018 Tous droits réservés.

VDDANA and ISSANA are pads to bias the artificial neuron's buffer. The output signal is observed from the VOUT pad, which corresponds to the membrane voltage (Vmem). These eight pads (except the VOUT) are biased in order to characterize the neuron circuit. The detailed set up of the test bench will be presented in the next section.

© 2018 Tous droits réservés.

lilliad.univ-lille.fr

3.6 Characterization of Wet Wire chip

3.6.1 Test bench of WetWire chip

The experimental test bench as shown in **Figure 3.17** was constituted of several instruments. For the neuron excitation, we used a Keysight 33500B series waveform generator, which biases the VIN pad. The Keithley 2636A system source meter has been used to bias VSS. Two Agilents SMU (E5273A and E6263A) containing two channels, are used to bias VDD, VDD_T, VDDANA and ISSANA pads. The Agilent SMU supplies used for biasing these pads also enabled us to perform the measurement of the average current with nominal 500fA accuracy. The values used for biasing the biomimetic and fast neuron are reported in the **Table 3.6**.

Biasing Pads	**VIN**	**VDD**	**VDD_T**	**VDDANA**	**ISSANA**	**VSS**
Biomimetic neuron	≤200mV	200mV	200mV	300mV	-43µA	0V
Fast neuron	≤200mV	200mV	200mV	300mV	-400µA	0V

Table 3.6 Bias for the biomimetic and fast neuron of the Wet Wire chip.

The VIN varies between 0 to 200mV. For VIN = 0, the PMOS transistor is open and thus the neuron spikes with a maximal frequency. In contrary, for VIN = 200mV, the PMOS transistor is completely closed and the neuron does not spike. The output signal issued from the buffer was monitored by ROHDE & SCHWARZ oscilloscope 500MHz 5GSa/s, in order to perform frequency, amplitude and spike width measurements.

© 2018 Tous droits réservés.

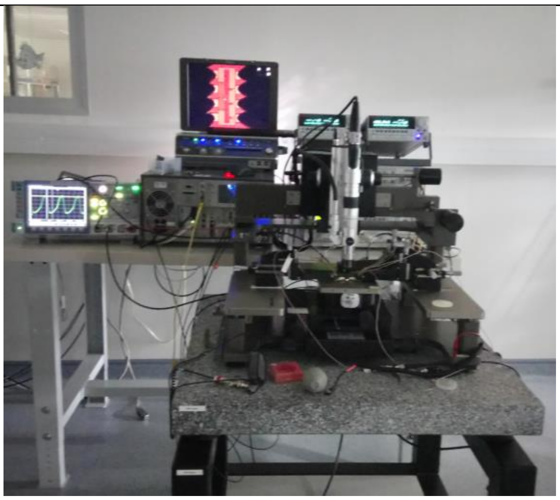

The WetWire test bench.

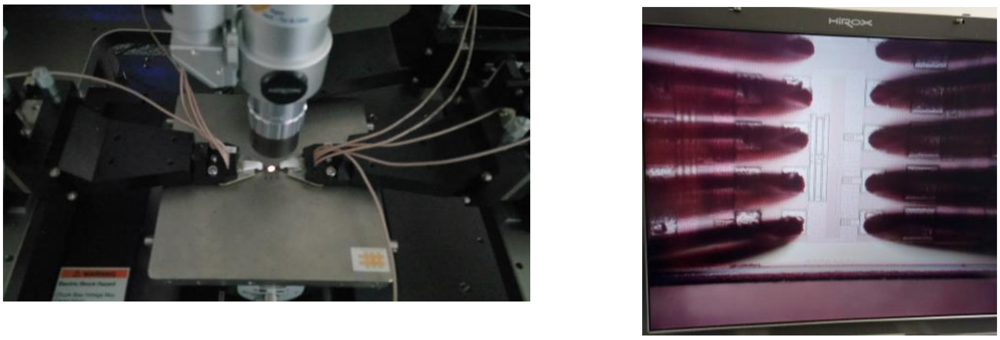

Under probe measurements.

Biomimetic neuron under probes.

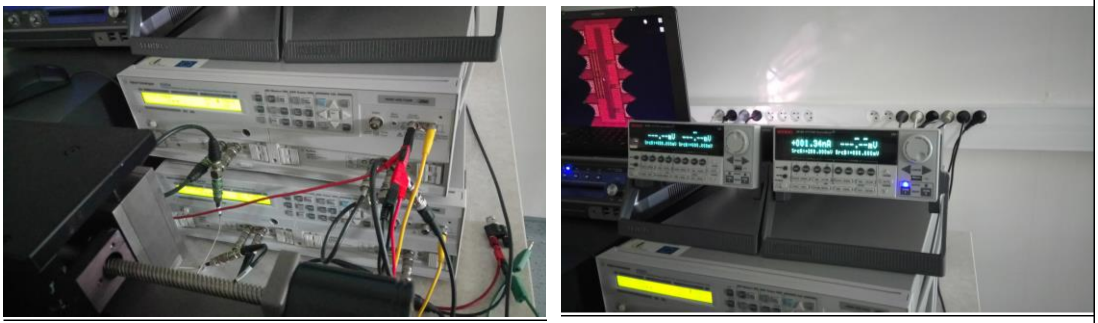

Two Agilents SMU (E5273A and E6263A) connected to VDD, VDD_T, VDDANA and ISSANA pads.

One Keithley 2636A connected to VSS.

Figure 3.17 Photographs of the test bench.

© 2018 Tous droits réservés.

3.6.2 Pulsed characterization of biomimetic and fast neuron

In this part, we will demonstrate experimentally the generation of spikes with the biomimetic and the fast neuron and compare the biomimetic spike to the spike obtained by Wei model. The aim of this part is to verify that the injection of different amount of charges leads to the generation of different number of spikes from the artificial neuron. The input excitation, VIN is defined with two levels as follows: VIN_High corresponds to the maximal value of the pulse and VIN_low is the minimal value of the pulse. The Keysight generator enables us to define the duration of this pulse (Tp).

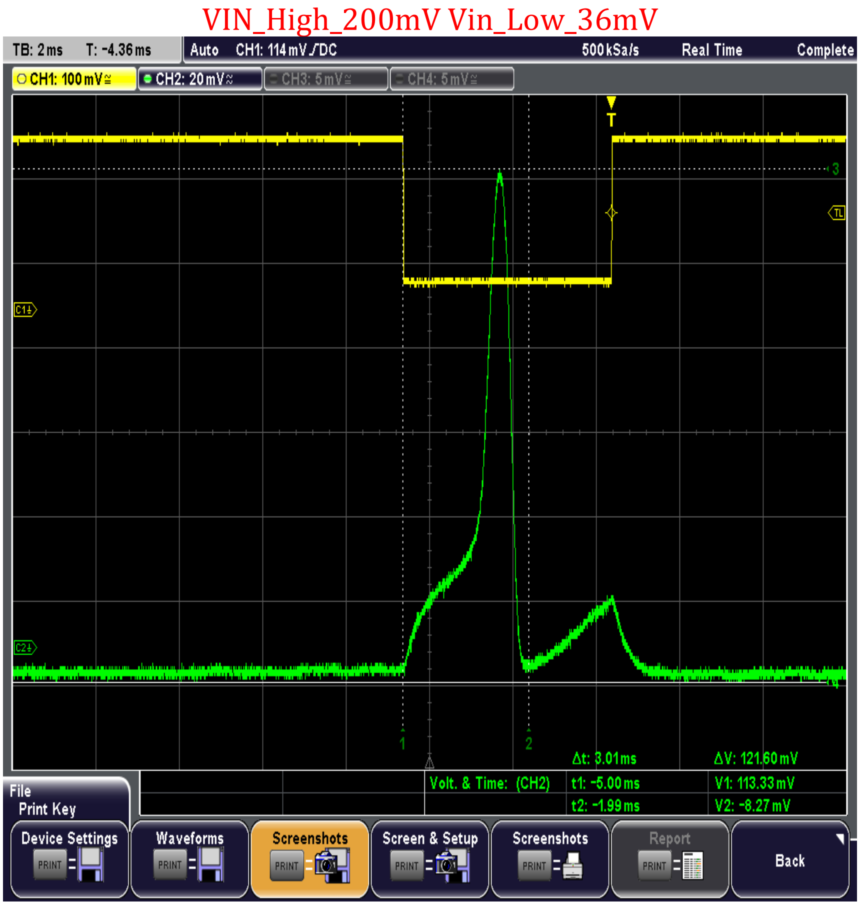
VIN_High_200mV Vin_Low_36mV

Figure 3.18 Biomimetic neuron circuit generates one spike Tp = 4ms.

As shown in **Figure 3.18** to **Figure 3.20,** the biomimetic neuron generates experimentally one, two and three spikes for different values of VIN_Low, which corresponds to different excitatory currents. The excitation current IE corresponding to VIN_Low = 36mV **Figure 3.18**, is less than 1pA and it increases as the VIN_Low decreases from 36mV to 25mV.

© 2018 Tous droits réservés.

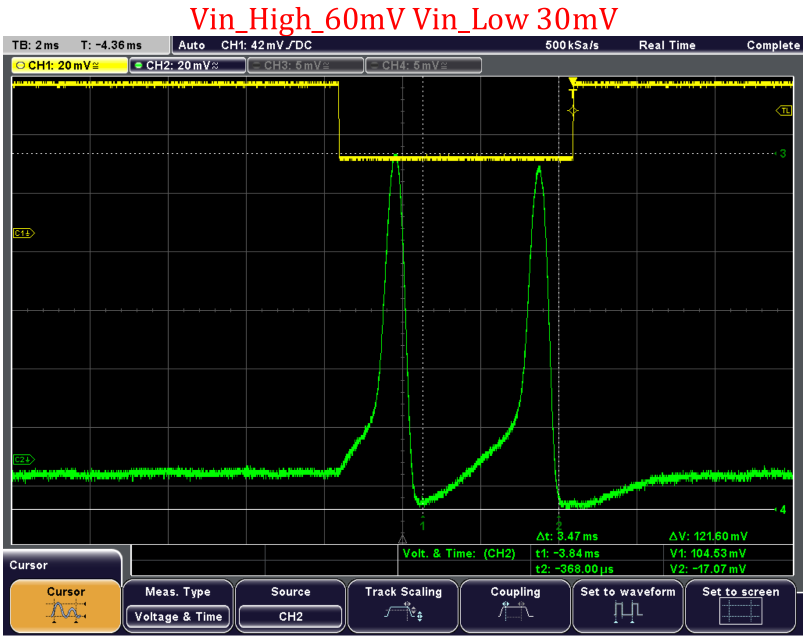

Figure 3.19 Biomimetic neuron circuit generates two spikes Tp = 6ms.

As it can be noticed, Tp increases from 4ms in **Figure 3.18** to 10ms in **Figure 3.20**. Hence, we can conclude that the overall injected charge increases, which modulates precisely the generation of spikes as we expected. In fact, as described in chapter 2, we have demonstrated the precise modulation of the number of spikes based on the injected charge, which is also demonstrated experimentally in this part.

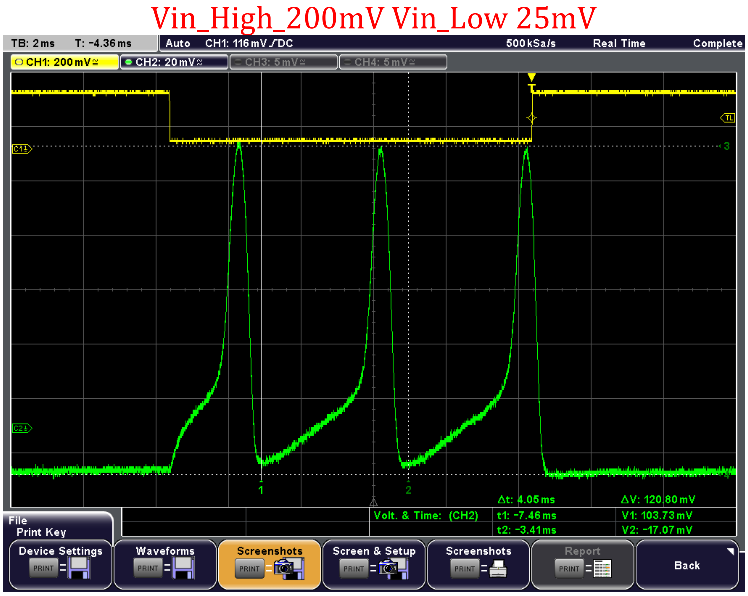

Figure 3.20 Biomimetic neuron circuit generates three spikes Tp = 10ms.

The output waveform of the fast neuron is shown in **Figure 3.21**. In this case, for an excitatory current IE = 150pA, the fast neuron generates a spike train with a spike width

© 2018 Tous droits réservés.

around 40µs and a peak-to-peak amplitude of 112mV. In fact, the fast neuron frequency is higher than the one in the biomimetic neuron.

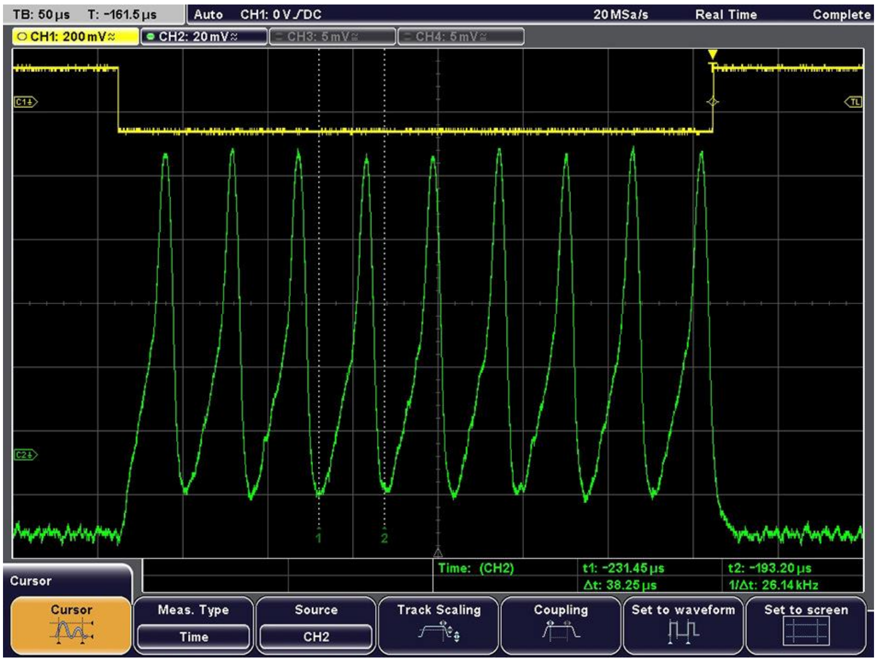

IE = 150pA

TB: 50 µs T: −161.5 µs

Auto CH1: 0 V ⁄ DC

20 MSa/s Real Time Complete

CH1: 200 mV

CH2: 20 mV

CH3: 5 mV

CH4: 5 mV

Time: (CH2)

t1: −231.45 µs

Δt: 38.25 µs

t2: −193.20 µs

1/Δt: 26.14 kHz

Meas. Type: Time

Source: CH2

Figure 3.21 Example of output waveform for fast neuron. Pulsed VIN resulting in constant current excitation IE = 150pA.

In this section, we have demonstrated the ability of these artificial neurons to be externally excited using an amount of charge Q, as in biology.

3.6.3 Comparison of biomimetic pulsed characterization with Wei model

To validate the design of a biomimetic neuron, which provides physiological spikes, we will compare the spikes of the biomimetic neuron to the ones issued from Wei model. In **Figure 3.22**, the spike of the Wei model (Matlab simulation) is compared to the spike obtained with the fabricated biomimetic neuron (Fab_circuit). In both cases, the excitation pulse is applied during the same period T'' = 10ms. The excitatory currents applied in to the simulation and in to the Fab_circuit are respectively Iex = 20µA/cm^2 and Iex' = 1pA. Based on these values, we defined a normalization coefficient, as the ratio of the excitatory current and the membrane capacitance. We obtain 20A/F for both cases with C_m = 1µF/cm^2 for the simulation and C_m' = 50fF for the Fab_circuit. The peak-to-peak amplitude of the spike from the Wei model varies and have a maximal value of V_{ppmax}= 120mV and minimal value of V_{ppmin}= 97mV. For the biomimetic neuron (Fab_circuit), the peak-to-peak amplitude remains constant at V_{pp} = 122mV. The peak-to-peak values are thus similar. The spike width in both cases are SW = 4ms.

© 2018 Tous droits réservés.

Vin_High_200mV Vin_Low_25mV

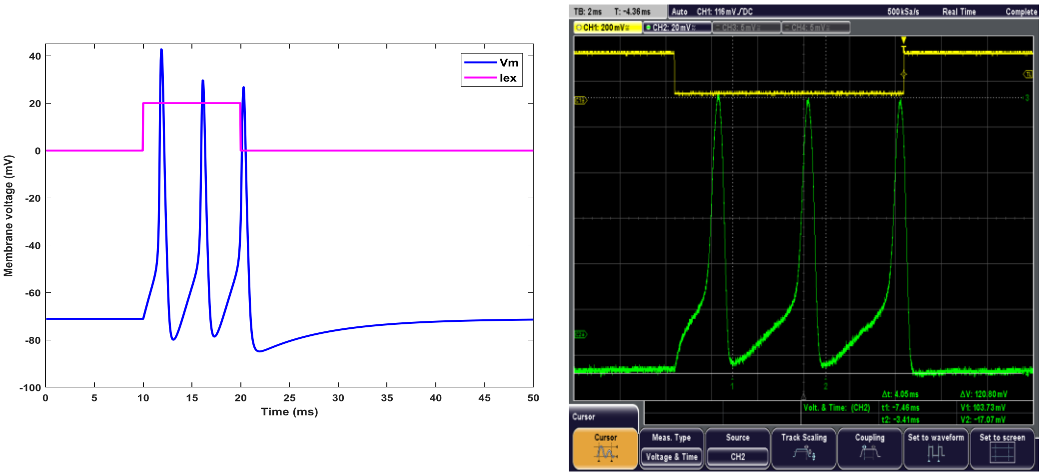

Volt. & Time: (CH2)
Δt: 4.05 ms ΔV: 120.80 mV
t1: -7.46 ms V1: 103.73 mV
t2: -3.41 ms V2: -17.07 mV

Figure 3.22 Comparison between Wei model and fabricated biomimetic circuit. Left: Wei model. Right: biomimetic circuit (Fab_circuit).

Before presenting in detail the performance of the biomimetic and the fast neuron, we will present the results issued from the oscillatory neuron and the tonic burst circuit of the WetWire chip.

3.6.4 Characterization of oscillatory neuron

The oscillatory neuron (or unstable neuron) is designed to spike without any excitation, as it does not have a resting state due to the absence of an inhibitory synapse. The bias of the oscillatory neuron pads are VDD = 200mV, VSS = 0mV, VDDANA = 300mV, ISSANA = -400µA, VDD_T = 200mV, VIN = 0V. The resulting spikes shown in **Figure 3.21** have a frequency of 3.42kHz and peak-to-peak amplitude of 182mV.

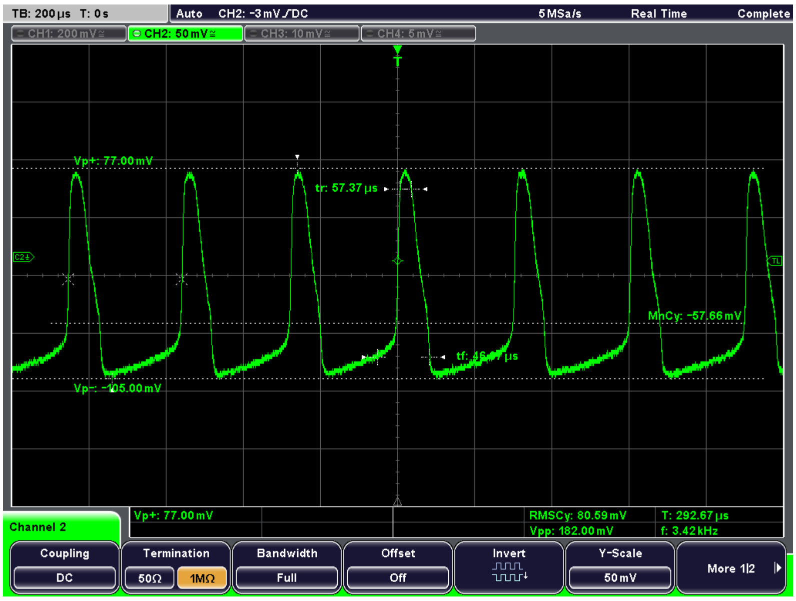

Vp+: 77.00 mV
tr: 57.37 µs
MnCy: -57.66 mV
tf: 46.… µs
Vp-: -105.00 mV
Vp+: 77.00 mV
RMSCy: 80.59 mV
Vpp: 182.00 mV
T: 292.67 µs
f: 3.42 kHz

Figure 3.23 Spike train of oscillatory neuron.

© 2018 Tous droits réservés.

3.6.5 Characterization of tonic-burst circuit

The so-called tonic-burst circuit will generate a particular spiking mode of neurons called bursting (Fox, Rotstein, & Nadim, 2016). It leads to a particular generated pattern consisting of fast spiking separated by intervals of quiescence. In order to emulate the bursting mode, we consider the schematic shown in **Figure 3.24**.

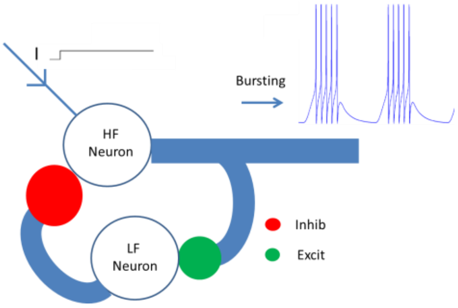

Figure 3.24 Schematic for the tonic-burst circuit.

This tonic burst schematic is based on the association of a biomimetic neuron (referred as “low frequency” –LF- Neuron in **Figure 3.24**) with a Fast neuron (referred to high frequency –HF- Neuron in **Figure 3.24**). A key point stands in the different dynamics obtained by the HF and LF neurons. The HF neuron is connected to the LF neuron through an excitatory synapse. However, the LF neuron is connected to the HF neuron through an inhibitory synapse. This tonic-burst circuit behaves following this principle. First, the HF neuron is firing when an excitatory current is applied. Then, due to the connection between HF and LF neuron through an excitatory synapse, the membrane capacitance of the LF neuron integrates the synaptic current induced by every HF neuron spike. When the LF neuron membrane potential reaches its threshold, it starts to fire with spike duration much higher than the HF neuron ones. Because of the inhibitory synapse between these two neurons, the HF neuron is quickly inhibited. Finally, when the LF neuron repolarizes, the HF neuron depolarizes and fires again. This cycle holds as long as HF neuron is excited (see **Figure 3.24**). This circuit was implemented on WetWire chip under the name of " tonic_burst_h_top_DUT". The biases for this circuit are reported in the **Table 3.7**.

ISSANA_BF	ISSANA_HF	VDD	VDD_T	VDDANA	VSS	VIN_HF
-42µA	-42µA	200mV	200mV	300mV	0V	<200mV

Table 3.7 Bias values for the tonic-burst circuit also identified as tonic_burst_h_top_DUT on the Wetwire chip.

The spike generation of HF and LF neurons as a function of the input excitation VIN_HF is shown in **Figure 3.25**. The output spikes of HF and LF neuron are represented by Vout_HF and Vout_LF, respectively.

© 2018 Tous droits réservés.

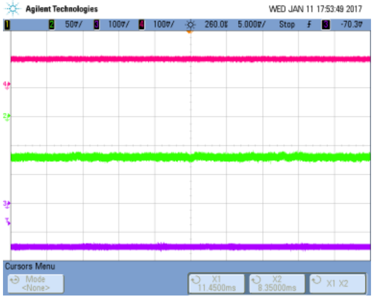	VIN_HF Vout_HF Vout_LF	HF generates no spikes for VIN_HF = 83mV
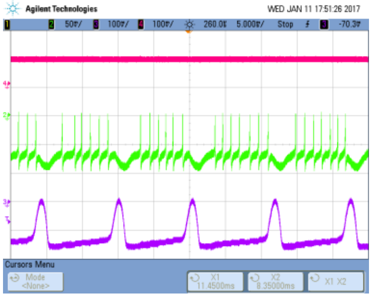	VIN_HF Vout_HF Vout_LF	HF generates 6 spikes for VIN_HF = 82mV
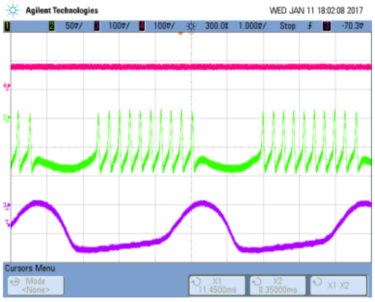	VIN_HF Vout_HF Vout_LF	HF generates 10 spikes for VIN_HF = 62mV
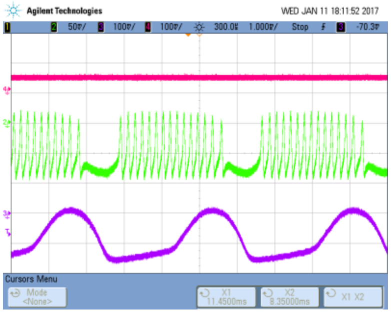	VIN_HF Vout_HF Vout_LF	HF generates 15 spikes for VIN_HF = 35mV
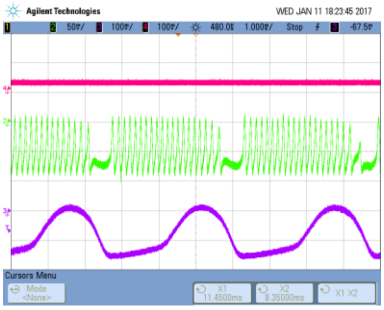	VIN_HF Vout_HF Vout_LF	HF generates 20 spikes for VIN_HF = 16mV

Figure 3.25 Experimental spikes for the HF and LF neurons used in neuronal networks to emulate bursting mode. The first signal is VIN_HF, the second one is Vout_HF and the third one is Vout_BF. The number of spikes of HF neuron increases as VIN_HF decreases.

© 2018 Tous droits réservés.

When VIN_HF is lower than 82mV, the HF neuron begins to generate spikes (six spikes). The number of spikes increase from 10, 15 and 20 respectively according to the decrease of VIN_HF as follows: VIN_HF = 62, 35 and 16mV (see **Figure 3.26)**. In **Figure 3.25**, we have reported the variation of the number of spikes for the HF neuron in function of the excitatory input (VIN_HF).

It must be underlined that in this circuit design, the excitatory current for the HF neuron increases as VIN_HF decreases. By this way, it results in the increase of the number of spikes observed at the output of the HF neuron. A maximum of 26 spikes is reached for VIN_HF = 0V.

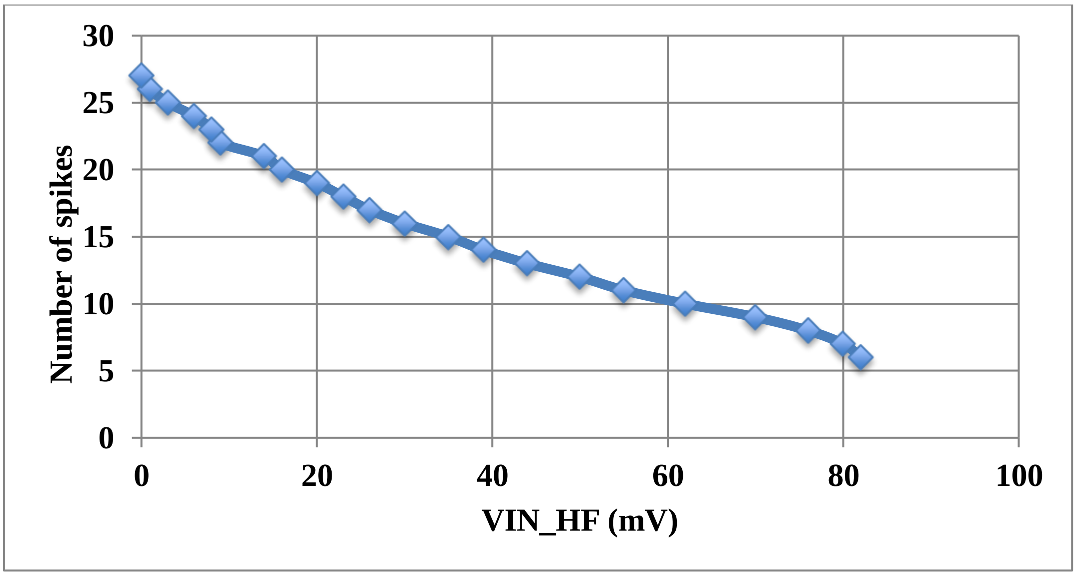

Figure 3.26 Spikes in tonic burst circuit. Number of spikes as a function of VIN_HF.

3.6.6 Biomimetic and fast neuron performance

This part is dedicated to the study of the biomimetic and fast neurons performance. In order to perform this analysis, both the spike frequency and the corresponding average power consumption (including the static and dynamic parts) have been measured as a function of the excitation current. The static power refers to a zero-excitation condition, while dynamic power consumption is deduced from the consumption under constant excitation, which induces a spiking mode. The excitability of the biomimetic neuron is shown in **Figure 3.27**. The minimal observed frequency is around 20Hz. As expected, the firing rate and power consumption increase with the excitatory current.

© 2018 Tous droits réservés.

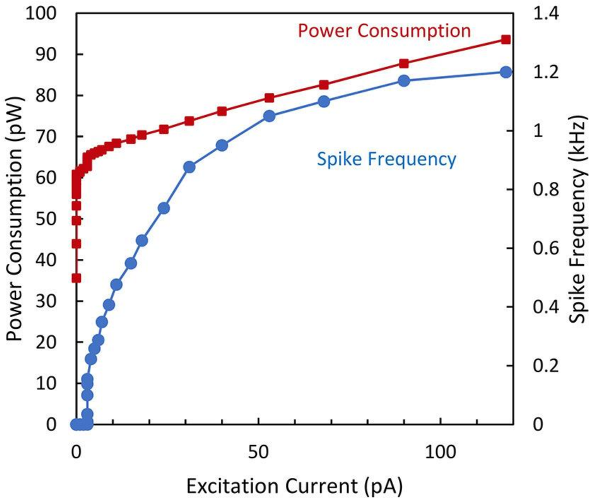

Figure 3.27 Spike frequency and power consumption over the excitation current for the biomimetic neuron.

For Iex = 120pA, a maximal spike frequency of 1.2kHz was obtained with a total dissipated power of 90pW. According to (Izhikevich, 2007), this biomimetic neuron is categorized as a Type I neuron. The energy efficiency of the circuit is deduced from the power dissipation and frequency measurements. In **Figure 3.28**, it is plotted as a function of the excitation current for two cases: (i) when the whole average power (static and dynamic - blue line) is taken into account and (ii) when the standby power (i.e., power consumption at zero excitation current) is subtracted (red line).

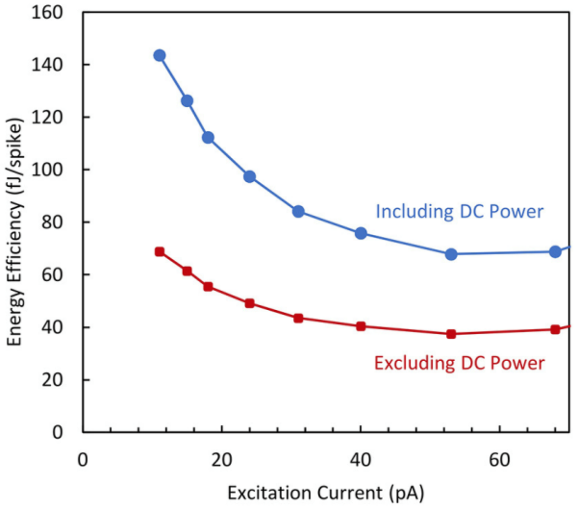

Figure 3.28 Energy efficiency vs. excitation current for the biomimetic neuron when the DC power is included or not from energy estimation.

For excitation current higher than 30pA, the dissipated energy per spike is roughly constant and therefore independent of the spike frequency. An energy efficiency value of 40fJ/spike is obtained when considering the dynamic power consumption. It is worth mentioning that this value is several orders of magnitude lower than the energy

© 2018 Tous droits réservés.

efficiency of actual biological neuron, as it is estimated around the 10pJ range, from the ATP consumption in (Attwell & Laughlin, 2001) (Lennie, 2003) (Poon & Zhou, 2011) and our estimation in chapter 2. This low energy dissipation obtained for the proposed artificial neuron can be interesting for spiking neuron networks applications needing the integration of a large number of neurons.

Concerning the fast neuron, a spike frequency as high as 26kHz was obtained with a total power consumption of 105pW for excitation current Iex = 150pA. The power consumption and spike frequency are illustrated in **Figure 3.29** as a function of the excitation current.

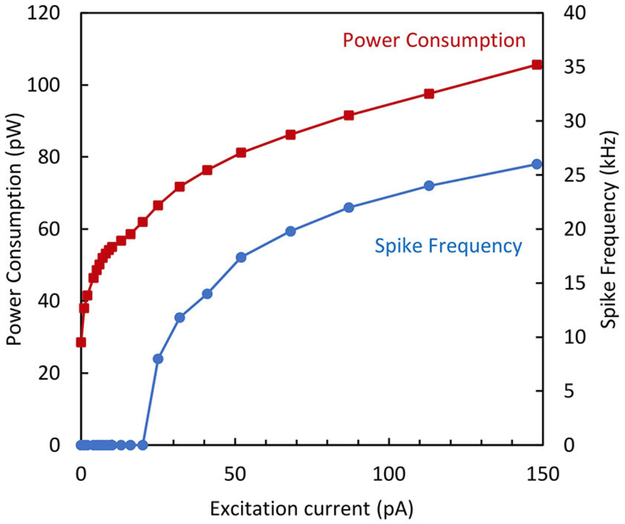

Figure 3.29 Spike frequency and power consumption vs. excitation current for the fast neuron.

As already discussed, the main objective of this work was to minimize the energy dissipation: the circuit simulation predicted a value in the fJ/spike range. The energy efficiency was determined from measurements of the total dissipated power along with the spike frequency. The energy efficiency of the fast neuron is illustrated as a function of the excitation current in **Figure 3.30**.

© 2018 Tous droits réservés.

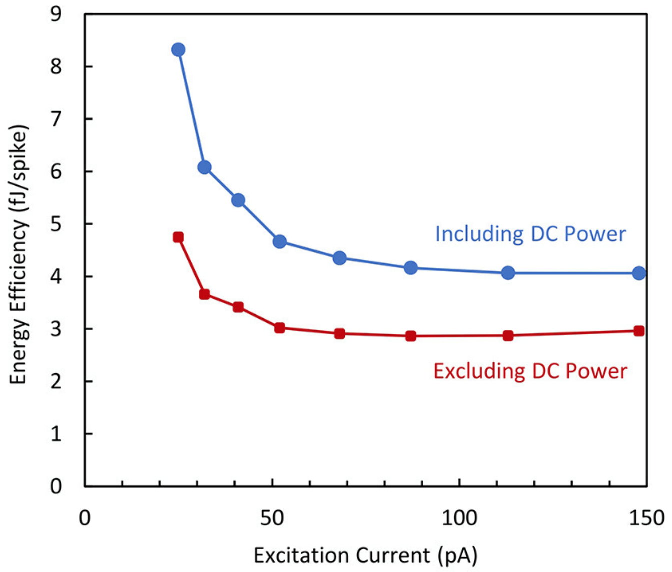

Figure 3.30 Energy efficiency vs. excitation current measured for the fast neuron.

The curves demonstrate that the energy efficiency does not significantly depend on the output spiking frequency and the experimental dissipation reaches values as low as 3fJ/spike when only the dynamic power is considered.

© 2018 Tous droits réservés.

3.7 Introduction to GreyMatter chip

The ‘GreyMatter’ chip has been fabricated in TSMC 65nm technology in order to enable a precise characterization of the elementary circuits of the artificial neurons. As shown in **Figure 3.31**, it contains various elementary circuits: inverters with different widths, buffer of biomimetic neuron, buffer of fast neuron, a standalone biomimetic neuron and fast neuron without ESD protection. The artificial neuron without ESD protection allows the accurate estimation of the current induced into the circuit. In this case, unlike the WetWire chip, we have a direct access to the exact value of the excitation current. For the WetWire chip, we had to de-embed the value of the induced current due to the diodes protections in order to estimate the exact value of the excitatory current. We have used the GreyMatter's biomimetic and fast neuron to perform a noise analysis, which will be presented in chapter 4. In this section, we will present the buffer characterization, which will allow us to characterize the artificial neurons in chapter 4.

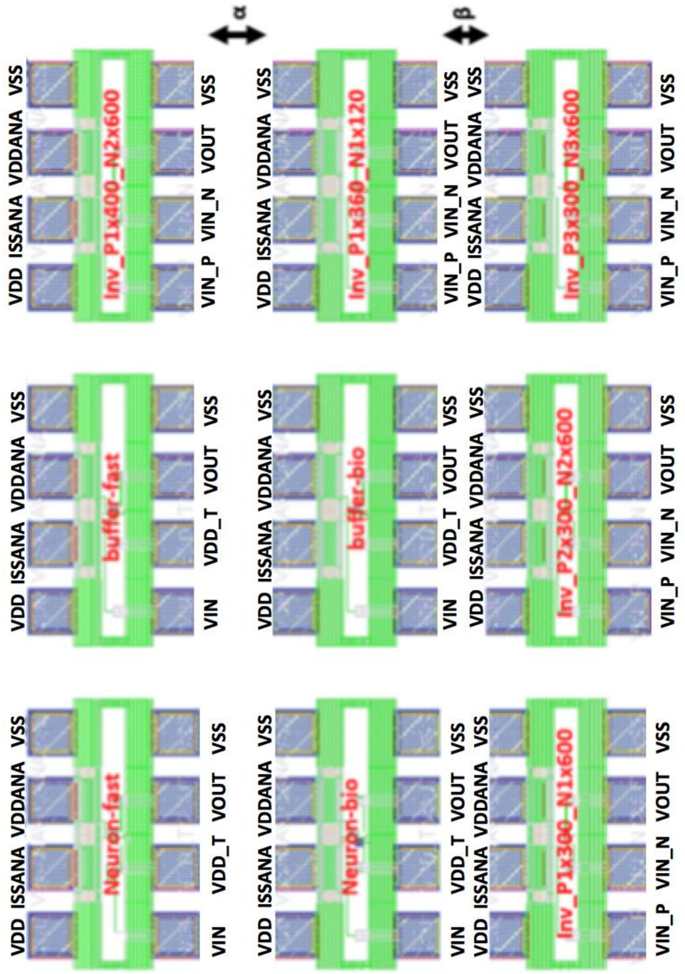

Figure 3.31 ‘GreyMatter’ chip with 9 circuits.

© 2018 Tous droits réservés.

In order to determine the correct biasing of the biomimetic and fast neuron buffer, we varied the input of the buffer (VIN) from 0 to 200mV with a step of 50mV and extracted the mean value of the output of the buffer (VOUT). This analyze has been performed for various values of VDDANA and ISSANA (see **Figure 3.32**).

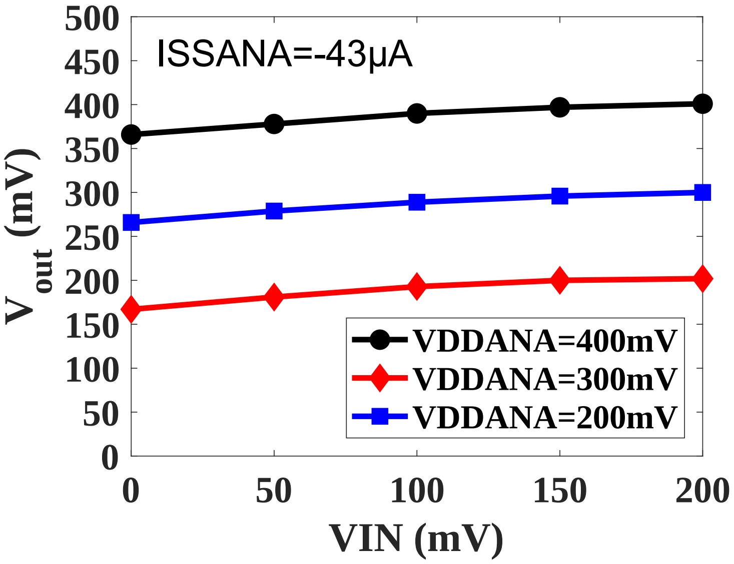

Figure 3.32 Biomimetic buffer output for various biasing.
The black line is obtained with VDDANA = 400mV, ISSANA = -43µA.The blue line is obtained with VDDANA = 300mV, ISSANA = -43µA. The red line is obtained with VDDANA = 200mV, ISSANA = -43µA.

In both cases, we had to adjust the biasing of the buffer in order to achieve the output gain of one. Based on this method we have reported in **Table 3.8** the new bias values for the GreyMatter buffers and compare it to the WetWire buffer.

Buffer	**Biomimetic neuron**		**Fast neuron**	
Biasing	**VDDANA**	**ISSANA**	**VDDANA**	**ISSANA**
WetWire chip	300mV	-43µA	300mV	-400µA
GreyMatter chip	610mV	-58µA	560mV	-560µA

Table 3.8 Comparison of buffer biases of 'WetWire' and 'GreyMatter'

These values are important to obtain the right spike amplitude of the biomimetic and fast neuron of the 'Wet Wire' and 'Grey Matter' chip.

In order to estimate the variability of the sub-threshold transistors in 65nm technology, we have considered different test benches to characterize the inverters and their corresponding NMOS and PMOS transistors individually. We have observed around 50% variability for the NMOS transistor and the PMOS transistors. The further

© 2018 Tous droits réservés.

investigation of this point was out of the scope of this thesis and we will not detail this point.

© 2018 Tous droits réservés.

3.8 Conclusion

In this chapter, we have presented the state-of-the-art standalone artificial neurons in order to evaluate the performance of the existing versions. We analyzed the neuronal membrane, which enables us to design and fabricate two standalone artificial neurons with state of the art performances in terms of power consumption, energy efficiency and area as reported in **Table 3.9**.

An energy efficiency (excluding the DC power) of **3fJ/spike** for the fast neuron and **40fJ/spike** for the biomimetic neuron has been extracted. An improvement of two orders of magnitude below the state of the art energy efficiency in (Cruz-Albrecht, Yung, & Srinivasa, 2012) has been achieved, associated to a silicon area decreasing by more than one order of magnitude. This is a very encouraging result in the road to diminish the power consumption of spiking neural networks.

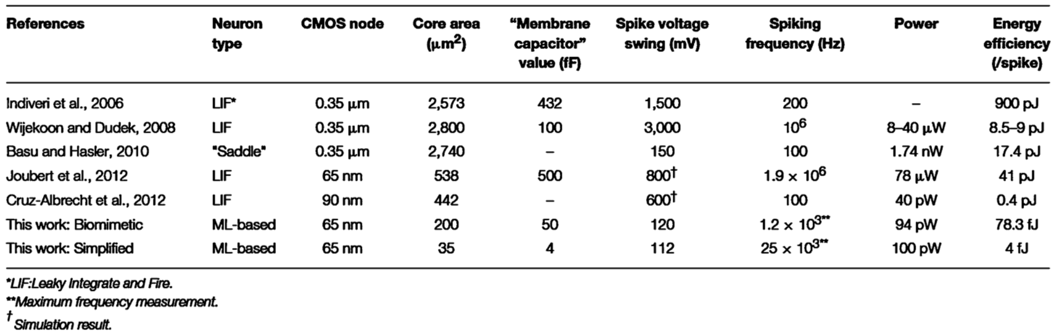

References	Neuron type	CMOS node	Core area (μm^2)	“Membrane capacitor” value (fF)	Spike voltage swing (mV)	Spiking frequency (Hz)	Power	Energy efficiency (/spike)
Indiveri et al., 2006	LIF*	0.35 μm	2,573	432	1,500	200	–	900 pJ
Wijekoon and Dudek, 2008	LIF	0.35 μm	2,800	100	3,000	10^6	8–40 μW	8.5–9 pJ
Basu and Hasler, 2010	"Saddle"	0.35 μm	2,740	–	150	100	1.74 nW	17.4 pJ
Joubert et al., 2012	LIF	65 nm	538	500	800†	1.9×10^6	78 μW	41 pJ
Cruz-Albrecht et al., 2012	LIF	90 nm	442	–	600†	100	40 pW	0.4 pJ
This work: Biomimetic	ML-based	65 nm	200	50	120	$1.2 \times 10^{3**}$	94 pW	78.3 fJ
This work: Simplified	ML-based	65 nm	35	4	112	$25 \times 10^{3**}$	100 pW	4 fJ

**LIF:Leaky Integrate and Fire.*
***Maximum frequency measurement.*
† Simulation result.

Table 3.9 State-of-the-art performances of reported stand-alone artificial neurons. The energy efficiency is presented including the DC power.

We have connected these ultra-low power artificial neurons with specific synapses and investigated the burst-spiking mode. We have characterized the WetWire and GreyMatter chips. The output spike of the biomimetic neuron was similar to the one in the biological neuron as we expected. In contrary, the frequency obtained for both neurons circuits was less than expected from cadence simulations. In fact, we expected to obtain 1MHz for the fast neuron, which wasn't achieved. The fast neuron was retro simulated in cadence and the excitatory current obtained was higher than the current obtained experimentally. This point will be investigated in future work by studying the sub-threshold NMOS and PMOS transistors of the GreyMatter chip. We have also observed a variability of 70% for the frequency in the spiking train delivered by the fast neuron. This point will also be investigated in future work. Nevertheless, this variability can be interesting for specific spiking neural network, where a sparse system needs to be investigated. Obviously, this variability must be controlled for applications, which require a precise frequency and a uniform spiking neural network. We have also observed an increase of the experimental excitatory current due to the presence of the room light, therefore all the measurements have been performed in the dark environment to avoid this fluctuation.

© 2018 Tous droits réservés.

3.9 References

(Attwell & Laughlin, 2001) Attwell, D., & Laughlin, S. B. (2001). An Energy Budget for Signaling in the Grey Matter of the Brain. *Journal of Cerebral Blood Flow & Metabolism*, *21*(10), 1133–1145. https://doi.org/10.1097/00004647-200110000-00001.

(Basu & Hasler, 2010) Basu, A., & Hasler, P. E. (2010). Nullcline-based design of a silicon neuron. IEEE Transactions on Circuits and Systems I: Regular Papers, 57(11), 2938–2947. https://doi.org/10.1109/TCSI.2010.2048772.

(Cruz-Albrecht, Yung, & Srinivasa, 2012) Cruz-Albrecht, J. M., Yung, M. W., & Srinivasa, N. (2012). Energy-Efficient Neuron, Synapse and STDP Integrated Circuits. IEEE Transactions on Biomedical Circuits and Systems, 6(3), 246–256. https://doi.org/10.1109/TBCAS.2011.2174152.

(Joubert, Belhadj, Temam, & Heliot, 2012) Joubert, a., Belhadj, B., Temam, O., & Heliot, R. (2012). Hardware spiking neurons design: Analog or digital? *The 2012 International Joint Conference on Neural Networks (IJCNN)*, 1–5. https://doi.org/10.1109/IJCNN.2012.6252600.

(Hynna & Boahen, 2007) Hynna, K. M., and Boahen, K. (2007). Thermodynamically equivalent silicon models of voltage-dependent ion channels. *Neural Comput.* 19, 327–350. doi: 10.1162/neco.2007.19.2.327

(Indiveri et al., 2011) Indiveri, G., Linares-Barranco, B., Hamilton, T. J., van Schaik, A., Etienne-Cummings, R., Delbruck, T., … Boahen, K. (2011). Neuromorphic silicon neuron circuits. *Frontiers in Neuroscience*, *5*(MAY), 1–23. https://doi.org/10.3389/fnins.2011.00073.

(Indiveri et al., 2006) Indiveri, G., Chicca, E., & Douglas, R. (2006). A VLSI Array of Low-Power Spiking Neurons and Bistable Synapses With Spike-Timing Dependent Plasticity. IEEE Transactions on Neural Networks, 17(1), 211–221. https://doi.org/10.1109/TNN.2005.860850.

(La Barbera et al., 2015) La Barbera, S., Vuillaume, D., & Alibart, F. (2015). Filamentary switching: Synaptic plasticity through device volatility. ACS Nano, 9(1), 941–949. https://doi.org/10.1021/nn506735m.

(Mead, 1989) Mead, C. (1989). Analog VLSI and Neural Systems. Reading,MA: Addison-Wesley.

© 2018 Tous droits réservés.

(Misra & Saha, 2010) Misra, J., & Saha, I. (2010). Artificial neural networks in hardware: A survey of two decades of progress. *Neurocomputing*, *74*(1–3), 239–255. https://doi.org/10.1016/j.neucom.2010.03.021

(Torrejon et al., 2017) Torrejon, J., Riou, M., Araujo, F. A., Tsunegi, S., Khalsa, G., Querlioz, D., … Grollier, J. (2017). Neuromorphic computing with nanoscale spintronic oscillators. Nature, 547(7664), 428–431. https://doi.org/10.1038/nature23011.

(Farquhar & Hasler, 2005) Farquhar, E., & Hasler, P. (2005). A bio-physically inspired silicon neuron. *IEEE Transactions on Circuits and Systems I: Regular Papers*, *52*(3), 477–488. https://doi.org/10.1109/TCSI.2004.842871

(Fox et al., 2016) Fox, D., Rotstein, H. G., & Nadim, F. (2016). *Encyclopedia of Computational Neuroscience*. https://doi.org/10.1007/978-1-4614-7320-6

(Izhikevich, 2007) Izhikevich, E. M. (2007). Dynamical Systems in Neuroscience:The Geometry of Excitability and Bursting. Cambridge, MA: MIT Press.

(Lennie, 2003) Lennie, P. (2003). The cost of cortical computation. *Current Biology : CB*, *13*(6), 493–497. https://doi.org/10.1016/S0960-9822(03)00135-0

(Pantazi, Woźniak, Tuma, & Eleftheriou, 2016) Pantazi, A., Woźniak, S., Tuma, T., & Eleftheriou, E. (2016). All-memristive neuromorphic computing with level-tuned neurons. Nanotechnology, 27(35), 355205. https://doi.org/10.1088/0957-4484/27/35/355205

(Poon & Zhou, 2011) Poon, C.-S., & Zhou, K. (2011). Neuromorphic silicon neurons and large-scale neural networks: challenges and opportunities. *Frontiers in Neuroscience*, *5*, 108. https://doi.org/10.3389/fnins.2011.00108

(Rasche & Douglas, 2000) Rasche, C., & Douglas, R. (2000). An Improved Silicon Neuron. *Analog Integrated Circuits and Signal Processing*, *23*(3), 227–236. https://doi.org/10.1023/A:1008357931826

(Tsugawa et al., 2017) Tsugawa, H., Takahashi, H., Nakamura, R., Umebayashi, T., Ogita, T., Okano, H., … Nomoto, T. (2017). Pixel/DRAM/logic 3-layer stacked CMOS image sensor technology. In 2017 IEEE International Electron Devices Meeting (IEDM) (p. 3.2.1-3.2.4). IEEE. https://doi.org/10.1109/IEDM.2017.8268317

(Yang et al, 2013) Yang, J. J., Strukov, D. B., & Stewart, D. R. (2013). Memristive devices for computing. *Nature Nanotechnology*, *8*(1), 13–24.

© 2018 Tous droits réservés.

https://doi.org/10.1038/nnano.2012.240

(Wijekoon & Dudek, 2008) Wijekoon, J. H. B., & Dudek, P. (2008). Compact silicon neuron circuit with spiking and bursting behavior. Neural Networks, 21(2–3), 524–534. https://doi.org/10

© 2018 Tous droits réservés.

lilliad.univ-lille.fr

Thèse de Sara Hedayat, Université de Lille, 2018

Chapter 4.

Noise in artificial neurons

© 2018 Tous droits réservés.

lilliad.univ-lille.fr

© 2018 Tous droits réservés.

4.1 Noise in brain

Unpredictable fluctuations and disturbances that are not part of a signal, called noise, are present in the brain. It is known that the brain is a noisy environment with different sources of noise. In fact, stochastic behavior is observed at different stages in the nervous systems (see **Figure 4.1**) (Faisal, Selen, & Wolpert, 2008). Bottom stages such as voltage-gated ion channels and neurotransmitter release mechanisms (see **Figure 4.1.b**) as well as top stages like motor neurons, where noise impacts the entire neuron response (see **Figure 4.1.c**), constitute these different stages. This noisy activity of neurons introduces some stochastic properties of the brain information processing. This stochastic behavior impacts many aspects of brain function, including probabilistic decision-making, perception, memory recall, short-term memory, attention, and even creativity (Rolls & Deco, 2010).

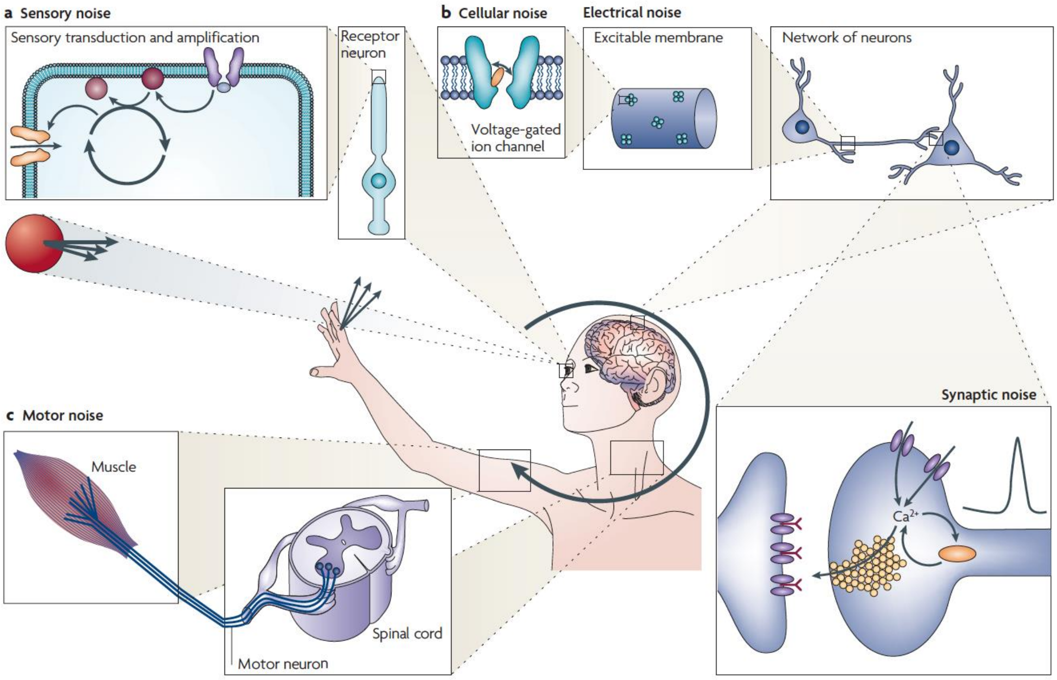

Figure 4.1 Overview of the behavioral loop and the stages at which noise is present in the nervous system.
a. Sources of sensory noise include the transduction of signals. This is exemplified here by a photoreceptor and its signal amplification cascade. **b.** Sources of cellular noise include the ion channels of excitable membranes, synaptic transmission and network interactions. **c.** Sources of motor noise include motor neurons and muscle. In the behavioral task shown (catching a ball), the nervous system has to act in the presence of noise in sensing, information processing and movement (Faisal, Selen, & Wolpert, 2008).

© 2018 Tous droits réservés.

For instance, in 2015, Stanford neuroscientists revealed that noisy neurons are critical for learning (Engel, Chaisangmongkon, Freedman, & Wang, 2015). Based on these findings, it is obvious that noise plays an important role in the brain function.

Hence, in this chapter, the impact of the noise on the artificial neuron response will be investigated. First, the membrane voltage fluctuations of the biomimetic and fast neuron will be studied. Second, the response of the biomimetic neuron to an excitatory synaptic noise will be analyzed. Finally, the stochastic resonance phenomena within the biomimetic neuron will be investigated.

© 2018 Tous droits réservés.

4.2 Membrane voltage fluctuations of the artificial neurons

4.2.1 Noise and membrane voltage fluctuations

Noise in neurons causes membrane voltage fluctuations (MVF) even in the absence of synaptic inputs. The most dominant source of such noise is channel noise (Faisal, Selen, & Wolpert, 2008). Channel noise is defined as the thermodynamic fluctuations in the gating channel ions which produce probabilistic gating behavior (Faisal, White, & Laughlin, 2005). In this section, the membrane voltage fluctuations of the artificial neuron at resting state (when the neuron does not spike) will be presented. This phenomenon has been widely investigated in biological neurons (Destexhe, Rudolph, Fellous, & Sejnowski, 2001) (Richardson, 2004). A standard deviation (SD) of 4mV has been observed for the MVF of the biological neuron (Destexhe, Rudolph, Fellous, & Sejnowski, 2001).

The aim of this study is to compare the artificial neuron and the biological neuron in terms of membrane voltage fluctuations. Another objective is to show that the artificial neuron source of noise in the resting state is mainly thermal. Hence, assuming an equivalent circuit of the neuron composed by a conductance in parallel with a capacitance, the standard deviation of the membrane voltage fluctuations, SD, will be simply given by:

$$SD = \sqrt{\frac{KT}{C_m}} \qquad \text{Eq.4.1}$$

In this expression, SD is the RMS noise voltage while K, T and C_m are the Boltzmann constant ($K = 1.38\ 10^{-23} J.K^{-1}$), the room temperature ($T = 300K$) and the membrane capacitance respectively. Based on Eq.4.1, we calculated the thermal noise standard deviation for the biological neuron, artificial biomimetic and artificial fast neuron (see **Table4.1**).

© 2018 Tous droits réservés.

Neuron	**C_m**	**SD**
Biological neuron	100pF	6.43µV
Artificial biomimetic neuron	50fF	0.27mV
Artificial fast neuron	4fF	1.01mV

Table 4.1: Membrane capacitance and the theoretical standard deviation of biomimetic and fast neuron.

The thermal noise in the biological neuron with a 100pF membrane capacitance is less than 10µV, which is much lower than the voltage fluctuations measured on biological neurons. Studies have shown that the membrane voltage noise in the case of cultured neuronal cells is about 0.1mV (Diba, 2004). In this case, only few synapses are connected to the neuron, and this noise could be referred to as the intrinsic noise of the cell. If a higher number of synapses are connected to the cell, the total neuron noise is estimated to be around few millivolts (4mV) as reported by (Destexhe, Rudolph, Fellous, & Sejnowski, 2001) where the number of synaptic connections of one neuron is around 10^4.

These experimental data show that (i) the membrane voltage noise in biological neurons is very high as compared with fluctuations due to thermal noise, and (ii) a significant part of the membrane voltage noise in living neurons is due to the synaptic noise, that is to say the noise generated by the synaptic activity.

4.2.2 Artificial neuron membrane voltage fluctuations test bench

The artificial neuron of the WetWire chip and the artificial neuron of GreyMatter chip contains 8 pads (see **Figure 4.2.up**). As shown in the schematic (see **Figure 4.2.down**) the artificial neuron is biased via VDD and VSS, the excitation PMOS transistor is biased via VDD_T, VIN and the buffer is biased via VDDANA, ISSANA and VSS. The membrane voltage VOUT is observed at the buffet output.

© 2018 Tous droits réservés.

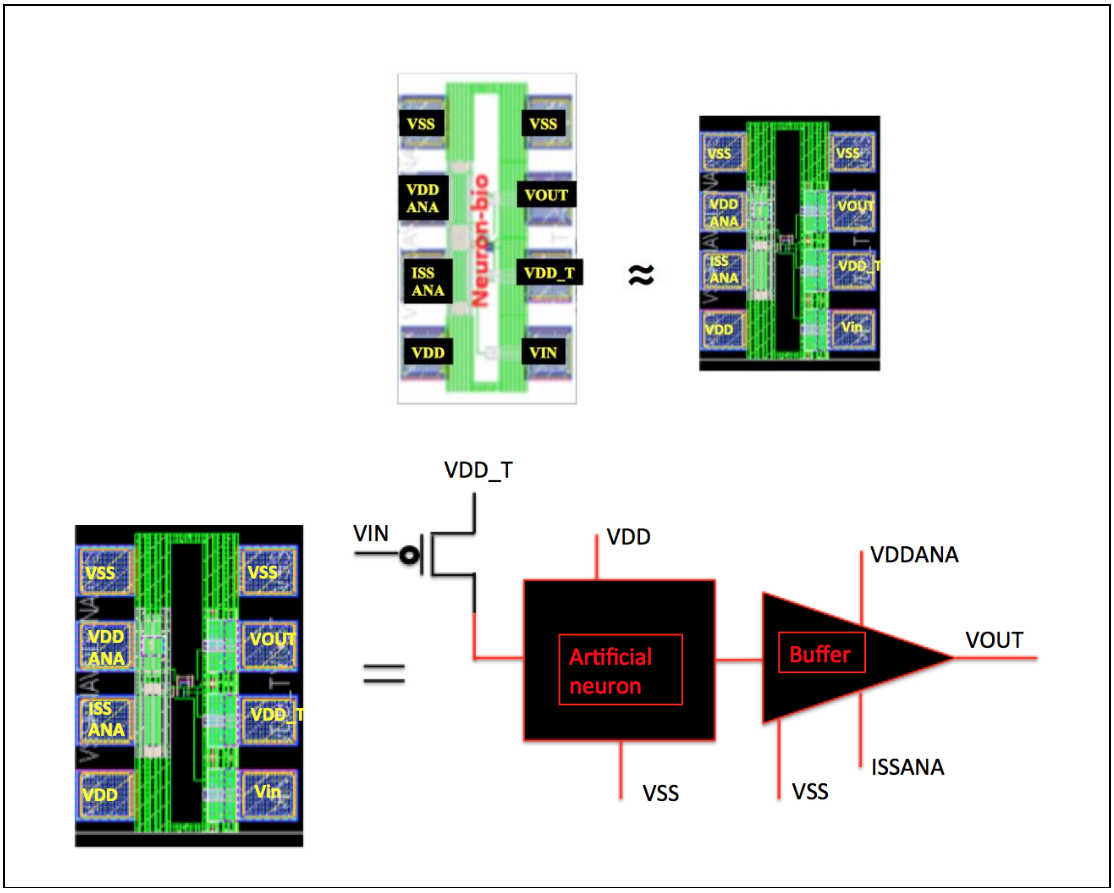

Figure 4.2 Artificial neurons circuits and schematic.

Figure 4.2.up: The artificial neuron of GreyMatter chip (left) and WetWire chip (right).

Figure 4.2.down: The biomimetic neuron pads (left) and its schematic (right).

The test bench of the membrane voltage fluctuations is illustrated in **Figure 4.3**. A Keithley 4200-scs is connected to VDD, VDDANA, ISSANA and VSS. Two Keysight 33500B are connected to VIN and VDD_T, respectively. The output of neuron was connected to both ROHDE & SCHWARZ oscilloscope 500MHZ-5GSa/s and a National Instrument chassis (NI PXIe-1073).

© 2018 Tous droits réservés.

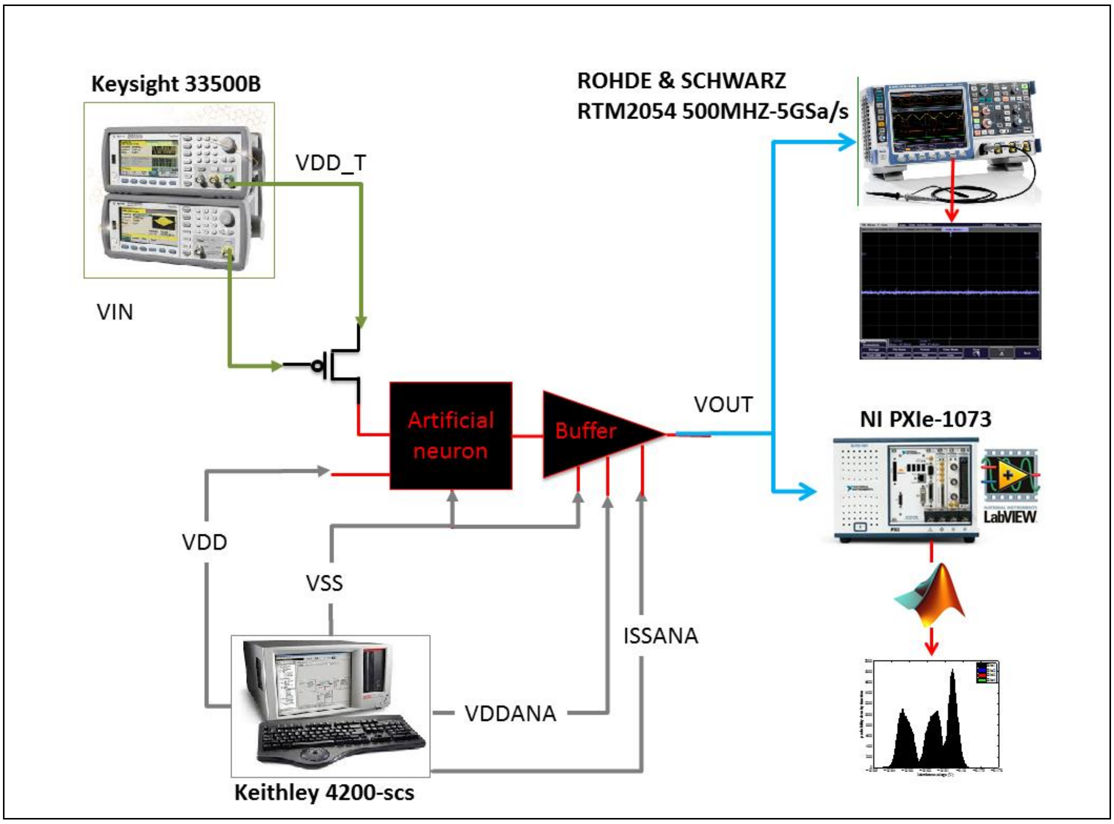

Figure 4.3 Test bench of the membrane voltage fluctuations.

The NI through the LabVIEW software enables us to acquire data in a variable period of time. This point will be detailed in the next section concerning the synaptic noise analysis where the acquisition time becomes a critical issue. Different Matlab codes were developed to analyze the data of the membrane voltage fluctuations.

4.2.3 Artificial neuron membrane voltage fluctuations at resting state

In this section, we will present the mean and standard deviation of the membrane voltage for the biomimetic and fast neuron at different resting states. Four cases are defined to characterize and determine specifically the membrane voltage fluctuations at resting state: disconnected neuron (case 1), disconnected trans-conductance (case 2), connected neuron (case 3) and neuron off (case 4). These different cases are also defined to experimentally investigate the influence of the buffer. In the following paragraphs, we will explain the biasing conditions used for each of these cases:

Case 1: Disconnected neuron

To obtain the disconnected neuron, the artificial neuron (biomimetic or fast) is off, by disconnecting VIN, VDD_T and VDD (VIN= VDD_T= VDD= NC). The VSS remains at 0V. The buffer is on, with VDDANA = 300mV and ISSANA = -400µA for the fast neuron and VDDANA = 300mV and ISSANA = -43µA for the biomimetic neuron. The artificial neuron does not generate any spikes, as it is not biased. For simplification, we will refer to this biasing as case 1.

© 2018 Tous droits réservés.

Case 2: Disconnected trans-conductance

As described in chapter 3, the trans-conductance is a PMOS transistor that injects an excitatory current to the artificial neuron when VIN and VDD_T are correctly biased. In this case, VIN and VDD_T are open (VIN = VDD_T = NC). The buffer is on. The remaining pads of the artificial neuron are VDD = VSS = 0V. In this case, the neuron does not generate any spikes. For simplification, we will refer to this biasing as case 2.

Case 3: Connected neuron

To obtain the connected neuron VIN and VDD_T are open (VIN = VDD_T = NC). The buffer is on. The artificial neuron is biased with VDD = 200mV and VSS = 0V. In this case, the neuron does not generate any spikes. For simplification, we will refer to this biasing as case 3.

Case 4: Neuron off

In this case, the biasing of the artificial neuron (biomimetic or fast) are VIN = VDD_T = VDD = 200mV and VSS = 0V. The buffer is set to be on. Obviously for this set up the trans-conductance is completely closed (due to VIN = VDD_T = 200mV) and the neuron does not generate any spikes. For simplification, we will refer to this biasing as case 4. The test bench and instruments used for these four cases remain the same. The test bench with the pads value in the case 4 for the biomimetic neuron is illustrated in the **Figure 4.4**.

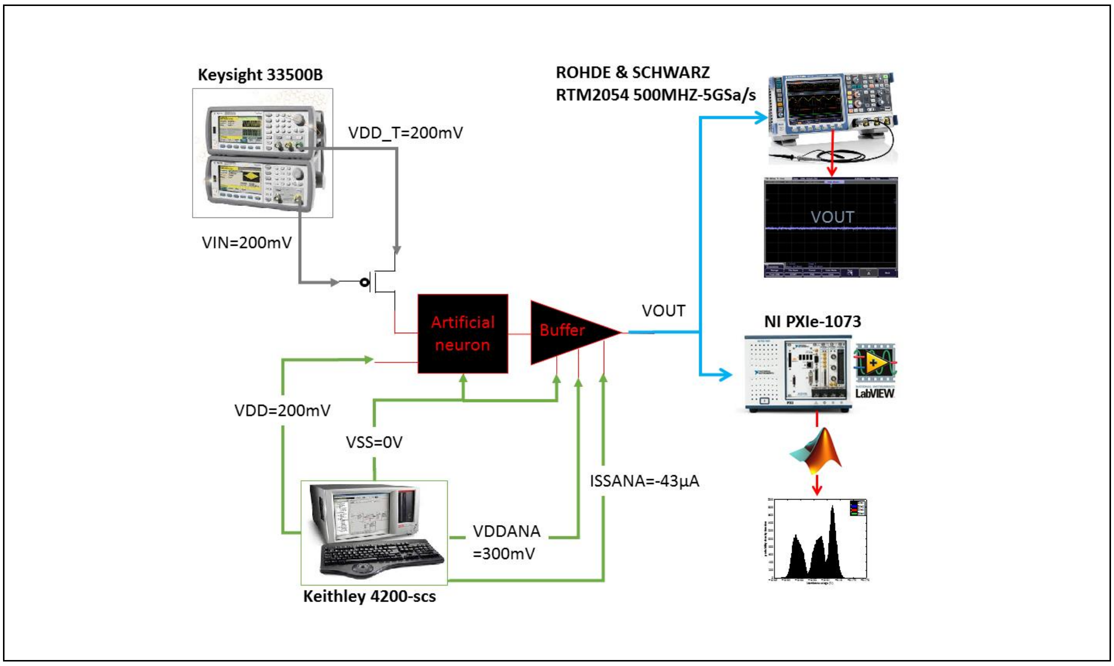

Figure 4.4 Membrane voltage fluctuations test bench in case 4 for the biomimetic neuron.

We have applied these four cases to the biomimetic neuron and extracted the probability density function (PDF) as a function of the membrane voltage (VOUT) in **Figure 4.5.**

© 2018 Tous droits réservés.

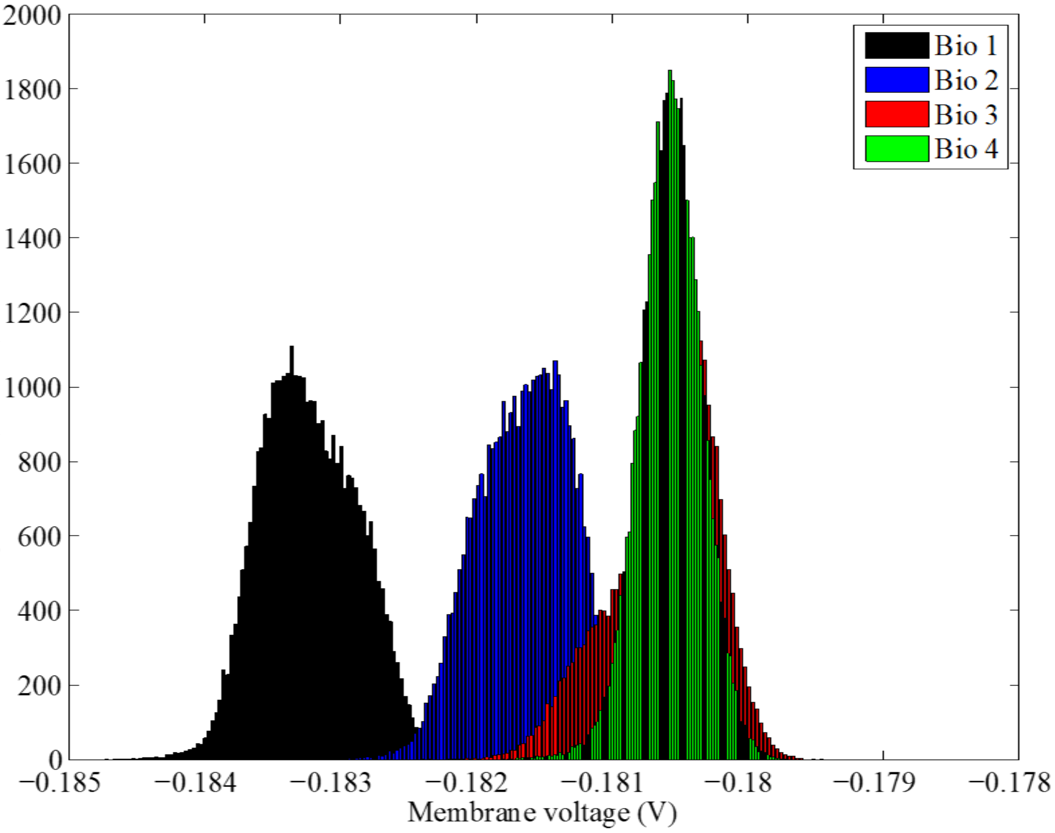

Figure 4.5 Probability density function of the biomimetic neuron at different resting states. Bio 1, Bio 2, Bio 3 and Bio 4 correspond to the respective case 1, case 2, case 3 and case 4 biasing.

The corresponding mean and standard deviation for each case of the biomimetic neuron are extracted from the PDF and are presented in **Table 4.2**.

The membrane voltage mean value varies from -183mV in the case 1, when only the buffer is on, to -180mV in the case 4, where the neuron is biased without any excitation current. The standard deviation varies from 0.36mV in the case 1 to 0.23mV in the case 4. As we compare these experimental values to the theoretical standard deviation value (0.27mV for the biomimetic neuron presented in **Table 4.1**), we can conclude that as expected (see **Table 4.1**) the biomimetic membrane voltage fluctuations is mainly thermal.

© 2018 Tous droits réservés.

Case	**VIN (mV)**	**VDD (mV)**	**VDD_T (mV)**	**Mean (mV)**	**Standard Deviation (mV)**
1	NC	NC	NC	-183.2	0.36
2	NC	0	NC	-181.6	0.35
3	NC	200	NC	-180.6	0.37
4	200	200	200	-180.6	0.23

Table 4.2 The four resting state cases, mean and standard deviation of membrane voltage fluctuations for the biomimetic neuron. Not Connected (NC) corresponds to disconnected biases, in all these cases the buffer is on with VDDANA = 300mV and ISSANA = -43µA.

Additionally, the standard deviation observed in biological neuron (4mV) is higher than the one in the biomimetic neuron. Based on this experiment, we can also conclude that in the resting state the observed noise in the artificial neuron is due to the thermal noise. The impact of the buffer noise has been also investigated using the noise matrix technique. We demonstrated that the noise of the buffer is negligible compared to the noise of the artificial neuron. The same analyses have been performed for the fast neuron and results are presented in **Figure 4.6** and **Table 4.3.**

© 2018 Tous droits réservés.

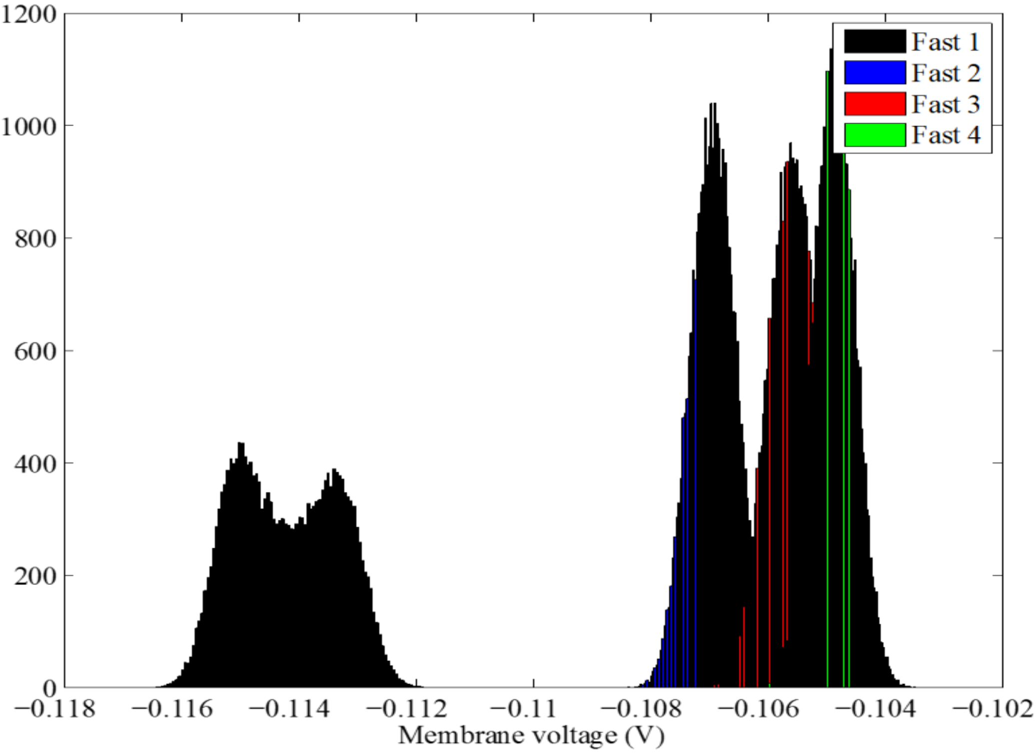

Figure 4.6 Probability density function of the fast neuron at different resting states. fast 1, fast 2, fast 3 and fast 4 corresponds to the respective case 1, case 2, case 3 and case 4 biasing.

Figure 4.6 shows the probability density function of the fast neuron for different cases. As shown in **Figure 4.6** and **Table 4.3**, the membrane voltage mean value of the fast neuron varies from -114mV in the case 1 to -105mV in the case 4. The standard deviation is around 0.4mV. This experimental standard deviation value is slightly less than the theoretical standard deviation calculated from the Eq.4.1 of 1mV.

Case	**VIN (mV)**	**VDD (mV)**	**VDD_T (mV)**	**Mean (mV)**	**Standard Deviation (mV)**
1	NC	NC	NC	-114,2	_
2	NC	0	NC	-106,9	0,39
3	NC	200	NC	-105,6	0,41
4	200	200	200	-105,6	0,41

Table 4.3 The four resting state cases, mean and standard deviation of the membrane voltage fluctuations for the fast neuron. Not Connected (NC) corresponds to disconnected biases, in all these cases the buffer is on with VDDANA = 300mV and ISSANA = -400µA.

In conclusion, for the fast neuron, the standard deviation mostly does not change for these different cases. However, the membrane voltage mean value is more impacted than the standard deviation, with 10mV variation between case 1 and case 4.

© 2018 Tous droits réservés.

The PDF of case 1, for both fast neuron and biomimetic neurons, corresponds to the minimum mean voltage value compared to other cases. The mean value increases for both neurons respectively from case 2, case 3 to case 4 where the maximum mean value of the membrane voltage is obtained.

4.2.4 Artificial neuron near threshold membrane voltage fluctuations

It is interesting to investigate the membrane voltage fluctuations of the artificial neuron near its threshold. The near threshold state is obtained by biasing the trans-conductance with VINmin, which is defined as the minimum value for VIN when the neuron does not spike. This value for the biomimetic neuron is around VINmin = 69.8mV. We have compared the probability density function for VIN = 180mV to the VINmin as illustrated in **Figure 4.7**.

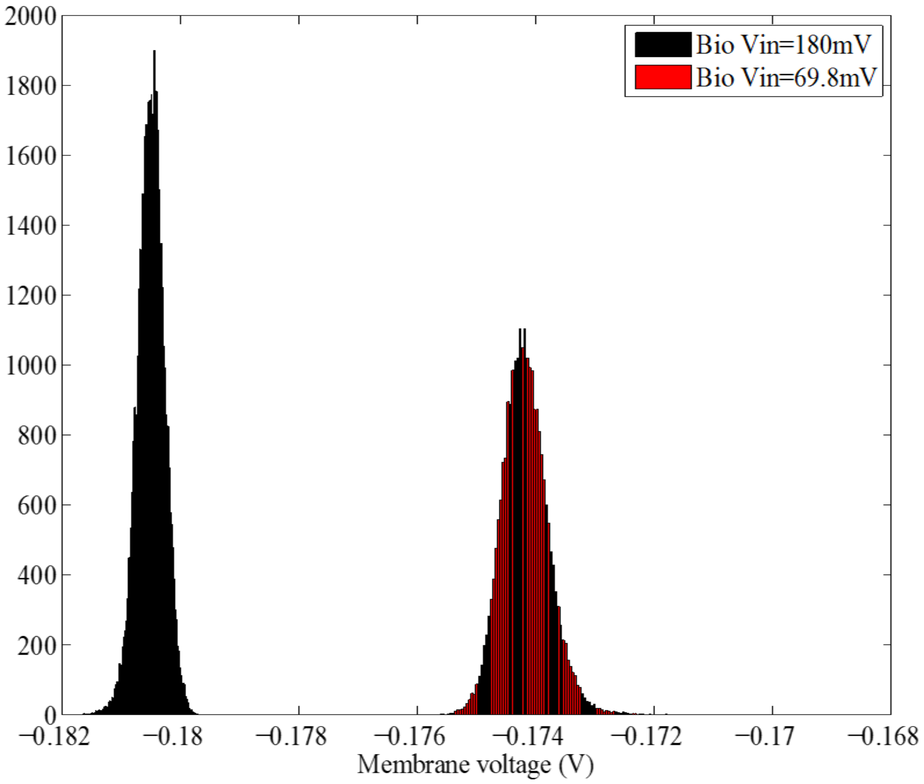

Figure 4.7 Probability density function at near threshold for biomimetic neuron.

For VIN = 180mV, we observe a mean and standard deviation of respectively -180.5mV and 0.23mV. This standard deviation corresponds to 192K in terms of temperature of noise (Eq.2.1). For VINmin = 69.8mV, both mean and standard deviation, increase to respectively -174.2mV and 0.40mV. This standard deviation corresponds to 580K in terms of temperature of noise.

© 2018 Tous droits réservés.

For the fast neuron the VINmin is 58mV, the probability density function of the fast neuron is illustrated in **Figure 4.8**.

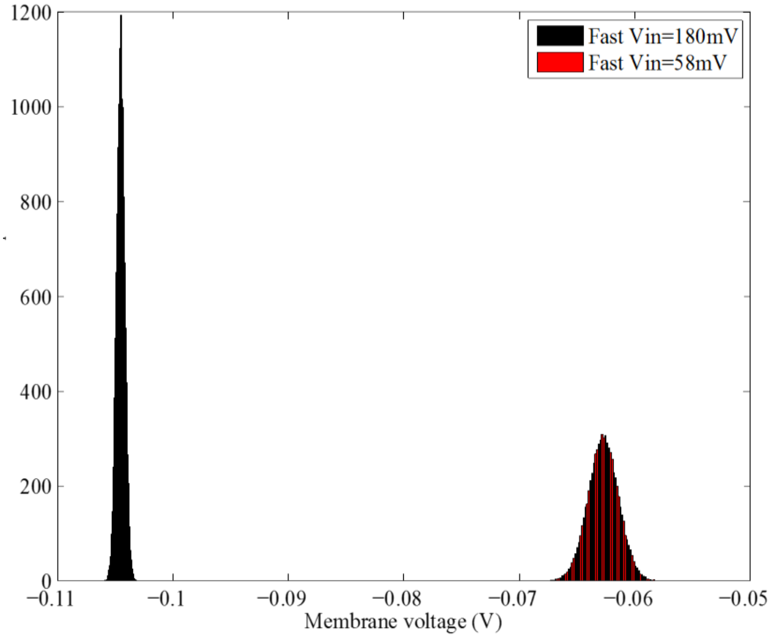

Figure 4.8 Probability density function at near threshold for fast neuron.

For VIN = 180mV, we observe a mean and standard deviation of respectively -104.5mV and 0.36mV. This standard deviation corresponds to approximately 38K in terms of temperature of noise. For VINmin = 58mV both mean and standard deviation, increase to respectively -62.7mV and 1mV. This standard deviation corresponds to approximately 252K in terms of temperature of noise. In this case, the standard deviation of the fast neuron corresponds to the value of 1mV obtained by the theory.
These experiments demonstrate that as both biomimetic and fast neuron approach their threshold, their mean and standard deviation increases. However, the low noise temperature obtained in the case of the fast neuron remains obscure: the uncertainty of the capacitance value and the validity of a simple C-G circuit for such a complicated circuit could be investigated for a deeper analysis of these results.

4.3 Synaptic noise in artificial neuron

In the brain, neurons are subjected to an intense synaptic bombardment (Destexhe, Rudolph, & Paré, 2003). The synaptic noise is composed of many uncorrelated Poisson pulse trains and some correlated ones. Based on the central limit theorem (CLT), which establishes that in most situations when independent random variables are added their properly normalized sum tends toward a normal distribution, we can assume that the sum of injected noise to a neuron cell is equivalent to a Gaussian voltage noise.

© 2018 Tous droits réservés.

To investigate this effect on our artificial neuron, this synaptic noise was reproduced by adding a Gaussian noise on the excitatory synapse. As explain in Chapter 3, the excitatory synapse of the artificial neuron is the PMOS trans-conductance. The Gaussian noise is applied on the gate of PMOS. Due to the non-linearity of the trans-conductance (sub-threshold mode), the drain-source noise current (I(t)) is composed of a DC and variable part as follows:

$$I(t) = I_0 + \sigma_I B(t) \qquad \text{Eq.4.2}$$

where σ_I is the standard deviation and B(t) is a Gaussian process defined as follows:

$$E[B(t)] = 0 \qquad \text{Eq.4.3}$$

$$E[B(t)B(t-\tau)] = \exp\left(-\frac{\tau}{\tau_c}\right) \qquad \text{Eq.4.4}$$

$$Fc = 1\,/\,(2\pi.\tau_c) \qquad \text{Eq.4.5}$$

where Fc is the cutoff frequency of the Gaussian noise source. This cutoff frequency was chosen (Fc = 100kHz) to be larger than the neuron cutoff frequency (Fn = 2kHz), hence the Gaussian noise is approximately a white noise.

This noise current (I(t)) is then integrated by the membrane capacitance of the artificial neuron as follows:

$$V(t) = \frac{1}{C}\int_0^t I(t)dt = \frac{1}{C}(I_0 t + \sigma_I W(t)) \qquad \text{Eq.4.6}$$

where W(t) is the standard Wiener process that is defined as follows:

$$W(t) = \int_0^t B(t)dt \qquad \text{Eq.4.7}$$

In fact, V(t) can be considered as a Brownian motion with drift and therefore:

$$\mu_v = E[V(t)] = I_0 t \qquad \text{Eq.4.8}$$

$$\sigma_v = var(V(t)) = \frac{2\sigma_I^2 \tau_c t}{C^2} \qquad \text{Eq.4.9}$$

© 2018 Tous droits réservés.

Let T_{th} be the first time V (t) reaches the spike threshold value V_{th}, then:

$$T_{th} = \inf\{t|V(t) = V_{th}\} \qquad \text{Eq.4.10}$$

It can be shown (Capasso, 2011) that the hitting time T_{th} follows the inverse Gaussian distribution hence:

$$T_{th} \sim IG(\frac{C_{V_{th}}}{I_0}, \frac{C^2 V_{th}^2}{2\sigma_I^2 \tau_c})\} \qquad \text{Eq.4.11}$$

In this chapter, the membrane voltage and the inter spike interval (ISI) distributions of the artificial neuron under a Gaussian noise excitation will be investigated.

4.3.1 Input noise characterization

We have characterized the generated noise from the Keysight 33500B to validate its Gaussian nature. In fact, the Keysight will be used as the source of the noise and it is necessary to verify the nature of its generated noise signal.

The input noise has a bandwidth of 100kHz with an offset value of 20mV. This noise was analyzed for two acquisition times window: first, short acquisition time of 13s and second, long acquisition time of 30min. For each acquisition time two level of noise was investigated: Vin Noise = 28.40mVrms which is considered as a low level of noise for our artificial neuron and Vin Noise = 45.45mVrms considered as high level of noise. We used a sampling frequency of 200kHz in the LabVIEW program to extract the noise.

For the short acquisition, the noise was extracted during 13s over 11 trials. To investigate the effect of time on the noise, we have extracted the 11th trials one hour after the acquisition of the 10th trials. **Figure 4.9.up** and **Figure 4.9.down** shows the superimposed number of occurrences and the probability density function (PDF) of the 11 noise trials for Vin Noise = 28.40mVrms and Vin Noise = 45.45mVrms, respectively.

© 2018 Tous droits réservés.

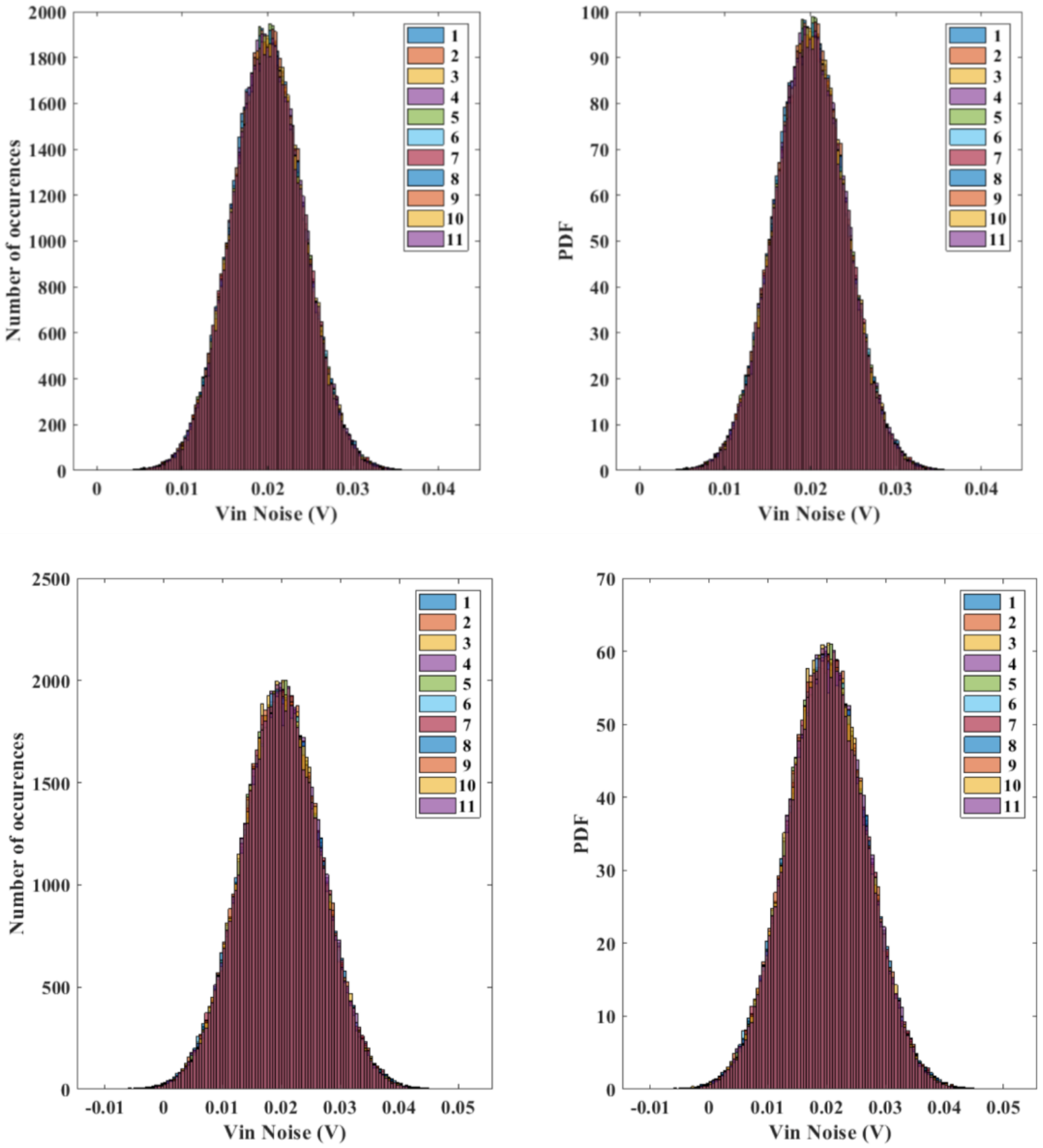

Figure 4.9 Histogram and PDF for short acquisition. Figure 4.9.up: 11 trials superimposed for Vin Noise = 28.40mVrms. **Figure 4.9.down:** 11 trials superimposed for Vin Noise = 45.45mVrms.

We calculated the half width at half maximum of each of these probability density functions. We found that it corresponds to the injected RMS value, as expected. For example, for Vin Noise = 45.45mVrms, the half maximum of the PDF (max value of PDF multiplied by $e^{-1/2}$) is about 36. Based on this value, the half width at the half maximum is about 45mVrms, which corresponds to the input noise.

We have extracted several parameters: the mean value (M), the standard deviation (SD), the variance (VAR) and the median (MED) for each trial. These parameters remain constant with same value for each trial. The mean and median are equal to 0.02V, which corresponds to the 20mV offset value, of the injected noise. The standard deviation is

© 2018 Tous droits réservés.

around 4.2mV and the variance varies around 17µV. As we increase the noise signal from 28.40mVrms to 45.45mVrms, the standard deviation increases from 4.2 mV to 6.7mV and the variance changes from 17µV to 45µV. The mean and median remain around 0.02V.

To perform the long acquisition, we have extracted 180 consecutive trials (the acquisition time of each trial is 10s) of the noise and rebuild the noise signal which has an acquisition time of 30min. **Figure 4.10.up** shows the number of occurrences and the PDF of the noise for Vin Noise = 28.40mVrms during 30min. **Figure 4.10.down** shows the number of occurrences and the PDF of the noise for Vin Noise = 45.45mVrms during 30min.

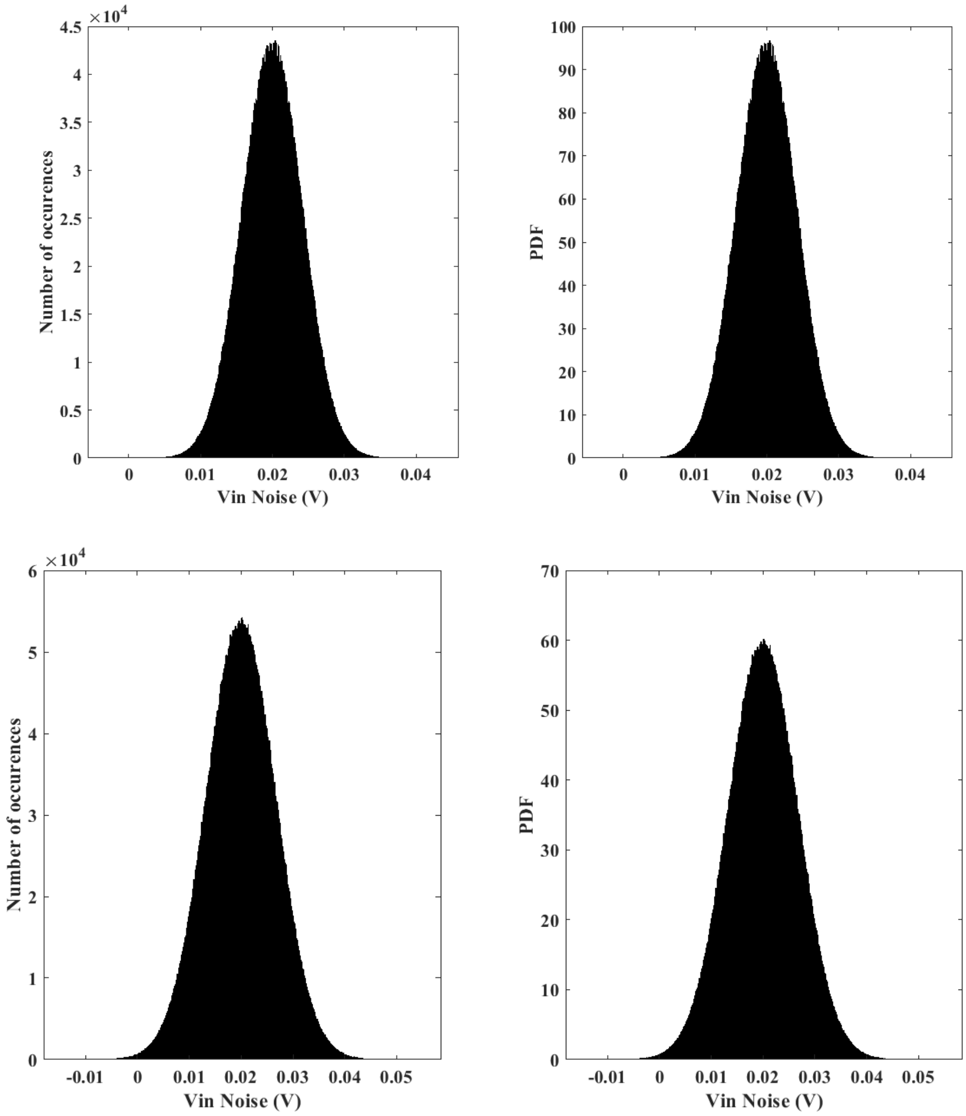

Figure 4.10 Histogram and PDF for long acquisition.
Figure 4.10.up: Vin Noise = 28.40mVrms during 30min
Figure 4.10.down: Vin Noise = 45.45mVrms during 30min

© 2018 Tous droits réservés.

Same values are obtained for the maximum value of the PDF, during 30min and 10s. The extracted noise parameters (mean, standard deviation, variance and median) of these two levels of noise also remain constant during the 30min acquisition. These parameters have the same values as the parameters obtained for the short acquisition. Based on these results, we conclude that the generated noise is a Gaussian noise.

As we compare the parameters obtained from the short acquisition to the long acquisition, we conclude that the acquisition time does not impact the input noise. This study validates that, the Gaussian noise generated from the Keysight 33500B remains uniform in time, which is an important point, as we will see in next paragraphs. In the next paragraphs, we will study the response of the artificial neuron to a synaptic noise of a Gaussian nature.

4.3.2 Biomimetic neuron DC characterization

In order to analyze experimentally the response of the artificial neuron to a synaptic noise excitation, a DC characterization was first carried out. Due to the variability observed before, we define a set of criteria to choose the best circuit for the noise analysis. The DC characterization enables us to extract parameters, which allow an accurate noise measurement. The DC characterization has been carried out for 30 biomimetic circuits present on the GreyMatter chip. Four parameters of each artificial neuron have been considered in the DC characterization as follows:

1) The maximal frequency (Fmax)
2) The membrane voltage (VOUT) when VIN = 0V
3) The peak-to-peak amplitude of the spike (mVpp)
4) The minimal value for VIN which the neuron does not generate spike (VINmin)

Based on these four parameters, we define the best circuit for a biomimetic neuron if it presents:

1) Fmax < 2kHz
2) VIN = 0V => VOUT = Vrest (the VOUT is at resting state).
3) 100mV ≤ mVpp ≤ 200mV
4) VINmin ≥10mV

Based on the DC characterization, only 10 biomimetic neurons displayed these four satisfying parameters and therefore were chosen to carry out the noise analysis.

© 2018 Tous droits réservés.

lilliad.univ-lille.fr

Thèse de Sara Hedayat, Université de Lille, 2018

4.3.3 Synaptic noise test bench

The synaptic noise test bench is composed of a Keithley 4200-scs, a Keysight 33500B, a ROHDE & SCHWARZ oscilloscope RTM2054 500MHZ-5GSa/s and a National Instrument NI PXIe-1073 (see **Figure 4.12**). The Keithley 4200-scs is connected to VDD, VDD_T, VDDANA, ISSANA and VSS. The VDD_T and VDD are equal to 200mV. The buffer is in on state with VDDANA = 610mV and ISSANA = -58µA. The VSS is set to zero (see **Figure 4.12**).

The Keysight 33500B is connected to the input of the biomimetic neuron (PMOS gate) to generate the Gaussian noise (Vin Noise). The Gaussian noise has an offset value equal to the VINmin. As explained in the previous section, the VINmin is extracted from the DC characterization.

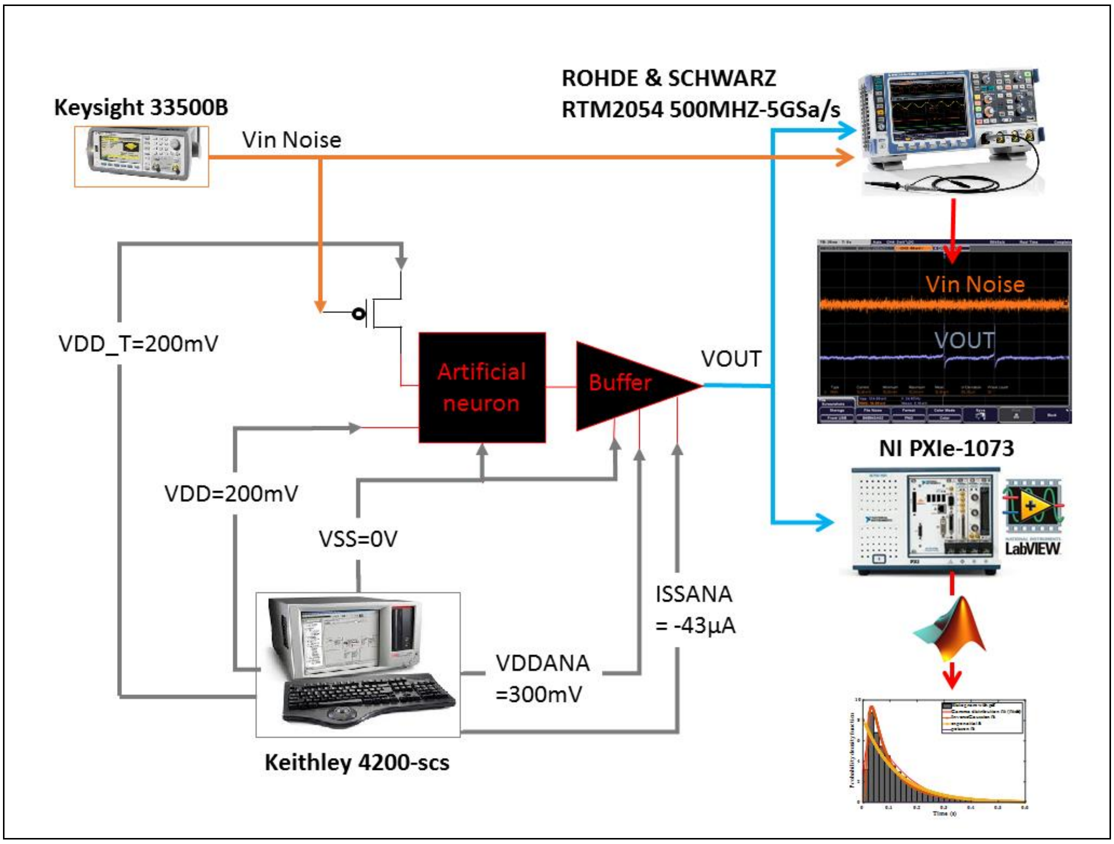

Figure 4.12 Synaptic noise test bench.

The output of neuron (VOUT) is connected to both ROHDE & SCHWARZ oscilloscope RTM2054 500MHZ-5GSa/s and a National Instrument NI PXIe-1073. The NI via the LabVIEW program enables us to acquire data's in a variable period of time. In fact, in this measurement due to the stochastic behavior of the spike train the acquisition time becomes an important factor. We have developed different LabVIEW and Matlab programs to analyze the output data of the artificial neuron excited by the Gaussian synaptic noise.

© 2018 Tous droits réservés. lilliad.univ-lille.fr

Figure 4.13 illustrates the response of the biomimetic neuron (VOUT) to the Gaussian noise (Vin Noise) during 200ms. The orange curve is the injected Gaussian noise with Vin Noise = 10mVrms and an offset value of 20mV. For this low level of noise the biomimetic neuron response is extremely variable. The generated stochastic spike shown in **Figure 4.13**, has an amplitude of VOUT = 124mVpp and a 24Hz frequency, which varies according to the acquisition time.

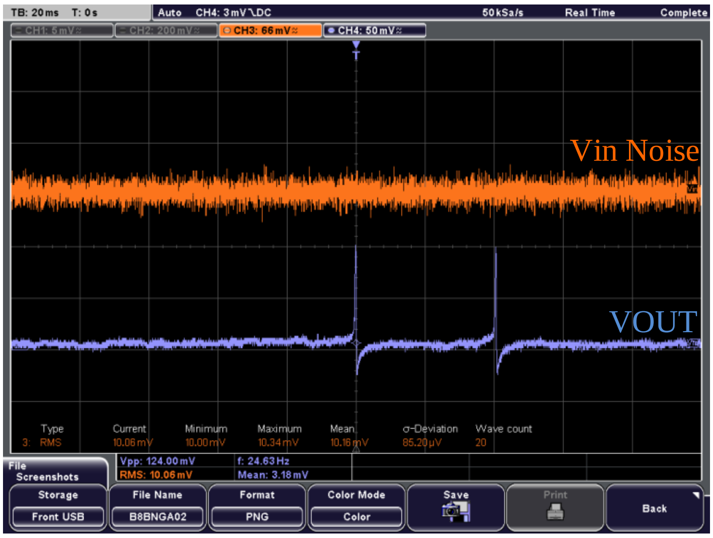
TB: 20 ms T: 0 s Auto CH4: 3 mV ⌐DC 50 kSa/s Real Time Complete

CH1: 5 mV≈ CH2: 200 mV≈ CH3: 66 mV≈ CH4: 50 mV≈

Type	Current	Minimum	Maximum	Mean	σ-Deviation	Wave count
3: RMS	10.06 mV	10.00 mV	10.34 mV	10.16 mV	85.20 µV	20

Vpp: 124.00 mV f: 24.63 Hz
RMS: 10.06 mV Mean: 3.18 mV

Storage: Front USB
File Name: B8BNGA02
Format: PNG
Color Mode: Color

Figure 4.13 Response of biomimetic neuron to the low level of Gaussian noise.

As the level of noise (Vin Noise) increases, the response of the biomimetic neuron becomes less stochastic and more periodic as shown in **Figure 4.14.**

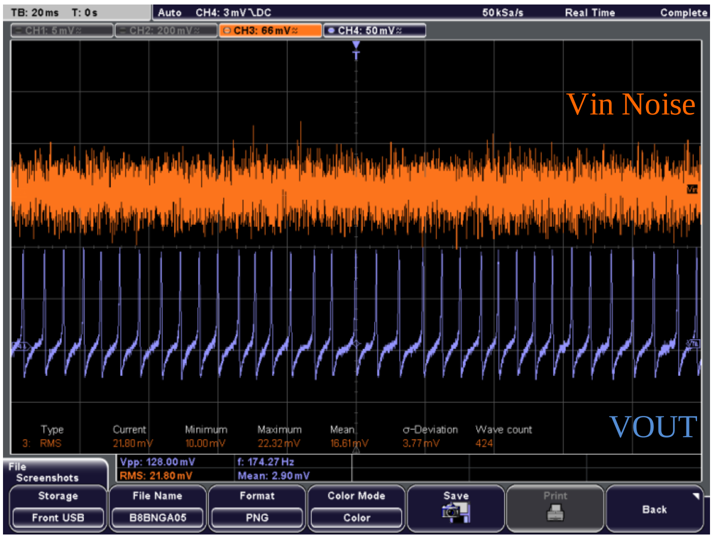
TB: 20 ms T: 0 s Auto CH4: 3 mV ⌐DC 50 kSa/s Real Time Complete

CH1: 5 mV≈ CH2: 200 mV≈ CH3: 66 mV≈ CH4: 50 mV≈

Type	Current	Minimum	Maximum	Mean	σ-Deviation	Wave count
3: RMS	21.80 mV	10.00 mV	22.32 mV	16.61 mV	3.77 mV	424

Vpp: 128.00 mV f: 174.27 Hz
RMS: 21.80 mV Mean: 2.90 mV

Storage: Front USB
File Name: B8BNGA05
Format: PNG
Color Mode: Color

Figure 4.14 Response of biomimetic neuron to the high level of Gaussian noise.

A spiking frequency of 175Hz with an amplitude of VOUT = 128mVpp is generated from the biomimetic neuron for an injected noise of Vin Noise = 22.73mVrms.

© 2018 Tous droits réservés.

For these biasing values, the noise measurement has been carried out for two different categories: short acquisition, long acquisition. The sampling rate of 5kHz that corresponds to a sampling time of 200µs is used for these categories.
The time acquisition of the membrane voltage is 13s for the short acquisition. This time increases to 30min for the long acquisition. In fact, the biomimetic neuron spike train is extremely stochastic as shown in **Figure 4.13** for low levels of injected noise. For this specific case, we have observed interspike intervals (ISI) as long as 40s. Hence, we developed a LabVIEW program to enable us to increase the time acquisition according to the observed ISI and the level of injected noise.

Several analyses have been performed for these two categories. First, the spike extraction with different time duration, using the National Instrument (NI PXIe-1073). Second, the extracted spikes are analyzed with developed Matlab codes to first detect the spike and then extract the interspike intervals known as ISI. Third, different ISI parameters such as the mean, the standard deviation and the variance are extracted. Forth, the histogram and the probability density function of the obtained ISI are plotted for different noise levels. Finally, different distribution fits such as gamma, inverse Gaussian, exponential and Poisson are investigated and compared to obtained results.

© 2018 Tous droits réservés.

4.3.4 Spike detection and ISI

For the noise analysis, we extract the membrane voltage also called spike train of the biomimetic neuron for different levels of excitatory Gaussian noise. The spike train enables us to detect the occurrence time of each spike, also called spike detection, in the spike train. **Figure 4.15.up** shows the spike train for an injected noise of 19.31mVrms and **Figure 4.15.down** shows the spike detection during 6s.

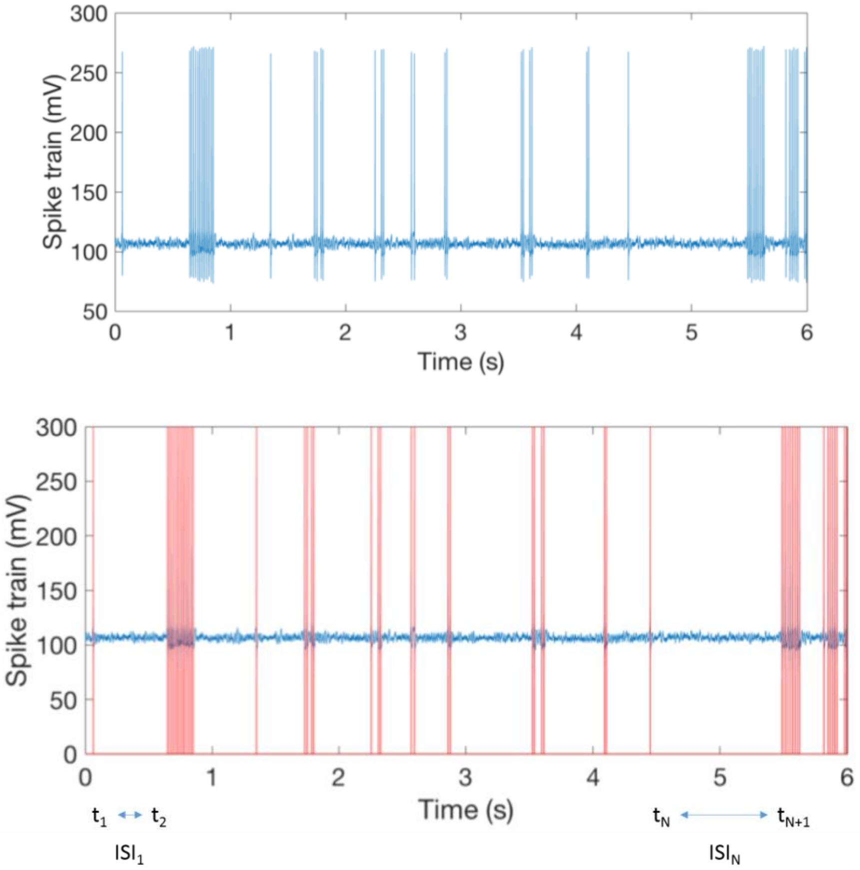

Figure 4.15 Spike train and ISI.
Figure 4.15.up: Resulting spike train for Vin Noise = 19.31mVrms.
Figure 4.15.down: Detected spikes with red lines.

The spike detection enables us to define the interspike intervals (ISIs) of one spike train. In fact, Matlab inserts a red line (**Figure 4.15.down**) for each detected spike and its occurrence time (t_i). We define the ISI_N as the consecutive subtraction (t_{N+1}-t_N) of the occurrence time of Nth spike (t_N) and Nth+1 spike (t_{N+1}). For instance, ISI_1 is resulted from the subtraction of t_2-t_1 as shown in **Figure 4.15.down.** Based on this definition, we extracted the overall ISI of one spike train. Obviously, in a spike train with 100 spikes there is 99 ISIs.

© 2018 Tous droits réservés.

4.3.5 Short acquisition

In this part, the injected Gaussian noise to the PMOS gate varies from 29.55mVrms to 51.1mVrms during 10s. As described before, we have extracted the spike train of each noise level and extracted its corresponding ISI. For each noise level, we define six parameters of the ISI as follows:

- M : is the mean value of the ISI.
- SD : is the standard deviation of ISI.
- VAR : is the variance of ISI.
- K: is the ratio of mean to standard deviation of ISI, known as the shape parameter.
- Θ : is the ratio of the mean to the shape parameter, known as the scale parameter.
- CV: is the ratio of the standard deviation to the mean value of ISI, known as the coefficient of variation.

These parameters can determine the distribution function of the ISI. For instance in a Poisson process, the coefficient of variation is CV = 1 (Pachitariu, Brody, Jun, & Holmes, n.d.).

The shape parameter K and the scale parameter Θ are used to define the gamma distribution.

We will also introduce other parameters to define the inverse Gaussian distribution in the following paragraphs.

These parameters of ISI are illustrated for each noise level in **Figure 4.16.**

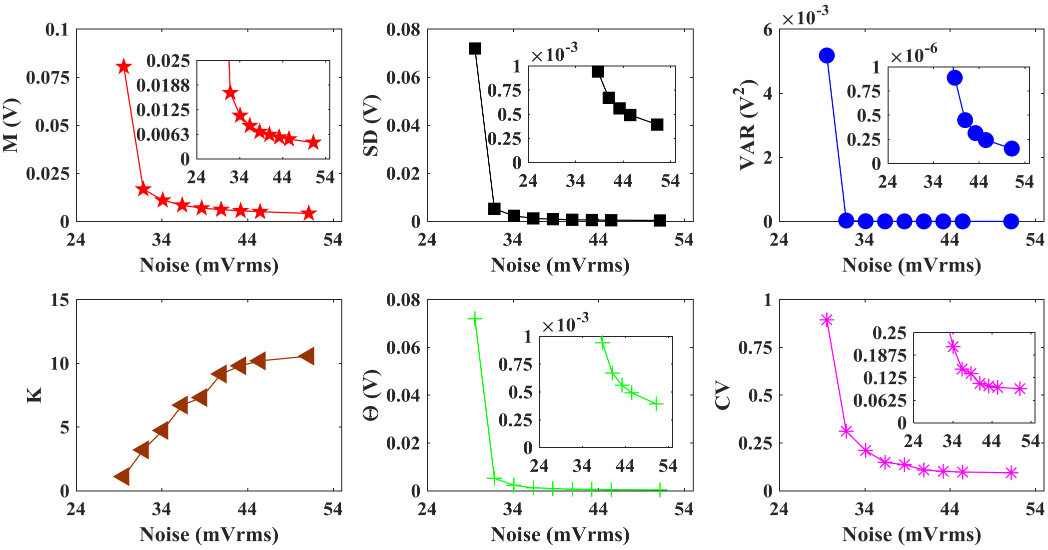

Figure 4.16 ISI parameters corresponding to the injected noise to the PMOS gate for an acquisition time =10s.

In this part, the injected Gaussian noise on the PMOS source varies from 27.27mVrms to 51.1mVrms during 10s. The ISI parameters are illustrated in **Figure 4.17.**

© 2018 Tous droits réservés.

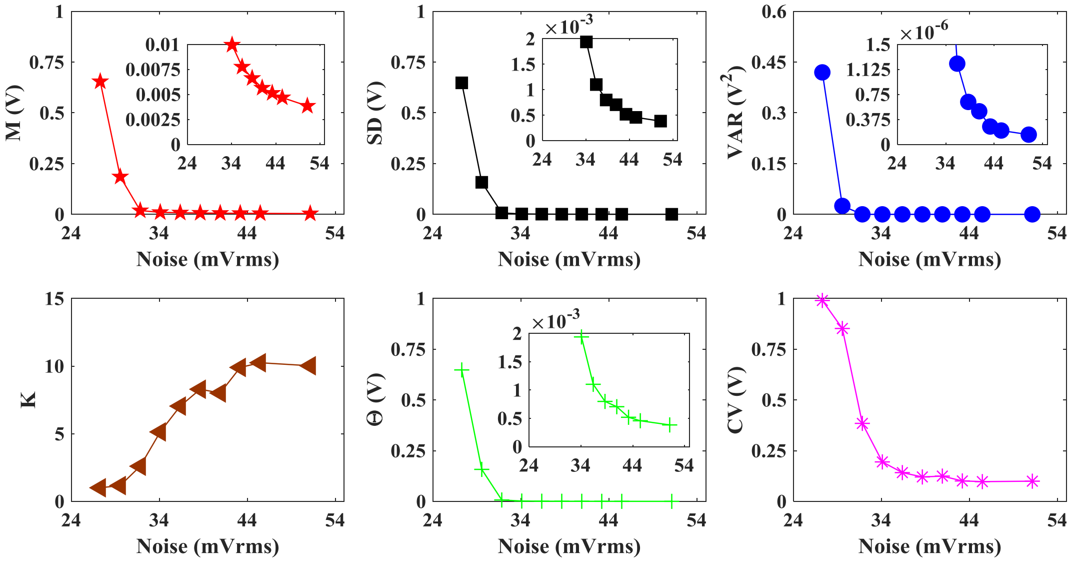

Figure 4.17 ISI parameters corresponding to the injected noise to the PMOS source for an acquisition time =10s.

The ISI parameters obtained from the injected noise on the PMOS gate and the PMOS source are similar. Hence, we will focus on the injected noise on the PMOS gate in the next paragraphs. The mean (M), standard deviation (SD), variance (VAR), scale parameter (Θ) and coefficient of variation (CV) decrease as the noise level increases. The shape parameter (K) increase as the noise levels increase, it saturates around 10 in both cases.

In this experiment, the first level of noise for both cases was 25mVrms but as shown in **Figure 4.18** (noise on PMOS gate) and **Figure 4.19** (noise on PMOS source) this level of noise is not enough to generate spikes.

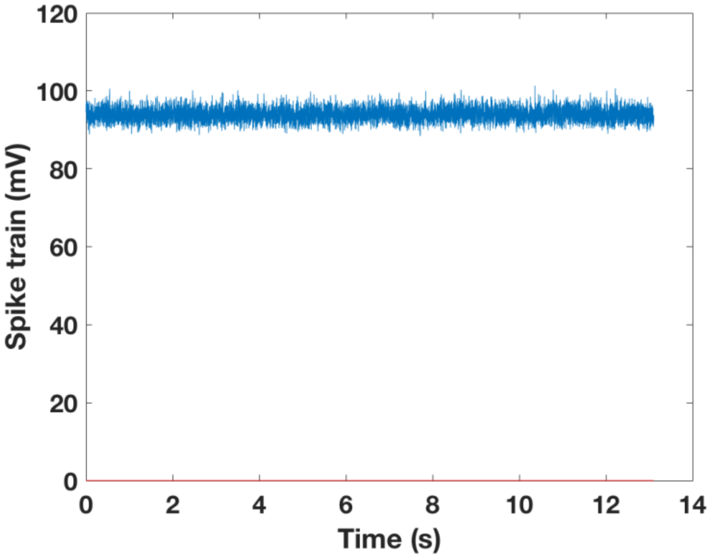

Figure 4.18 Spike train for Vin Noise = 25mVrms on PMOS gate.

© 2018 Tous droits réservés.

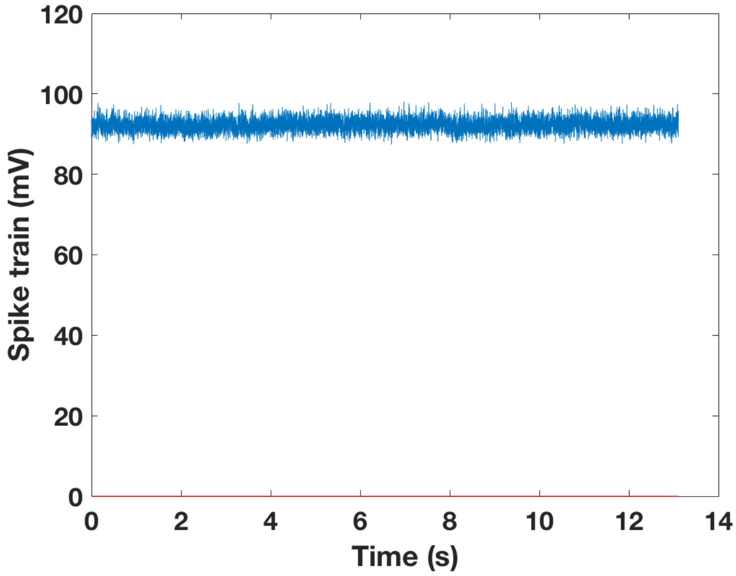

Figure 4.19 Spike train for Vin Noise = 25mVrms on PMOS source.

This value varies from circuit to circuit due to the variability of the artificial neuron. Another important point is the statistic of the spike train when the noise level is low. As it can be seen in **Figure 4.20** for an injected noise of 27.27mVrms on the PMOS gate, we obtain only 4 spikes during 13s.

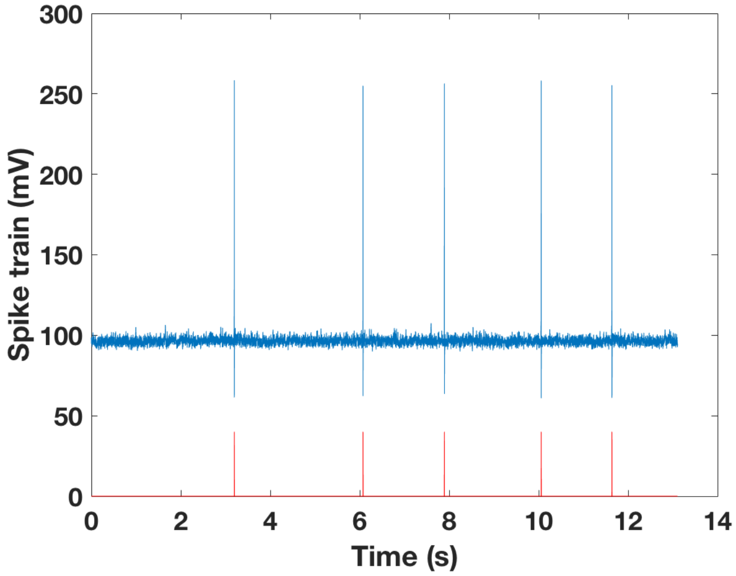

Figure 4.20 Spike train for Vin Noise = 27.27mVrms on PMOS gate.

Due to this poor statistic for this low noise level, we have developed another LabVIEW program in order to increase the acquisition time, which will be presented in the next section.

© 2018 Tous droits réservés.

4.3.6 Long acquisition

The long acquisition characterization enables us to obtain an improved statistic for the low level of noise. In order to obtain this long acquisition, we have developed a new LabVIEW program to acquire 180 consecutive spike trains of 10s. We have also developed a Matlab code in order to rebuild the totality of these 180 spike trains. **Figure 4.21.a** shows the spike train of a biomimetic neuron for high levels of noise during 120s. Each change of color corresponds to one spike train of 10s as illustrated in **Figure 4.21.a**.

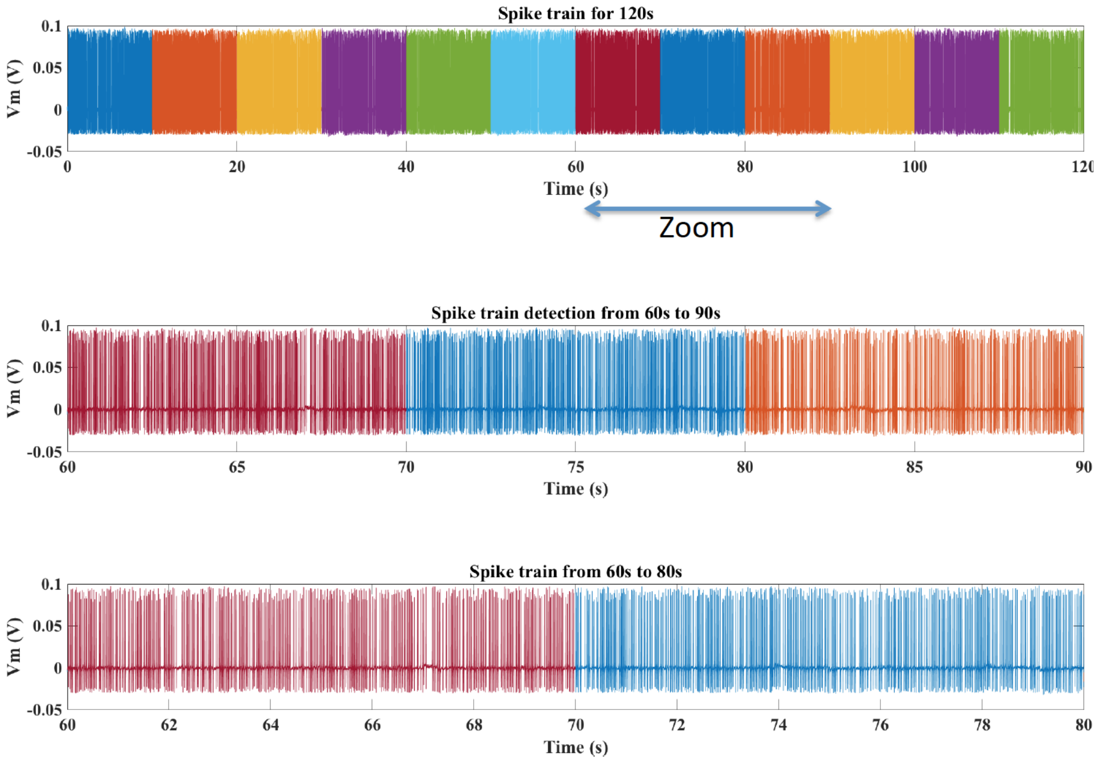

Figure 4.21.a Rebuild spike train over 120s.

Figure 4.21.b is obtained from another biomimetic neuron and shows the rebuild spike train of 180 consecutive spike trains excited by a low level of noise (Vin Noise = 27.27mVrms) during 30min.

© 2018 Tous droits réservés.

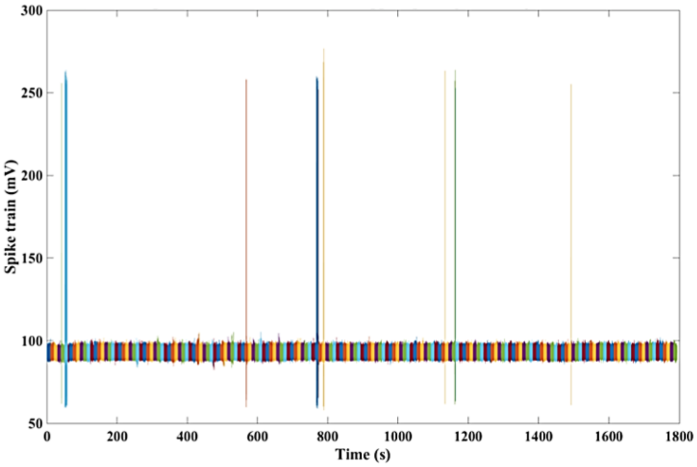

Figure 4.21.b Spike train for Vin Noise= 27.27mVrms on PMOS gate during 30min.

It is worth mentioning that the development of these programs was a key step in the experimental analyze of the noise. This achievement is fundamental in order to observe and analyze the behavior of the artificial neuron when it is excited with a low level of noise.

Using these developed tools, we have varied the level of injected noise from 27.27mVrms to 30.68mVrms by a step of 1.13mVrms on the PMOS gate of the biomimetic neuron. The rebuild spike train for each noise level is illustrated in **Figure 4.22**.

© 2018 Tous droits réservés.

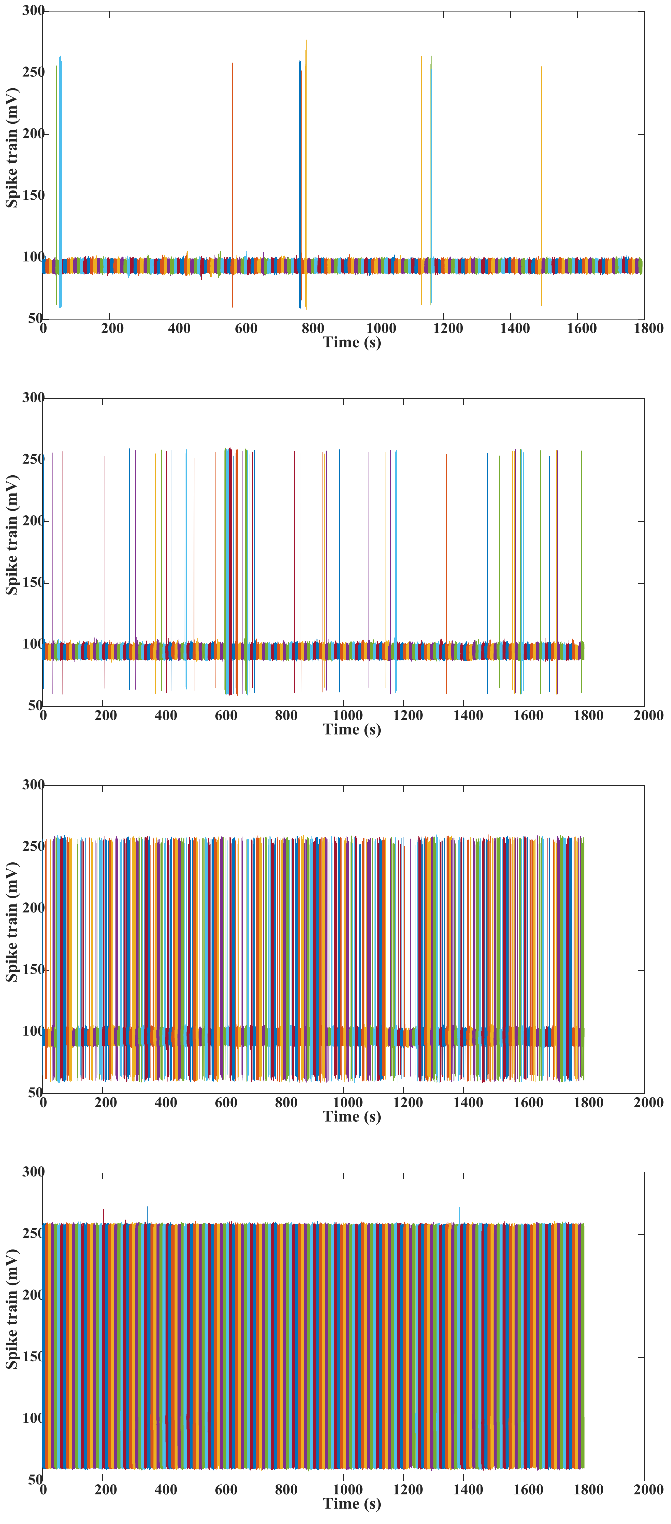

Figure 4.22 Rebuild spike train for different noise levels. The Vin noise varies from 27.27, 28.40, 29.54 to 30.68, respectively.

For each level of noise, we have reported in **Table 4.4** the number of spike, the number of ISI, the bin width and the number of bins for an acquisition time of 30min.

© 2018 Tous droits réservés.

Noise on PMOS gate (mVrms)	Number of spike	Number of ISI	Bin width (s)	Number of Bin
27.27	140	139	50	11
28.40	408	407	10	17
29.54	1094	1093	0.5	43
30.68	14 815	14 814	0.02	141

Table 4.4 Spike train data for long acquisition.

We have extracted the ISI parameters of each of these spike train as shown in **Figure 4.23.**

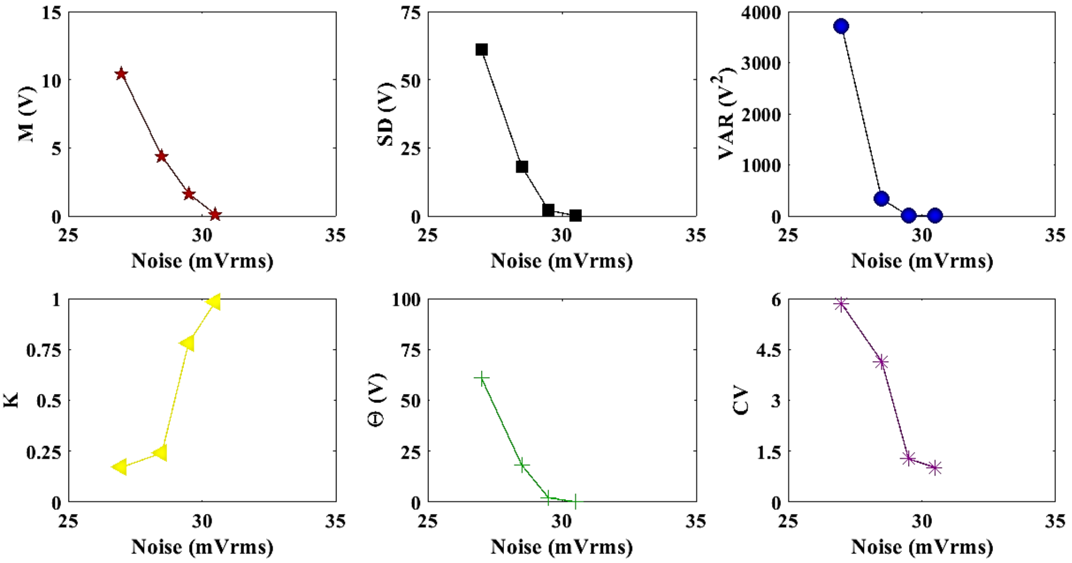

Figure 4.23 Experimental ISI parameters for different levels of noise injected to the PMOS gate during 30min.

The median, lambda (λ) and mu (μ) parameters were added and plotted as a function of noise in **Figure 4.24**. Where λ also called scale parameter is defined as follows:

$$\lambda = \frac{mean(ISI)^3}{variance\ (ISI)} \qquad \text{Eq.4.13}$$

and μ is the location parameter equal to the mean value of ISI.

© 2018 Tous droits réservés.

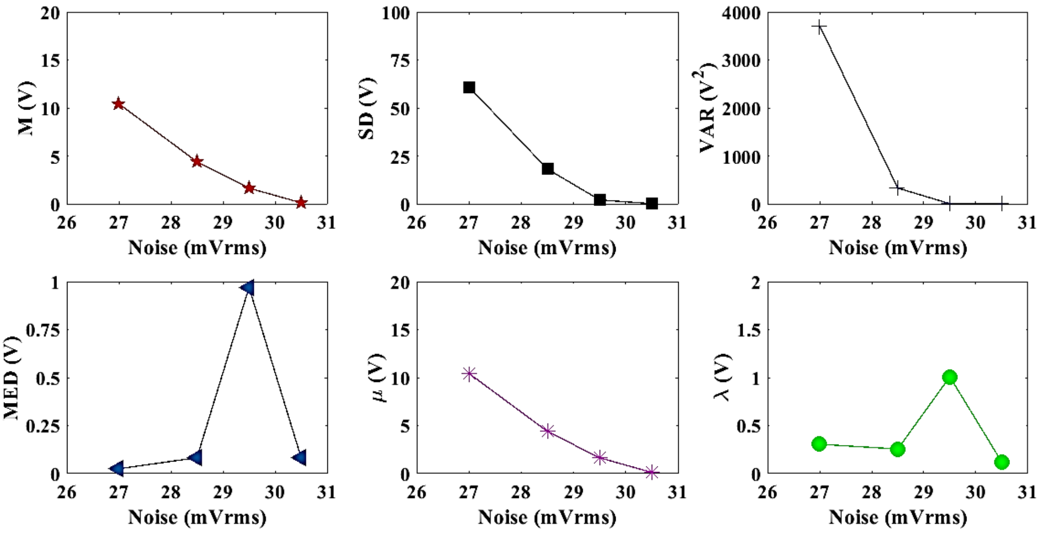

Figure 4.24 Experimental ISI parameters for different levels of noise on PMOS gate during 30min.

A Matlab code was developed to investigate the probability density function (PDF) of the obtained ISIs.

Figure 4.25.a and **Figure 4.25.b** illustrates the spike train obtained with Vin Noise = 29.54mVrms during 30min and the probability density function (PDF) of ISI corresponding to this spike train. **Figure 4.25.c** shows the PDF of ISI during 10s.

© 2018 Tous droits réservés.

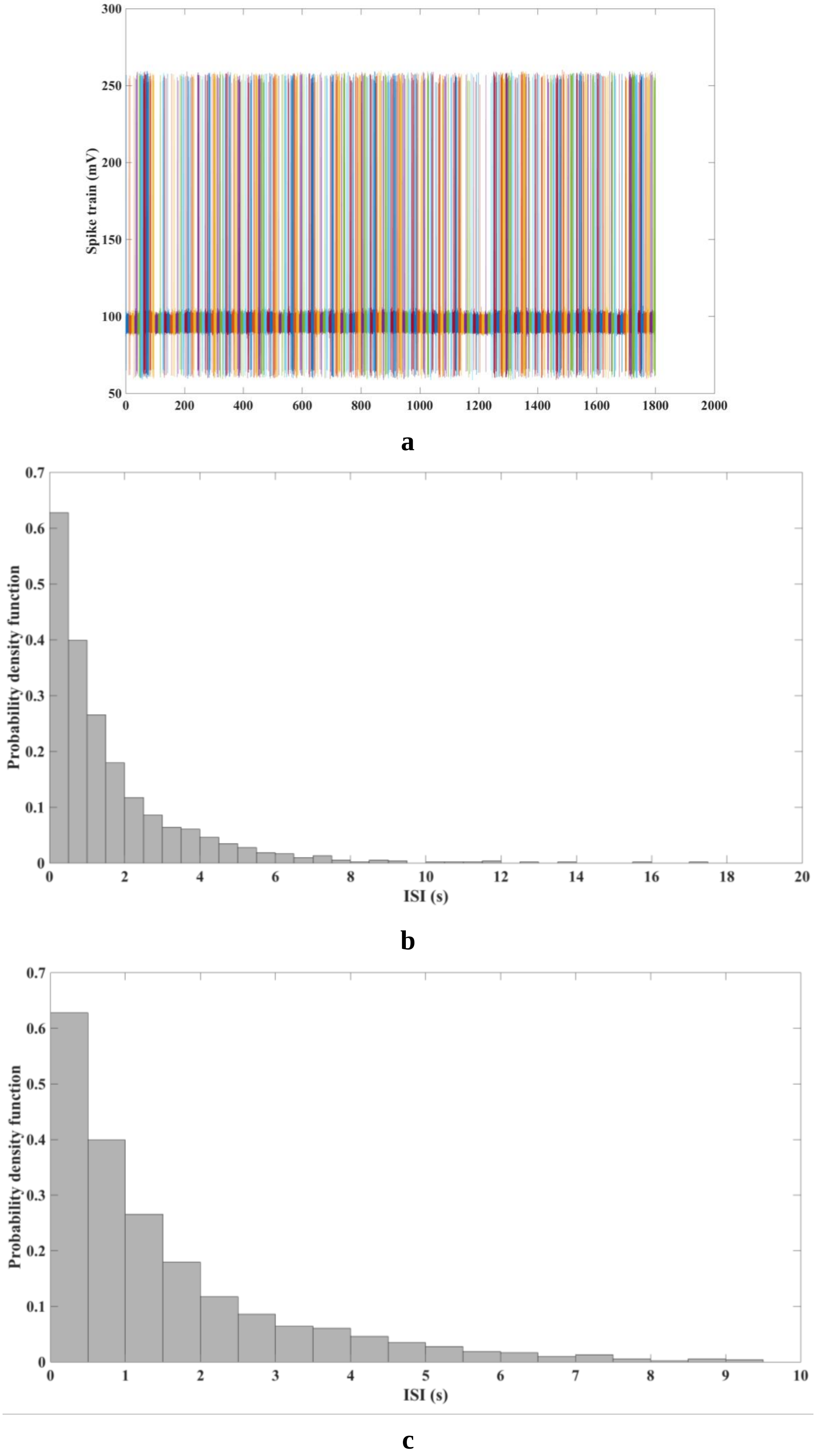

Figure 4.25: a: spike train with Vin Noise = 29.54mVrms during 30min. **b:** Complete PDF of ISI obtained from this spike train as function of ISI (0 < ISI < 20s). **c:** Zoom on the PDF (0 < ISI < 10s)

© 2018 Tous droits réservés.

Using the fit function of Matlab, we have compared several distribution functions with the measurements (see **Figure 4.26** and **Figure 4.27**). These distribution functions are: Gamma, Inverse Gaussian and Exponential. **Figure 4.26** compares the probability density function of ISI to these distributions for Vin Noise = 29.54mVrms.

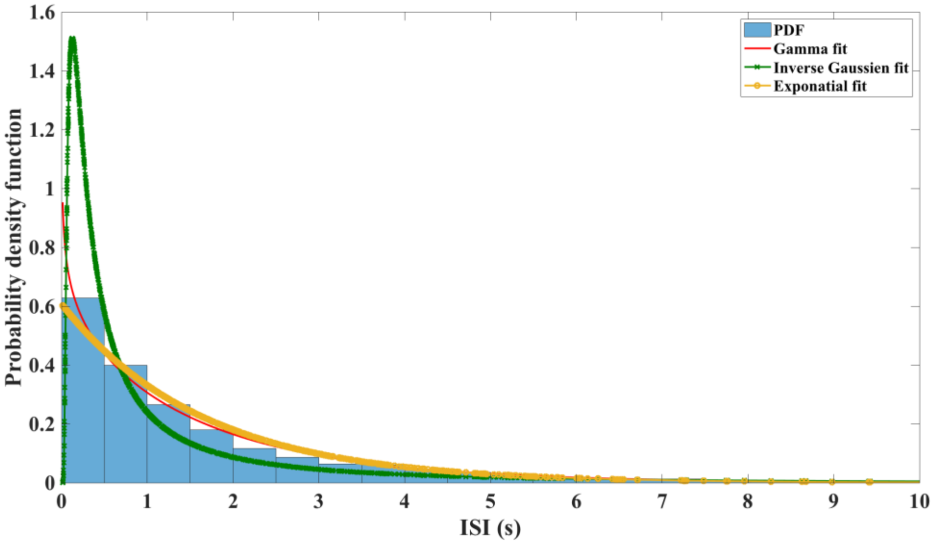

Figure 4.26 Comparison of PFD of ISI to several distributions. Vin Noise = 29.54mVrms on PMOS gate during 30min.

Same comparison is illustrated in **Figure 4.27** for Vin Noise = 30.68mVrms.

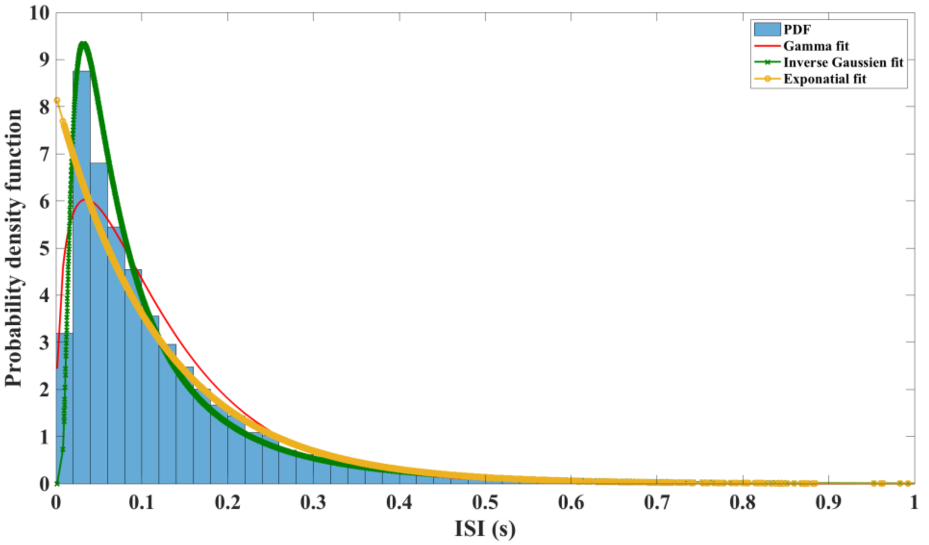

Figure 4.27 Comparison of PFD of ISI to several distributions. Vin Noise = 30.68mVrms on PMOS gate during 30min.

Based on these results, we can assume that the probability density function follows different distributions as the level noise increases. For low levels of noise

© 2018 Tous droits réservés.

(29.54mVrms) it seems to follow the Exponential and the Gamma fit. In fact as illustrated in **Figure 4.28,** the Gamma distribution reproduces the Exponential distribution when the shape factor k = 1.

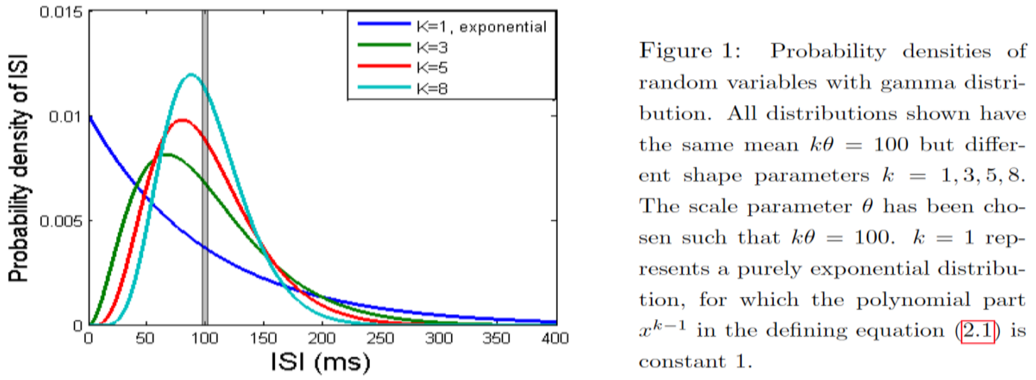

Figure 1: Probability densities of random variables with gamma distribution. All distributions shown have the same mean $k\theta = 100$ but different shape parameters $k = 1, 3, 5, 8$. The scale parameter θ has been chosen such that $k\theta = 100$. $k = 1$ represents a purely exponential distribution, for which the polynomial part x^{k-1} in the defining equation (2.1) is constant 1.

Figure 4.28 Gamma distribution (Pachitariu, Brody, Jun, & Holmes, n.d.).

Beyond a certain level of noise considered as high level of noise (30.68mVrms for the PMOS gate and 28.40mVrms for the PMOS source) the artificial neurons response tends to the inverse Gaussian distribution.

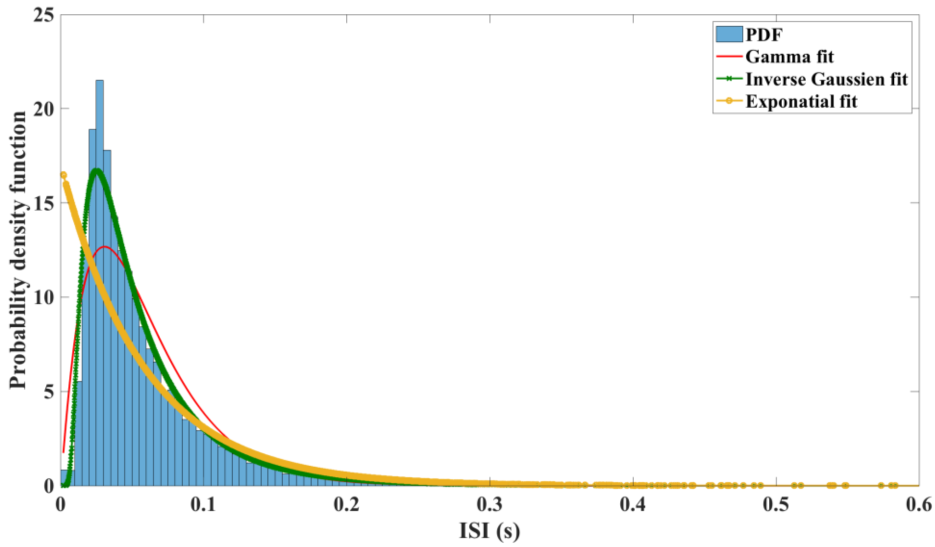

Figure 4.29 Comparison of PFD of ISI to several distributions. Vin Noise = 28.40mVrms is injected on PMOS source during 30min.

This point is put in evidence in **Figure 4.29** when a maximum noise of Vin Noise = 28.40mVrms is applied to the PMOS source of the biomimetic neuron.

© 2018 Tous droits réservés.

4.3.7 Simulation of biomimetic neuron response to the synaptic noise

We have analyzed the spike train of the biomimetic neuron for different level of Gaussian noise using LTspice simulations. It enables us to extract the injected current to the membrane capacitance of the biomimetic neuron for different level of injected noise on the PMOS gate. The Gaussian noise level varies from 27mVrms to 100mVrms. To obtain a Gaussian noise in LTspice, we use the random function (rand (time*1e6)) and injected to the PMOS gate of the biomimetic neuron. For instance, to simulate a 27mVrms Gaussian noise, we use the following expression (E.4.1) in LTspice:

Vin Noise = Vrms * SQRT(12/6) * (rand(time*1e6) + rand(A+ time*1e6) + rand(B+ time*1e6) + rand(C+ time*1e6) + rand(D+ time*1e6) + rand(E+ time*1e6) -3)   E.4.1

Where A, B, C, D and E are respectively 1.1e9, 2.07e9, 3.05e9, 4.06e9 and 5.08e9. The Vrms is the RMS noise value (here Vrms = 27mVrms). This Gaussian noise has a 150mV offset value, which is the minimum value of Vin (injected signal to PMOS gate) when the neuron does not generate spikes. The response of the biomimetic neuron to a 27mVrms noise and the average injected current is illustrated during 100ms in **Figure 4.30**. Only one spike was generated during 100ms.

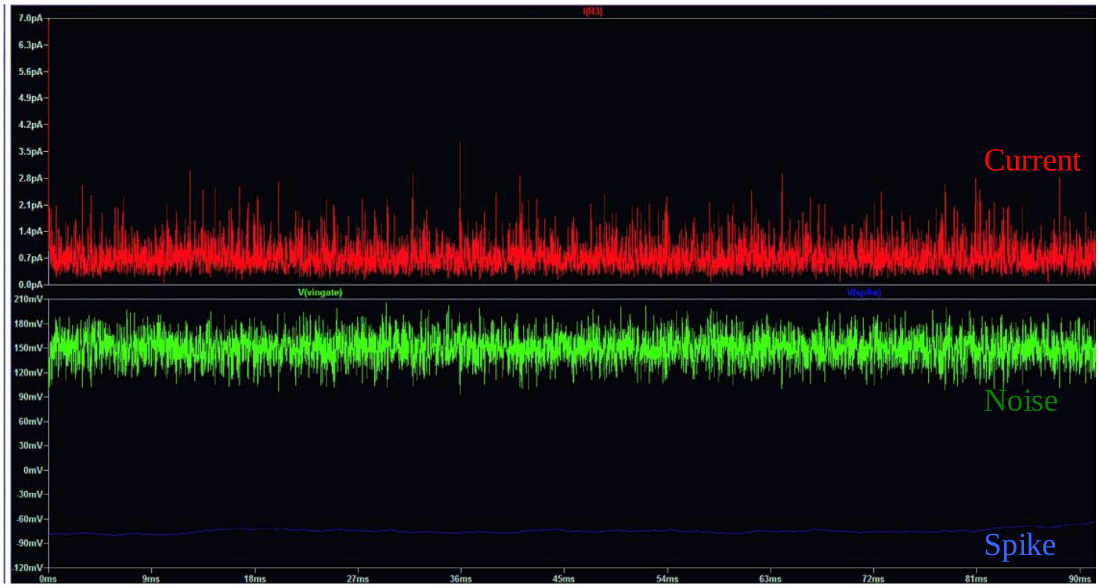

Figure 4.30 Response of the biomimetic neuron (blue curve) under Vin Noise = 27mVrms (green curve) and injected average current of 738.73fA (red curve). This figure is obtained after 100ms.

This spike train is obtained with 10µs resolution. It is worth mentioning that with this time resolution and an acquisition time of 30min (as performed in the experimental

© 2018 Tous droits réservés.

part), the extracted spike data will occupy 8Go of memory. Hence, we have chosen to reduce the acquisition time in function of the level of noise.

Gaussien Noise on PMOS gate (mVrms)	Acquisition time	Spike frequency	Average of current	RMS of current
27	60s	3Hz to 30Hz	738.73fA	813.65fA
30	30s	40Hz	783.23fA	881.02fA
40	25s	176.09Hz	982.12fA	1.21pA
50	20s	252.3Hz	1.25pA	1.76pA
60	15s	355Hz	1.63pA	2.67pA
70	12s	412.32Hz	2.11pA	3.94pA
80	10s	505.90Hz	2.65pA	5.63pA
90	8s	758.85Hz	3.20pA	9.15pA
100	5s	834Hz	4.11pA	17.9pA

Table 4.7 Spike train and current parameters obtained with simulation.

The acquisition time, spike frequency, average current and RMS current are reported in **Table 4.7** for distinctive level of noise.

Figure 4.31 shows the extracted ISI parameters of the biomimetic spike train for Vin Noise =27mVrms to Vin Noise=100mVrms.

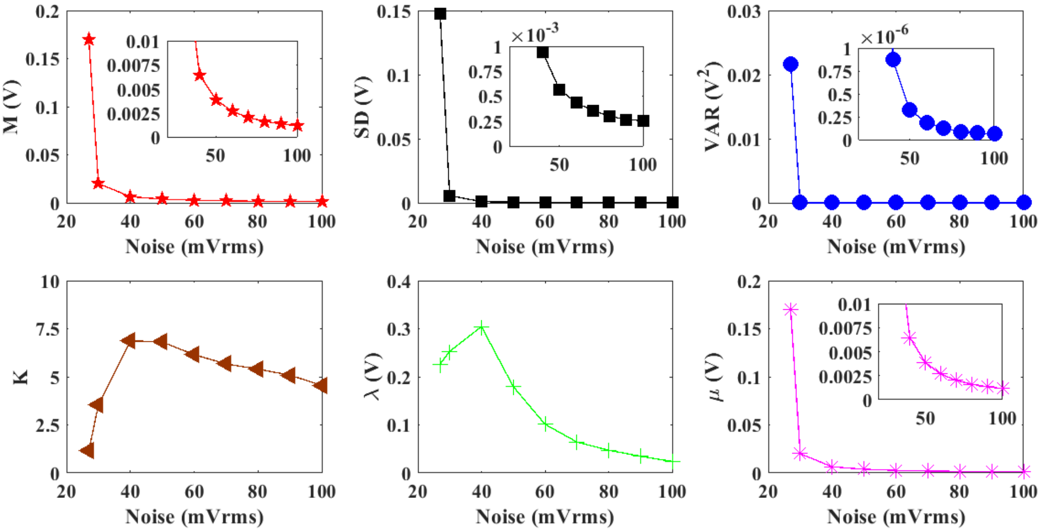

Figure 4.31 ISI parameters obtained with simulation.

© 2018 Tous droits réservés.

Figure 4.32 and **Figure 4.33** compare the PDF of ISI for Vin Noise = 27mVrms and Vin Noise = 100mVrms with different distributions (same figure for other level of noise are presented in annex).

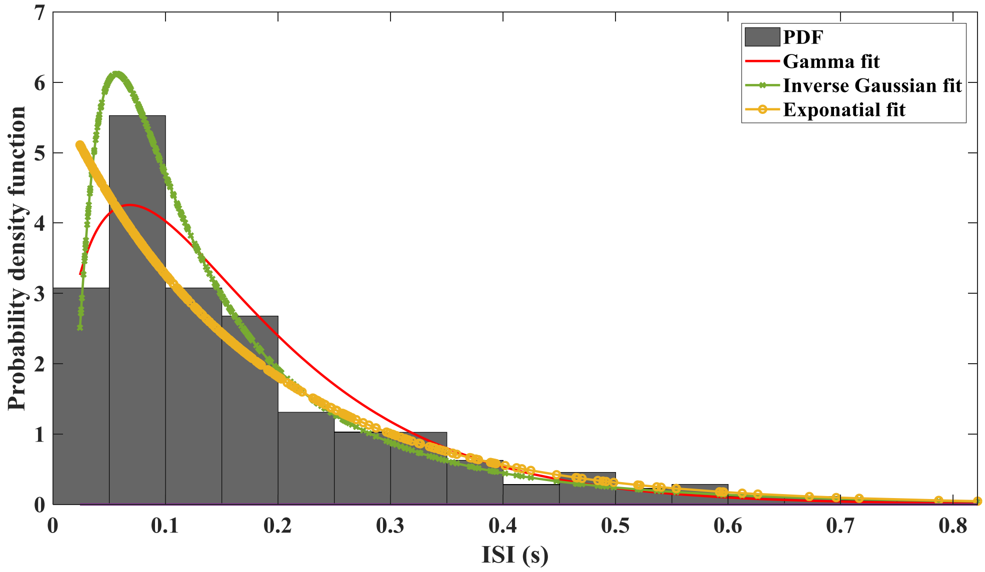

Figure 4.32 Comparison of PDF of ISI obtained with simulation to several distribution functions. Vin Noise = 27mVrms is injected on PMOS gate during 60s.

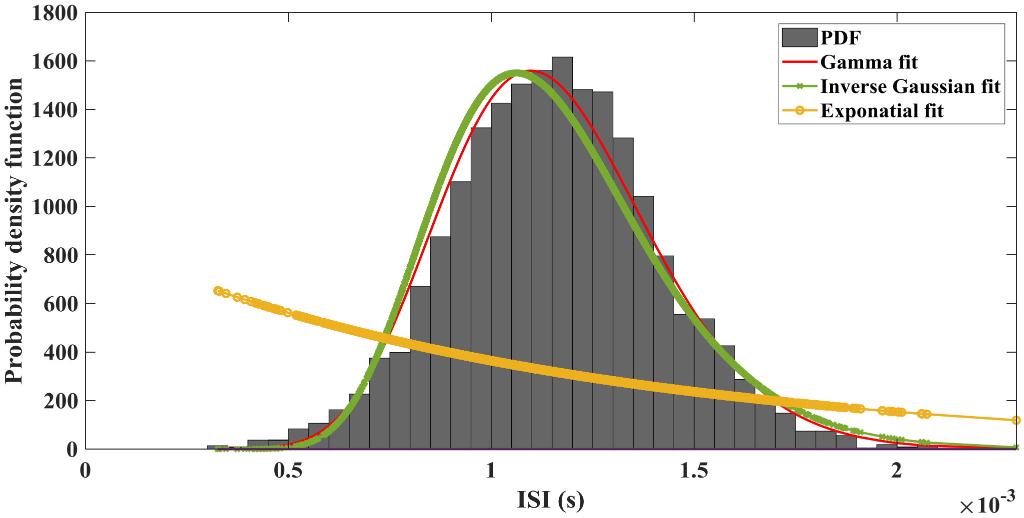

Figure 4.33 Comparison of PDF of ISI obtained with simulation to several distribution functions. Vin Noise = 100mVrms is injected on PMOS gate during 5s.

The inverse Gaussian and Gamma distribution seems to correspond to the PDF of obtained ISI for different level of noise expected the very low level of noise (27mVrms).

© 2018 Tous droits réservés.

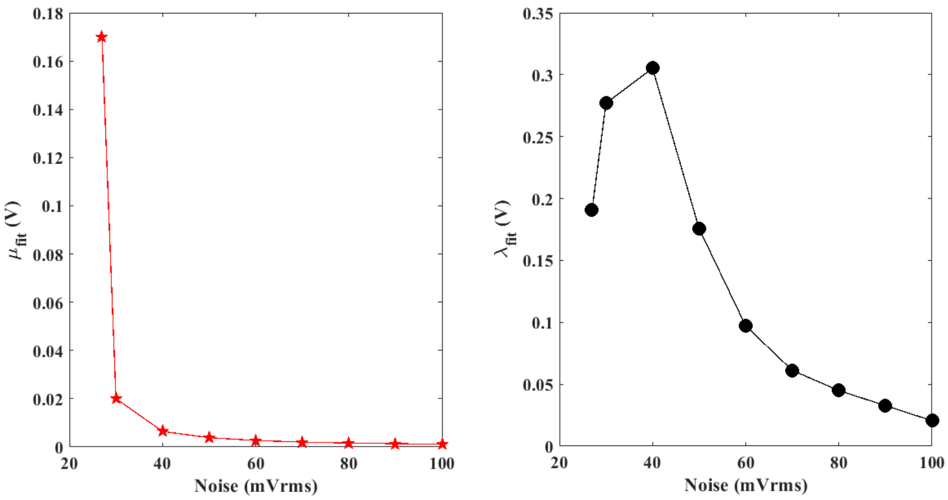

Figure 4.34 μ and λ obtained from the Matlab fit.

The fit parameters of the inverse Gaussian are illustrated in **Figure 4.34** and corresponds to the μ and λ obtained from the ISI.

© 2018 Tous droits réservés.

4.4 Stochastic resonance in the artificial neuron

4.4.1 Stochastic resonance history

After studying the membrane voltage fluctuations, which corresponds to the noise of artificial neuron in resting state and the response of the artificial neuron to an excitatory synaptic noise, we will investigate in this section the phenomenon of the stochastic resonance.

Historically, stochastic resonance has been defined as a paradoxical phenomenon as induced noise enhances the overall performance of the nonlinear system. Since 1980, when stochastic resonance was introduced in statistical physics, the concept has evolved and has been observed throughout diverse scientific fields, ranging from biological systems to nonlinear physical systems (McDonnell & Abbott, 2009). Stochastic Resonance (SR) has been studied in three different fashions, the first focused on physical and mathematical descriptions of SR (Jung, 1993), the second investigated SR in electronic systems and its potential applications (Harmer, Davis, & Abbott, 2002), and the last have dedicated their research to study SR in biology (Faisal, Selen, & Wolpert, 2008), (McDonnell & Ward, 2011). It is worth mentioning, combining these different aspects of SR phenomenon opens tantalizing perspectives, from the development of new families of sensors to brain research enabling bioinspired processing and medical applications. From a neuroscience point of view, SR is ubiquitous in neural systems and plays a major role in facilitating the information processing. These stochastic resonance features have been demonstrated both experimentally and theoretically from the complete organism (crayfish, paddlefish and human) to neural networks and the unitary cell (shark multimodal sensory cell, hippocampal model, cat cortex model) (McDonnell & Ward, 2011).

4.4.2 Simulation response of biomimetic neuron to stochastic resonance

The SR phenomenon is observed with LTspice simulation with a resolution time of 10µs. In fact to obtain the SR phenomena it is necessary to combine a sub-threshold signal (VS) (here sinusoidal signal) with a broadband noise (VN) (see **Figure 4.36**). The resulting combined signal (VSN) is injected to the PMOS gate of the trans-conductance (see **Figure 4.36**). In **Figure 4.35** the simulated combined signal VSN = 6mVrms with VS = 10mVpp (10Hz frequency and an offset of 150mV) is illustrated. For this low level of noise, the artificial neuron generates only one spike for each negative period of VS. As we increase the level of noise (VSN), the number of spike will increase. This part will be presented in detail in the next section (experimental investigation of SR).

© 2018 Tous droits réservés.

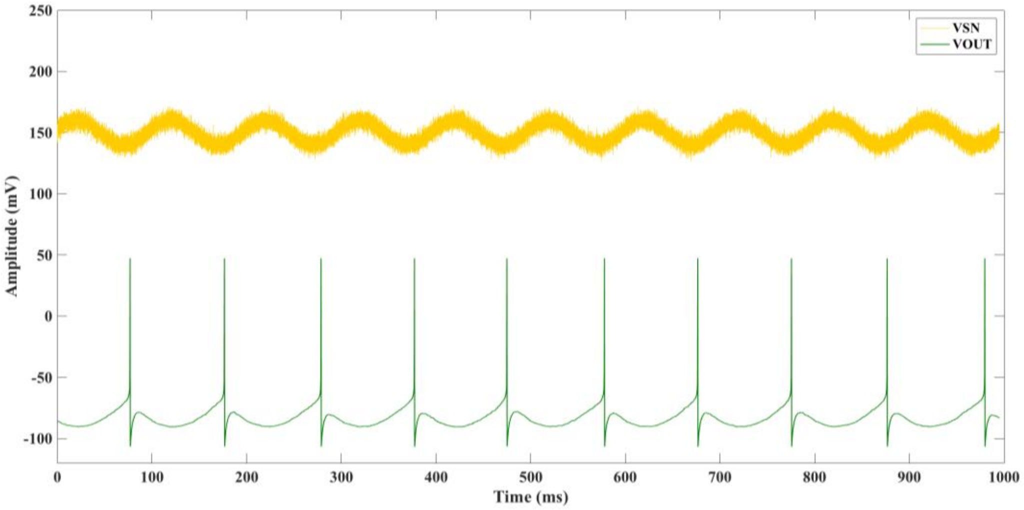

Figure 4.35 LTspice simulation of SR.

4.4.3 Stochastic resonance test bench and biomimetic neuron response

In order to experimentally demonstrates the stochastic resonance in the biomimetic neuron (from the WetWire chip), the test bench is constituted of a Keithley 4200-scs, two Keysight 33500B-30MHz and a ROHDE & SCHWARZ oscilloscope RTM 2054 500MHZ-5GSa/s (see **Figure 4.36**). The Keithley is used to bias the biomimetic neuron (VDD = 200mV, VSS = 0mV), the excitatory trans-conductance (VDD_T = 200mV) and the buffer of biomimetic neuron (VDDANA = 300mV, ISSANA = -43µA).

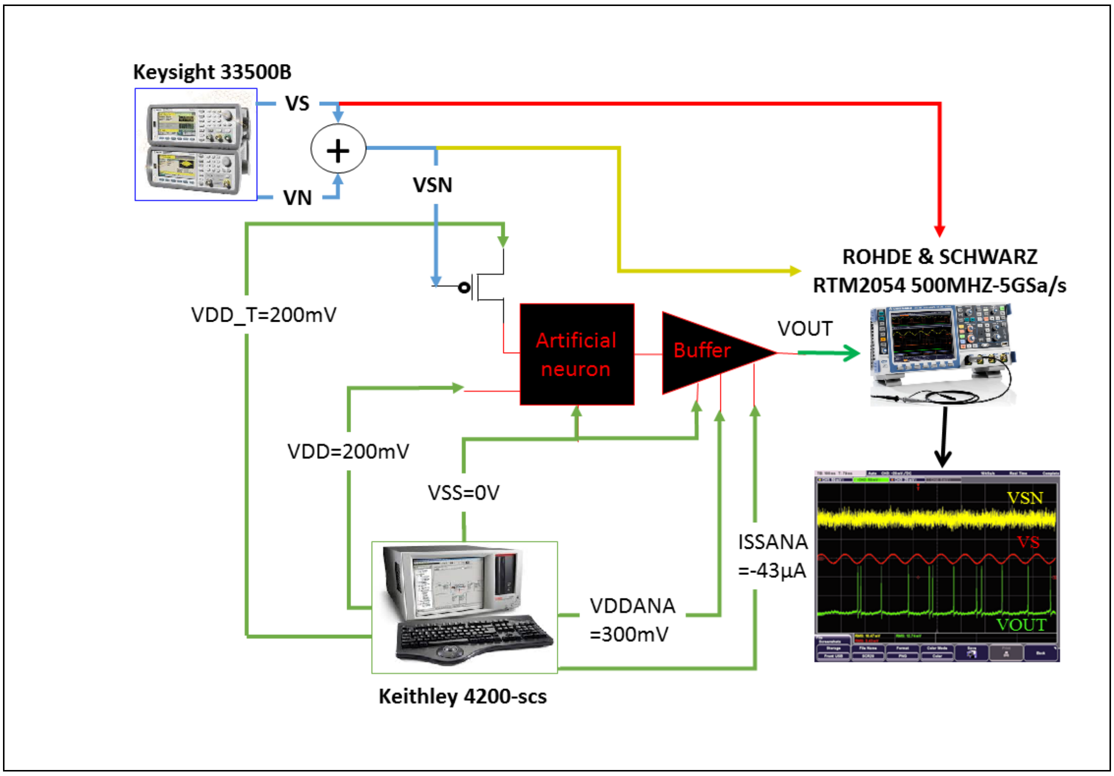

Figure 4.36 Test bench of stochastic resonance.

© 2018 Tous droits réservés.

For this experiment, the Keysight is used to generate both a sub-threshold sinusoidal signal (VS) of weak amplitude and weak frequency (10mVpp, 10 Hz) with an offset value of 110mV and a broadband noise (VN). The resulting combined signal is called VSN and is injected to the input of the neuron, which is the gate of the PMOS trans-conductance (see **Figure 4.36**). The output of neuron (VOUT), which corresponds to the membrane voltage after the buffer, is connected to R&S oscilloscope.
In this condition, and without significant noise amplitude, the biomimetic neuron stayed in its resting state since VSN was below than the firing threshold as shown in **Figure 4.37.a**. A spiking firing pattern arose as VN increased with a timing distribution that varies as a function of the sinusoidal signal rhythm and noise magnitude (**Figure 4.37.b**). Increasing, furthermore, VN increased the sensitivity of the biomimetic neuron to the weak excitatory signal and its response was enhanced as shown in **Figure 4.37.c**. These results clearly highlight the stochastic resonance phenomenon as observed in biology (Hänggi, 2002).

Based on the recording of VOUT for 1s which corresponds to ten times the period of VS, the statistical firing probability, as defined in (Chen, Saïghi, Buhry, & Renaud, 2010) is obtained by dividing the 1s recording in 10 parts. Each part is divided in 10 and the corresponding number of spikes is counted. The number of spikes is summed for each 0.1s and illustrated in **Figure 4.37.d**.

From the extracted histogram, the signature of the deterministic sinusoidal signal can be recovered.

© 2018 Tous droits réservés.

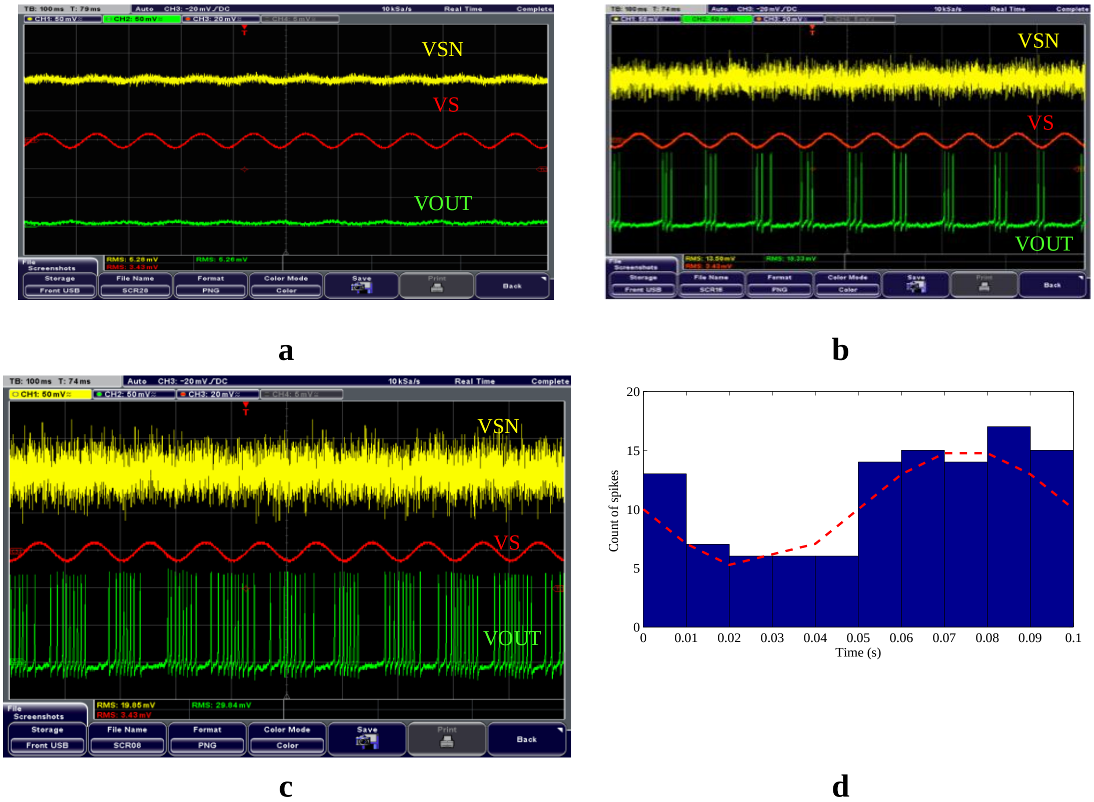

Figure 4.37 biomimetic neuron response for VS = 10mVpp with 10Hz frequency and different VN and VSN levels. a) VN= 11.36mVrms, VSN= 5.28mVrms. b) VN= 45.45mVrms, VSN= 13.50mVrms. c) VN = 68.18mVrms, VSN = 19.85mVrms. d) Statistical firing probability of biomimetic neuron in response to sinusoidal wave. The noise and signal amplitude are respectively VN = 600mVpp and VS =10mVpp.

4.4.4 Stochastic resonance and biomimetic neuron error probability

Stochastic resonance is observed under sinusoidal signal (see **Figure 4.38.Left**) as well as square signal (**Figure 4.38.Right**).

In order to define the error probability of the biomimetic neuron, Vm was recorded for various levels of induced noise during 1s. Each period of sub-threshold signal VS is divided in two states: the active state and resting state. The active state corresponds to the biomimetic neuron excitation for the half-negative period of VS. The active state is referred as 1 in **Figure 4.38.** The resting state is defined when biomimetic neuron is excited during the half-positive period of VS. The resting state is referred as 0 in **Figure 4.38.**

© 2018 Tous droits réservés.

Figure 4.38 Detecting states: Left: sinusoidal signal detected using stochastic resonance phenomena with error. Right: square signal detected using stochastic resonance phenomena without error.

As illustrated in **Figure 4.38** an active state is detected when the biomimetic neuron generates at least one spike on a given period. Errors occur when detection is made during a resting state or when no spike occurs during an active state (**see Figure 4.38.Left**). The error probability is defined as the ratio of the total number of errors divided by twenty, corresponding to 10 periods of VS.

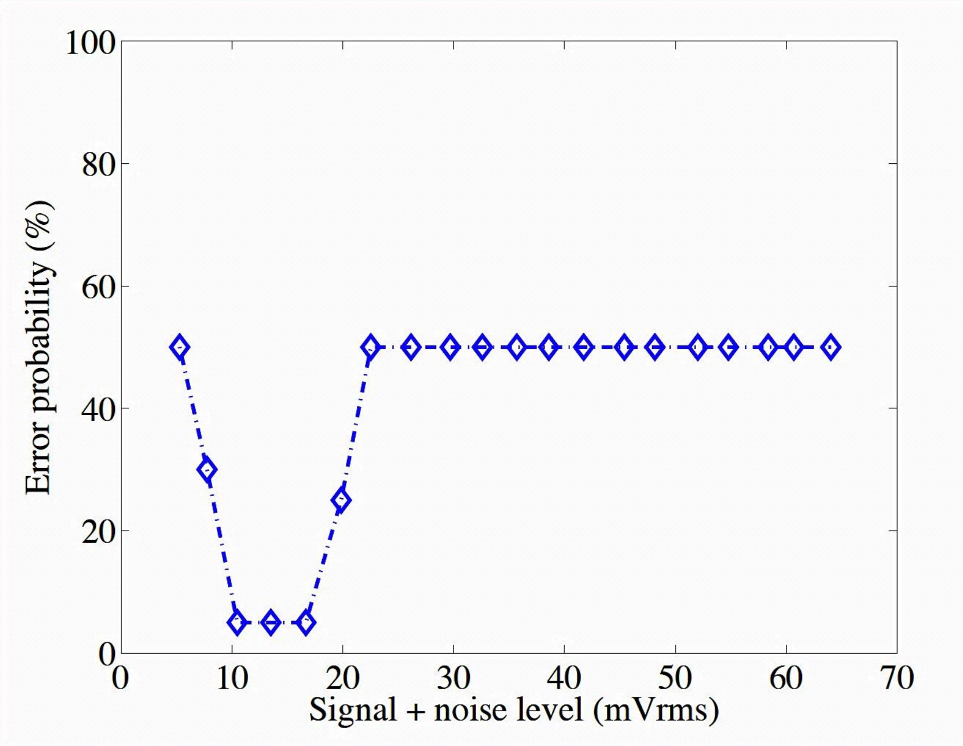

Figure 4.39 Error probability of biomimetic neuron as a function sinusoidal signal+noise level.

As described by **Figure 4.39**, the error probability decreases when the input noise is increased. It reaches the optimal value of 5% and degrades as VSN goes beyond

© 2018 Tous droits réservés.

20mVrms. The optimal VSN in order to achieve lowest error detection is around 15mVrms.

4.4.5 Stochastic resonance and biomimetic neuron signal to noise ratio, power and energy consumption

Output spikes of the biomimetic neuron in time domain (VOUT) were exported and analyzed with Advanced Designed System (ADS) software. Power spectral density has been analyzed allowing us to determine the signal to noise ratio (SNR) considering a noise bandwidth equal to 5kHz. As illustrated in **Figure 4.40,** SNR exhibits a maximum value of 22.4dB for VN = 35.7mVrms. The SNR exhibits a maximum at intermediate levels of added noise, hence experimentally demonstrating the stochastic resonance phenomenon.

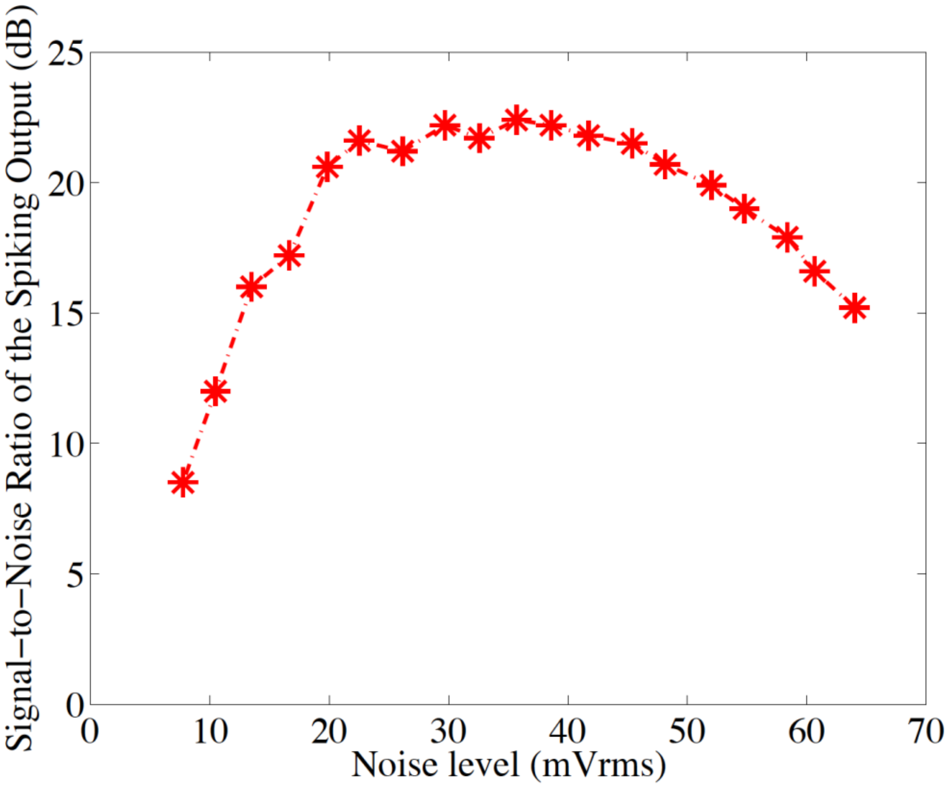

Figure 4.40 SNR as a function of noise levels.

Further measurements illustrate the power consumption of biomimetic neuron in **Figure 4.41** as a function of noise levels. The standby power consumption stands lower than 57pW independently of the noise level. The standby power is around 54.5pW. A slight increase is observed at the beginning of detection, which corresponds to the initial detection state (corresponding to number one in **Figure 4.41**).

© 2018 Tous droits réservés.

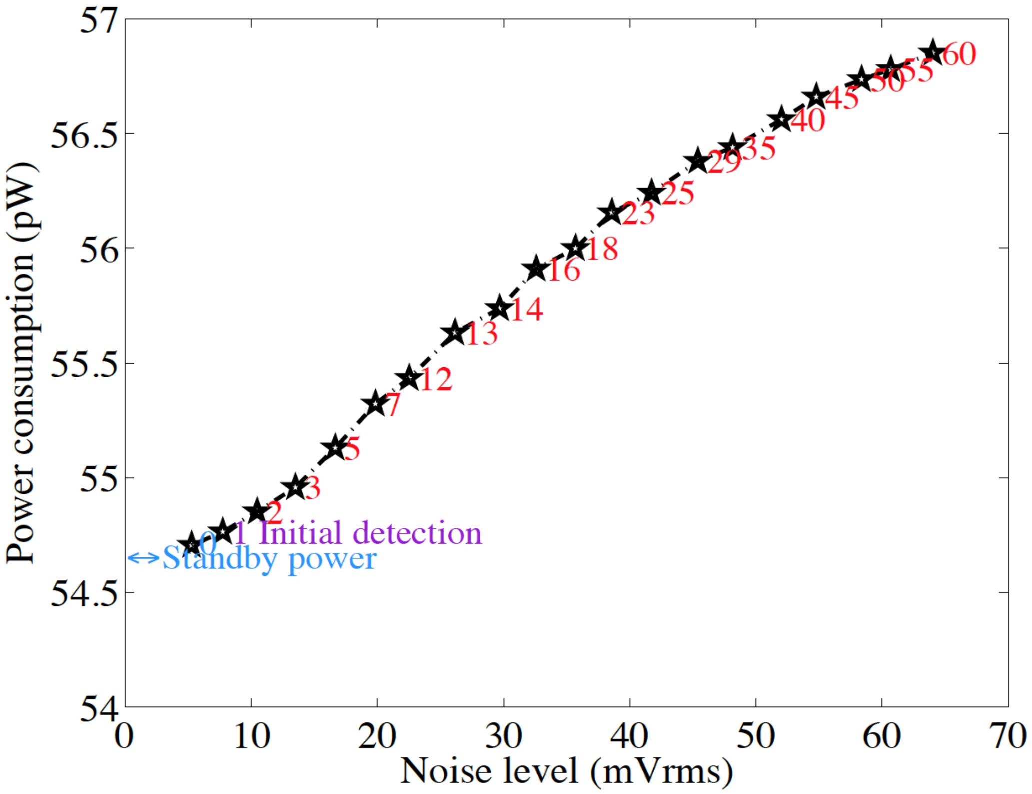

Figure 4.41 Power consumption as a function of added noise level for different detection states.

The initial state is defined when biomimetic neuron generates only one spike in the active state of VS. When increasing VN, the number of generated spikes is rising (13 spikes for VN= 26mVrms). It is obvious that the overall power consumption is mainly due to biomimetic neuron's standby power; such a low value demonstrates the biomimetic neuron's power efficiency for detection applications. The energy efficiency, for initial detection (number one in **Figure 4.41**), was estimated from the dynamic power (subtracting the standby power); in this case the biomimetic neuron encodes sub-threshold sinusoidal frequency of 10Hz; energy efficiency lower than 100fJ/spike is achieved. Such energy efficiency, compared to other stand alone artificial neuron (see chapter 3), is roughly one order magnitude lower than the state of the art.

4.4.6 Conclusion and perspectives on stochastic resonance

This work investigated and demonstrated the classical stochastic resonance phenomenon experimentally within the context of a biologically realistic artificial neuron. Ultra-low power consumption has been demonstrated while performing detection activity (between 54pW and 57pW). Considering more natural signals (Faisal, Selen, & Wolpert, 2008), (Duan, Chapeau-Blondeau, & Abbott, 2014) (such as electrical fields generated by predators or prey, lights, sounds, etc.) and biologically relevant sources of noise (synaptic noise, motor noise, colored noise, etc.) will enable

© 2018 Tous droits réservés.

to evolve stochastic facilitation and information processing within the biomimetic neuron. Furthermore, producing connected biomimetic neuron networks which demonstrate SR can be very promising and is currently under study. Finally, biomimetic neuron's biological features imply brand-new investigation of SR phenomenon, where a hybrid system of connected artificial neurons to biological neurons is studied, and aiming new biomedical applications.

© 2018 Tous droits réservés.

4.5 Annex

Simulation results of biomimetic response to the synaptic noise:

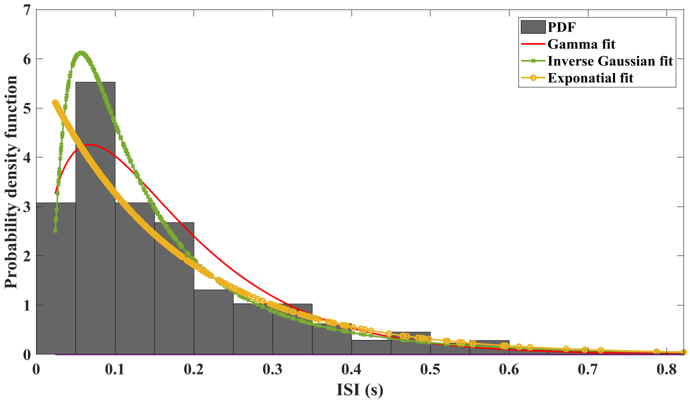

Comparison of PDF of ISI obtained with simulation to several distribution functions. Vin Noise = 27mVrms is injected on PMOS gate during 60s.

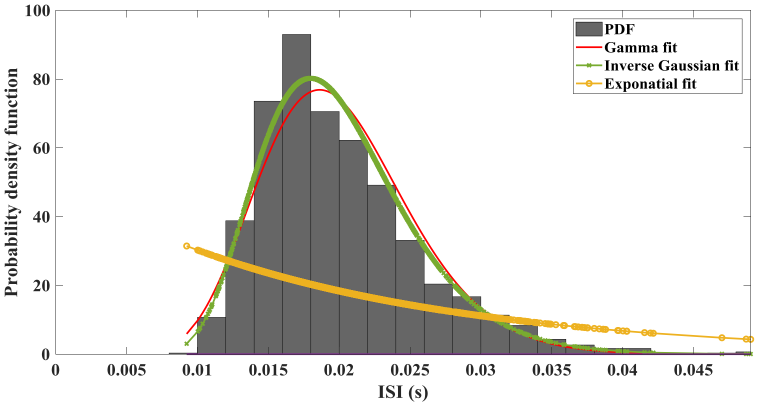

Comparison of PDF of ISI obtained with simulation to several distribution functions. Vin Noise = 30mVrms is injected on PMOS gate during 30s.

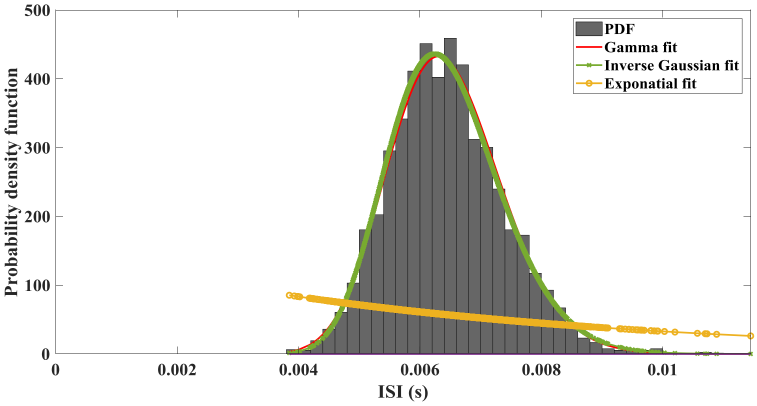

Comparison of PDF of ISI obtained with simulation to several distribution functions. Vin Noise = 40mVrms is injected on PMOS gate during 25s.

© 2018 Tous droits réservés.

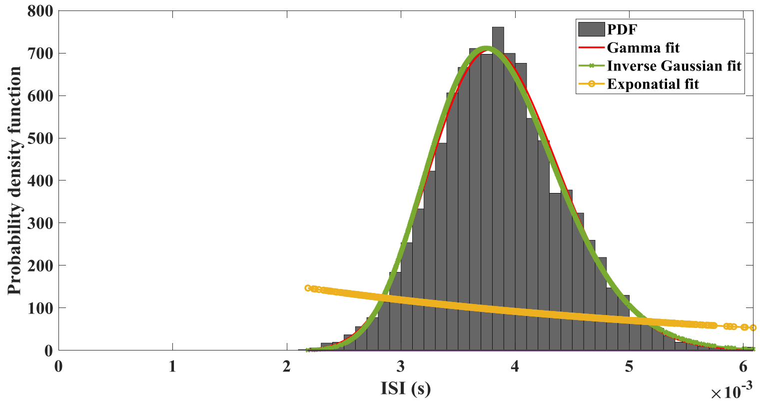

Comparison of PDF of ISI obtained with simulation to several distribution functions. Vin Noise = 50mVrms is injected on PMOS gate during 20s.

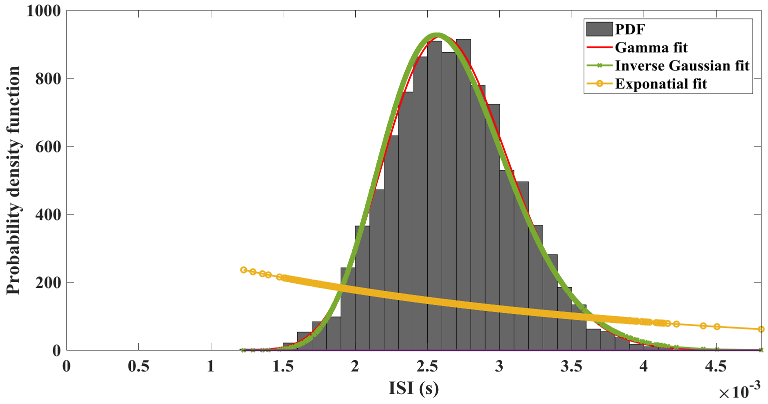

Comparison of PDF of ISI obtained with simulation to several distribution functions. Vin Noise = 60mVrms is injected on PMOS gate during 15s.

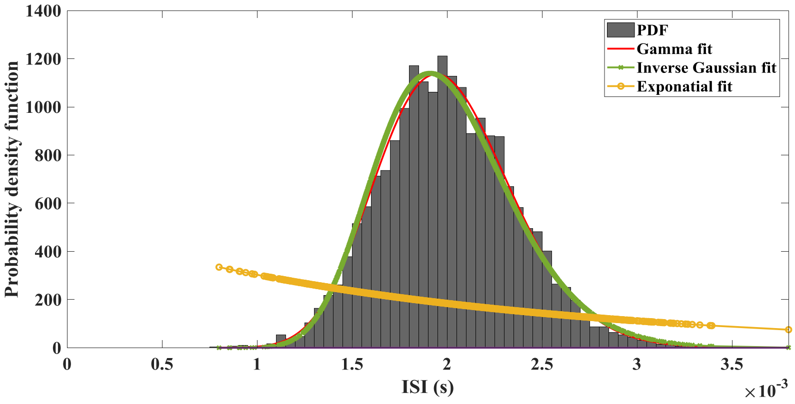

Comparison of PDF of ISI obtained with simulation to several distribution functions. Vin Noise = 70mVrms is injected on PMOS gate during 12s.

© 2018 Tous droits réservés.

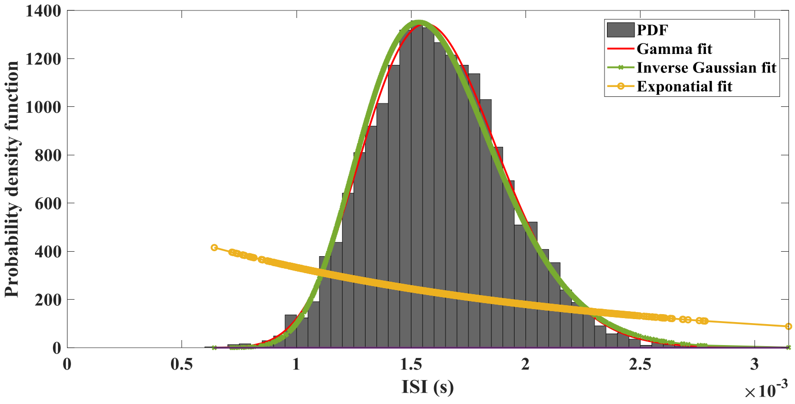

Comparison of PDF of ISI obtained with simulation to several distribution functions. Vin Noise = 80mVrms is injected on PMOS gate during 10s.

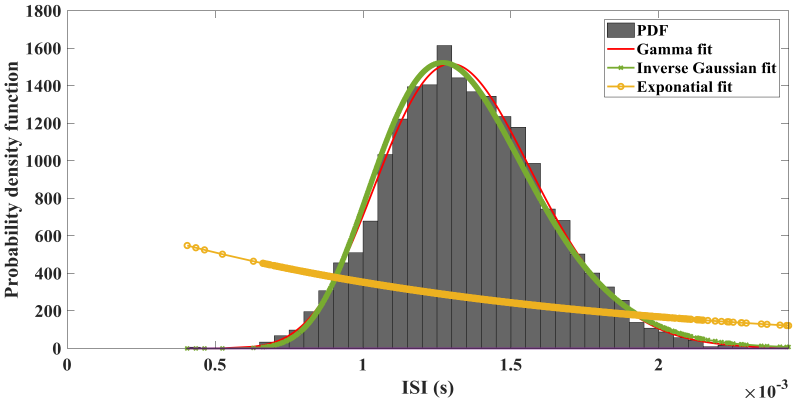

Comparison of PDF of ISI obtained with simulation to several distribution functions. Vin Noise = 90mVrms is injected on PMOS gate during 8s.

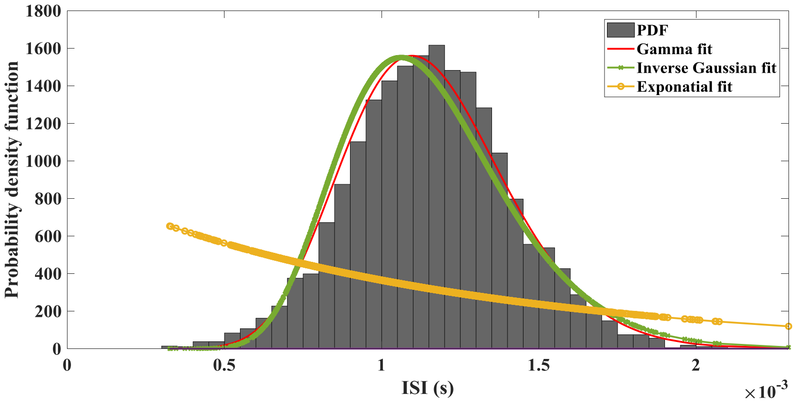

Comparison of PDF of ISI obtained with simulation to several distribution functions. Vin Noise = 100mVrms is injected on PMOS gate during 5s.

© 2018 Tous droits réservés.

4.6 References

(Chen, Saïghi, Buhry, & Renaud, 2010) Chen, H., Saïghi, S., Buhry, L., & Renaud, S. (2010). Real-time simulation of biologically realistic stochastic neurons in VLSI. *IEEE Transactions on Neural Networks*, *21*(9), 1511–1517. https://doi.org/10.1109/TNN.2010.2049028

(Diba, 2004) Diba, K. (2004). Intrinsic Noise in Cultured Hippocampal Neurons: Experiment and Modeling. *Journal of Neuroscience*, *24*(43), 9723–9733. https://doi.org/10.1523/JNEUROSCI.1721-04.2004

(Destexhe, Rudolph, Fellous, & Sejnowski, 2001) Destexhe, A., Rudolph, M., Fellous, J. M., & Sejnowski, T. J. (2001). Fluctuating synaptic conductances recreate in vivo-like activity in neocortical neurons. *Neuroscience*, *107*(1), 13–24. Retrieved from http://www.ncbi.nlm.nih.gov/pubmed/11744242

(Destexhe, Rudolph, & Paré, 2003) Destexhe, A., Rudolph, M., & Paré, D. (2003). The high-conductance state of neocortical neurons in vivo. *Nature Reviews Neuroscience*, *4*(9), 739–751. https://doi.org/10.1038/nrn1198

(Duan, Chapeau-Blondeau, & Abbott, 2014) Duan, F., Chapeau-Blondeau, F., & Abbott, D. (2014). Stochastic resonance with colored noise for neural signal detection. *PLoS ONE*, *9*(3), e91345. https://doi.org/10.1371/journal.pone.0091345

(Engel, Chaisangmongkon, Freedman, & Wang, 2015) Engel, T. A., Chaisangmongkon, W., Freedman, D. J., & Wang, X.-J. (2015). Choice-correlated activity fluctuations underlie learning of neuronal category representation. *Nature Communications*, *6*(1), 6454. https://doi.org/10.1038/ncomms7454

(Faisal, White, & Laughlin, 2005) Faisal, A. A., White, J. A., & Laughlin, S. B. (2005). Ion-channel noise places limits on the miniaturization of the brain's wiring. *Current Biology*, *15*(12), 1143–1149. https://doi.org/10.1016/j.cub.2005.05.056

(Faisal, Selen, & Wolpert, 2008) Faisal, A. A., Selen, L. P. J., & Wolpert, D. M. (2008). Noise in the nervous system. *Nature Reviews Neuroscience*, *9*(4), 292–303. https://doi.org/10.1038/nrn2258

(Jung, 1993) Jung, P. (1993, November 1). Periodically driven stochastic systems. *Physics Reports*. North-Holland. https://doi.org/10.1016/0370-1573(93)90022-6

(Harmer, Davis, & Abbott, 2002) Harmer, G. P., Davis, B. R., & Abbott, D. (2002). A review of stochastic resonance: circuits and measurement. *IEEE Transactions on Instrumentation and Measurement*, *51*(2), 299–309. https://doi.org/10.1109/19.997828

(Hänggi, 2002) Hänggi, P. (2002, March 15). Stochastic resonance in biology: How

© 2018 Tous droits réservés.

noise can enhance detection of weak signals and help improve biological information processing. *ChemPhysChem*. https://doi.org/10.1002/1439-7641(20020315)3:3<285::AID-CPHC285>3.0.CO;2-A

(McDonnell & Abbott, 2009) McDonnell, M. D., & Abbott, D. (2009). What Is Stochastic Resonance? Definitions, Misconceptions, Debates, and Its Relevance to Biology. *PLoS Computational Biology*, *5*(5), e1000348. https://doi.org/10.1371/journal.pcbi.1000348

(Pachitariu, Brody, Jun, & Holmes, n.d.) Pachitariu, M., Brody, C., Jun, P., & Holmes, P. (n.d.). Probabilistic models for spike trains of single neurons. *Gatsby.Ucl.Ac.Uk*. Retrieved from http://www.gatsby.ucl.ac.uk/~marius/papers/SpikTrainStats.pdf

(McDonnell & Ward, 2011) McDonnell, M. D., & Ward, L. M. (2011, June 20). The benefits of noise in neural systems: Bridging theory and experiment. *Nature Reviews Neuroscience*. https://doi.org/10.1038/nrn3061

(Rolls & Deco, 2010) Rolls, E. T., & Deco, G. (2010). The Noisy Brain: Stochastic Dynamics as a Princple of Brain Function. *Progress in Neurobiology, 2009*, (December), 68–70. Retrieved from http://www.sciencedirect.com/science/article/pii/S0301008209000197

(Richardson, 2004) Richardson, M. J. E. (2004). Effects of synaptic conductance on the voltage distribution and firing rate of spiking neurons. *Physical Review E*, *69*(5), 051918. https://doi.org/10.1103/PhysRevE.69.051918

© 2018 Tous droits réservés.

Thèse de Sara Hedayat, Université de Lille, 2018

© 2018 Tous droits réservés.

lilliad.univ-lille.fr

Chapter 5.

Conclusion and perspectives

© 2018 Tous droits réservés.

© 2018 Tous droits réservés.

5.1 General conclusion

Nature remains the best source of innovation. Many researchers have been inspired by nature and fabricate novel devices and systems to ensure a better life. In the 21st century, a growing need of intelligent systems with high-energy efficiency is emerging as described in chapter 1. The most important challenge is to continue to increase the computing performance of our computers while controlling their energy consumption. The heating of the processors not only jeopardizes their efficiency, but could also, if the current trend continues, create an energy shortage. Information and communication technologies consume nearly 10% of the worldwide energy generated and the cloud represents the fifth most electricity-consuming country after the USA, China, Russia and Japan. This energy consumption will not stop growing in the coming years due to the increase of generated data, which must be processed and stored. Moreover, the problem of the processors power dissipation has induced manufacturers since 2005 to take an important step: stop increasing the clock frequency of processors and turn to multi-core architectures. Finally, the miniaturization of components will inexorably lead to the emergence of defects that cannot be avoided.

Based on these issues and the need of ultra-low power intelligent systems, we have investigated one of the principal unities of the brain, the neuronal cell and build the first block of an intelligent neuromorphic system, the artificial neuron. This work is a step toward very large-scale hardware networks of neuronal circuits known as Hardware Neuronal Networks (HNN). We proposed in this work a high-energy efficient and simple artificial neuron with a conventional CMOS technology to be the foundation of a future high energy efficient HNN.

This thesis is a multidisciplinary work; it targets the design and fabrication of an ultra-low power artificial neuron with 65nm CMOS technology. In order to achieve this goal, the chapter 2 is dedicated to understand the electrophysiology of a neuron cell. We verified the excitability of the neuron based on different neuronal membrane models and studied the spikes generation as a function of the charge density. This study allowed us to estimate the power and energy efficiency per spike for neuronal models such as Hodgkin Huxley (HH) and Wei model.

Both HH and Wei model are based on four nonlinear differential equations (four state variables). These complex models lead to complex electrical circuits with considerable silicon surface. Thus, we investigated in chapter 2 the biophysically meaningful Morris-Lecar model as it represents a simpler model with only two nonlinear differential equations (two state variables).

© 2018 Tous droits réservés.

5.1 General conclusion

The chapter 3 presents the analogy between the two states variable Morris-Lecar model and the designed artificial neuron. The four states variables Wei model enabled us to adjust the parameters of this artificial neuron to obtain a bio-inspired neuron referred as the biomimetic neuron. Additionally, in the chapter 3, we present a simple version of the artificial neuron called the fast neuron. The characterization of various manufactured artificial neurons and neuronal circuits such as the oscillatory neuron and the tonic burst neuronal circuit is also presented in chapter 3.

It is worth mentioning that the biomimetic neuron core occupies 200µm^2 and a maximal spike frequency of 1.2kHz was obtained with a total dissipated power of 90pW. An energy efficiency (including the DC power) of 78.3fJ/spike is obtained for the biomimetic neuron, reaching values as low as 40fJ/spike when only the dynamic power is considered.

The fast neuron has a higher frequency and smaller area in comparison to the biomimetic neuron. It reaches a spike frequency as high as 26kHz with a core area of 35µm^2. The total power consumption of the fast neuron is 105pW. An energy efficiency (including the DC power) of 4fJ/spike is extracted and the power dissipation reaches values as low as 3fJ/spike when only the dynamic power is considered.

Based on these reported values, state-of-the-art performances were achieved in this work, as the artificial neuron is 1000 times more energy efficient than a living neuron. Additionally, it represents the state-of-the-art in terms of power, energy efficiency and area compared to previous works on the stand alone artificial neuron.

In chapter 4, various distinct noise analysis based on the noise phenomena observed in one living neuron were investigated. In fact, the membrane voltage fluctuation, the synaptic noise and the stochastic resonance, which occurs in the brain neuronal system, were studied within our artificial neuron.

Concerning the membrane voltage fluctuation investigation, we conclude that: (i) the membrane voltage noise in biological neurons is very high as compared with fluctuations due to thermal noise, and (ii) that a significant part of the membrane voltage noise in living neurons is due to the synaptic noise. This remains true as we compare the membrane voltage fluctuation of the artificial neuron to the living neuron.

Concerning the synaptic noise analysis, we injected a Gaussian noise to the PMOS excitatory transconductance of the biomimetic neuron to reproduce the synaptic noise both experimentally and in Ltspice simulation. Different spike trains were obtained

© 2018 Tous droits réservés.

from the biomimetic neuron as a function of different levels of injected Gaussian noise. We extracted the interspike intervals (ISI) from these spike trains and their probability density function (PDF) for short and long acquisition time windows. Based on the experimental data it seems that the PDF of ISI follows different distributions as the level of noise increase. For low levels of noise, it seems to follow the Exponential and the Gamma distribution while for higher level of noise it seems to follow the Inverse Gaussian distribution. Based on the simulation data and for high level of noise, the PDF of ISI follows Gamma distribution as well as Inverse Gaussian distribution.

Concerning the stochastic resonance analysis, we demonstrated experimentally the classical stochastic resonance phenomenon within the biomimetic neuron. Ultra-low power consumption has been obtained in the frame of detection activity (between 54pW and 57pW). The energy efficiency was estimated from only the dynamic power and it is lower than 100fJ/spike for the initial detection (when the neuron spike only once for the negative period of the sinusoidal signal). The artificial neuron high-energy efficiency is an important point for detection applications.

© 2018 Tous droits réservés.

5.2 Perspectives

The perspectives of this work are divided in two categories, the computing and the biomedical aspect.

For the computing aspect, and precisely for the hardware neural networks (HNNs) part, the aim is to develop an energy efficient neuromorphic system, able to communicate, learn and take decision like the brain. This hardware neural networks target the neuro-inspired computation of information with low costs and high-energy efficiency compared to artificial neural networks (ANNs). In this context, we have developed an artificial neuron with high-energy efficiency and small footprint enabling a high level of integration in future hardware neural networks. We have observed 70% variability in our artificial neuron due to the use of CMOS transistors in sub-threshold regime. This variability must be taken in account for future designs of the hardware neural networks. Additionally, future work on artificial synapses regarding the learning and the memory must be carried out to obtain intelligent HNNs.

From the biomedical aspect, the aim as mentioned in the chapter 1 is to fabricate a neuromorphic system, which is able to stimulate (preventing epileptic crises and slowing the Alzheimer disease) or even replace the defective brain area in case of injuries and neurodegenerative diseases. In this context, the perspective of this work is to connect the artificial neuron (the biomimetic neuron) to a living one and study the possibility of their communication while fabricating the interface system. Moreover, investigating the noise in this hybrid system is necessary due to the noisy activity of the living neuron cell. The biological features of the biomimetic neuron enable a brand-new investigation of SR phenomenon where a hybrid system of connected artificial neurons to biological neurons is studied, aiming new biomedical applications.
Furthermore, design and fabricate HNNs that communicates, stimulate and even inject drugs to the specific neuronal network of a human brain can be imagined as a long-term perspective.

© 2018 Tous droits réservés.

5.3 Scientific communications

1. Posters

[1] **Hedayat, S.,** Cappy, A., Hoel, V., Danneville, F. & Loyez, C., "Artificial neurons for information processing", DN2M-The new technology at the service of neuroscience, November 16, **2015.**

[2] **S. Hedayat** et al. “Neuromorphic information processing", France, **2016.**

[3] **Hedayat, S.,** Cappy, A., Hoel, V., Danneville, F., Loyez, C., Sourikopoulos I. and F. Danneville. "Ultra Low Power Brain Inspired Computing", Paris, April 7, **2016.**

2. Workshops

[1] **Sara Hedayat**, Virginie Hoel and Alain Cappy, "Membrane neuronale", **France,** IEMN, May 20, **2015**.

[2] Beatriz García Vasallo, Fabio Galán Prado, Javier Mateos, Tomás González
Sara Hedayat, Virginie Hoel and Alain Cappy, "A Monte Carlo simulator based on the Hodgkin and Huxley model for neuro-inspired devices", Workshop **E-MRS**, **France**, May 2-6, **2016**.

[3] Danneville, F., **Hedayat, S**., Hoel, V., Loyez, C., Sourikopoulos, I. and Cappy, A., "Electrical Simulations of Artificial Neuron in framework of Biocomputing and Biorobotics", Workshop **Irvine** -French workshop on advanced nano-imaging and bio-interface technologies, USA May 20-21, **2016**.

[4] Hoel, V., Cappy, A., **Hedayat, S.**, Loyez, C., Danneville, F. & Sourikopoulos, I.,"Artificial neurons for information processing –Towards Biomedical Applications", Workshop **Irvine** -French workshop on advanced nano-imaging and bio-interface technologies, May 20-21, **2016**.

[5] Cappy, A., **Hedayat, S.**, Sourikopoulos, I., Danneville, F., Hoel, V. and Loyez, C., " Energy efficient neuromorphic hardware", **GDR Biocomp**, October, **2016**.

© 2018 Tous droits réservés.

[6] I. Sourikopoulos, **S. Hedayat**, C. Loyez, F. Danneville, V. Hoel, E. Mercier and A. Cappy, "A 4-fJ/spike artificial neuron in 65nm CMOS technology", **Nice** workshop, **USA 2017**.

3. Conferences

[1] **S. Hedayat**, I. Sourikopoulos, C. Loyez, F. Danneville, L. Clavier, V. Hoel and A. Cappy, "Experimental investigation of stochastic resonance in a bio inspired 65nm CMOS artificial neuron", Oral presentation in **24th Int. Conf. on Noise and Fluctuations, Vilnius**, June **2017**.

[2] F. Danneville, I. Sourikopoulos, **S. Hedayat**, C. Loyez, L. Clavier, V. Hoel and A. Cappy, "Ultra Low Power Artificial Neuron in 65 nm CMOS technology", (Invited Paper), **BCTM, USA, 2017.**

4. Publications

[1] G.Vasallo, F.Galán-Prado, J.Mateos, T.González, **S.Hedayat,** V.Hoel and A.Cappy. "Monte Carlo model for action potentials in bioinspired devices", **Journal of Computational Electronics,** Volume 16, Issue 2, pp 419–430, **June 2017**.

[2] I.Sourikopoulos, **S. Hedayat**, C. Loyez, F. Danneville, V. Hoel, E. Mercier and A. Cappy, "A 4-fJ/spike artificial neuron in 65 nm CMOS technology", **Frontiers in Neuroscience**, Volume 11, Article 123, **March 2017**.

[3] **S. Hedayat**, I. Sourikopoulos, C. Loyez, F. Danneville, L. Clavier, V. Hoel and A. Cappy, "Experimental investigation of stochastic resonance in a bio inspired 65nm CMOS artificial neuron", **IEEE,** 10.1109/ICNF.2017.7985962, 20 **July 2017.**

© 2018 Tous droits réservés.